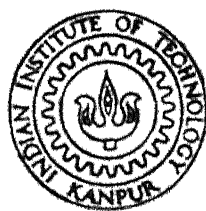


**MAGNETIC SCATTERING AND CRYSTALLIZATION STUDIES IN
AMORPHOUS $\text{Fe}_{80}\text{B}_{20-x}\text{Si}_x$ ($0 \leq x \leq 12$) USING RESISTIVITY,
MAGNETIZATION, AND MÖSSBAUER MEASUREMENTS**

by

RITA SINGHAL



DEPARTMENT OF PHYSICS

INDIAN INSTITUTE OF TECHNOLOGY KANPUR

AUGUST, 1991

PHY.

1991

D

SIN

MAG

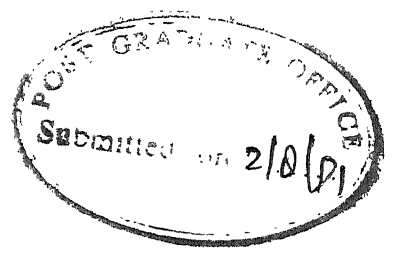
TH
PHY / 1991 / D
Singh m

**MAGNETIC SCATTERING AND CRYSTALLIZATION STUDIES IN
AMORPHOUS $\text{Fe}_{80}\text{B}_{20-x}\text{Si}_x$ ($0 \leq x \leq 12$) USING RESISTIVITY,
MAGNETIZATION, AND MÖSSBAUER MEASUREMENTS**

*A Thesis Submitted
in Partial Fulfilment of the Requirements
for the Degree of
DOCTOR OF PHILOSOPHY*

by
RITA SINGHAL

to the
DEPARTMENT OF PHYSICS
INDIAN INSTITUTE OF TECHNOLOGY KANPUR
AUGUST, 1991



C E R T I F I C A T E

It is certified that the work contained in the thesis entitled "MAGNETIC SCATTERING AND CRYSTALLIZATION STUDIES IN AMORPHOUS $\text{Fe}_{80}\text{B}_{20-x}\text{Si}_x$ ($0 \leq x \leq 12$) USING RESISTIVITY, MAGNETIZATION, AND MOSSBAUER MEASUREMENTS" by Rita Singhal has been carried out under our supervision. This work has not been submitted elsewhere for a degree.

Alak Kumar Majumdar
(Alak Kumar Majumdar)
Professor
Department of Physics
I I T Kanpur, INDIA

R. M. Singru
(R. M. Singru)
Professor
Department of Physics
I I T Kanpur, INDIA

August, 1991

27 AUG 1992
CENTRAL LIBRARY
INDIAN AIR FORCE
Acc. No. A11404U

PHY-1991-D-SIN-MAG

SYNOPSIS

Name of Student : RITA SINGHAL Roll No. 8410968

Degree for which submitted : Ph.D., Department of Physics

Thesis Title : MAGNETIC SCATTERING AND CRYSTALLIZATION STUDIES
IN AMORPHOUS $\text{Fe}_{80}\text{B}_{20-x}\text{Si}_x$ ($0 \leq x \leq 12$) USING
RESISTIVITY, MAGNETIZATION, AND MOSSBAUER
MEASUREMENTS.

Thesis Supervisors : Dr. A.K. Majumdar, Professor of Physics,
I.I.T. Kanpur - 208016, India.

Dr. R.M. Singru, Professor of Physics, I.I.T.
Kanpur - 208016, India.

Month and year of thesis submission : August 1991

Metallic glasses are fascinating from both experimental as well as theoretical point of view. The research in metallic glasses helps us to understand noncrystalline matter. By varying composition continuously in preparing homogeneous alloys, one can study these as a function of composition and temperature without the complicating interference from structural phase transitions. This is one of the main advantages of studying these amorphous alloys. Any correlation or comparison would be meaningful if different measurements are done on the same set of samples belonging to a series. For this reason we have chosen $\text{Fe}_{80}\text{B}_{20-x}\text{Si}_x$ ($0 \leq x \leq 12$) amorphous alloys.

The motivation behind the present work is :

- a) To see whether there is any magnetic contribution at all to the electrical resistivity in these materials.
- b) If it is there, does it occur through a $T^{3/2}$ term which is theoretically the leading term in amorphous materials or

through a T^2 term as found quantitatively by others in a similar system.

- c) To see whether the same temperature dependence of resistivity holds in the presence of external magnetic field as in the the zero-field case and to study the effect of magnetic field on magnetic scattering.
- d) To investigate the effect of substitution of B by Si on the magnetic properties as well on the crystallization process.

To this end we used different experimental techniques like measurements of resistivity at different temperatures and magnetic fields, temperature dependence of magnetization, Mössbauer spectroscopy, and X-ray diffraction.

Chapter I of the present thesis deals with the general introduction to the subject, brief review of the literature, motivation behind the work, and the basic theoretical background of the subject.

Chapter II gives the details of various experimental set-up used in the present work. The electrical resistivity set-up consists of a digital multimeter, a temperature controller, a constant-current source (optional), and a closed-cycle helium refrigerator. Electrical resistivity measurements were made from 8 to 300 K using a four-probe dc method. The temperature stability was within ± 0.1 K. The accuracy of $\Delta R/R$ was better than 1 part in 10^5 . Magnetoresistance was measured in both orientations (current density $\vec{J} \parallel \vec{M}$ and $\vec{J} \perp \vec{M}$, where \vec{M} is the magnetization) at several constant temperatures. An external constant-current source was used. In these measurements the

accuracy of $\Delta R/R$ was about 1 part in 10^6 .

High- and low - temperature magnetization measurements were done by using a vibrating sample magnetometer (VSM). For high-temperature measurements a high-temperature oven assembly, in conjunction with the VSM, was used. For low-temperature measurements, a closed-cycle helium refrigerator was employed. Whenever needed, the external magnetic field up to 16.5 kOe was provided by an electromagnet.

The Mössbauer spectrometer consists of a radioactive source, Mössbauer drive, gamma-ray detection and amplification system, and a multichannel analyzer (MCA) for data storage. Gamma-ray photon detection system, used in the present work, consists of a proportional counter, preamplifier, high-voltage power supply, and a spectroscopy amplifier.

Chapter III deals with the results and discussion of our experimental observations. The temperature dependence of electrical resistivity of $\text{Fe}_{80}\text{B}_{20-x}\text{Si}_x$ ($0 \leq x \leq 12$) amorphous ferromagnets has been studied in the range 8-300 K. In magnetic materials, over and above the scattering of electrons by structural disorders and lattice vibrations, there must be some evidence of magnetic scattering. Theoretically, the leading term in the magnetic resistivity is a $T^{3/2}$ term followed by a higher order T^2 term. The normalized resistivity data have been fitted in two ways in the low-temperature range (35-85 K). (i) When the magnetic contribution is considered through a T^2 term [$r(T) = \alpha_0 + \alpha_2 T^2$]; here the T^2 term comprises of contributions from both the structural and the magnetic terms. (ii) When the magnetic contribution is through a $T^{3/2}$ term [$r(T)$

$=\alpha_0 + \alpha_{3/2} T^{3/2} + \alpha_2 T^2]$; here the T^2 term is of structural origin only. The goodness of fit and the nature of the deviations show much better fit in the second case implying that there is a need for the $T^{3/2}$ term. In the high-temperature range (200 - 300 K), the data have been fitted in three different ways. (i) When no magnetic term is considered, i.e., $r(T) = \alpha_0' + \alpha_1' T$, the linear term is due to electron-phonon scattering. (ii) When the magnetic contribution is incorporated through a T^2 term, i.e., $r(T) = \alpha_0' + \alpha_1' T + \alpha_2' T^2$. (iii) When the magnetic contribution is through a $T^{3/2}$ term, i.e., $r(T) = \alpha_0' + \alpha_1' T + \alpha_{3/2}' T^{3/2}$. It has been observed that there is a significant improvement in the fit when either a T^2 or a $T^{3/2}$ magnetic term, in addition to the linear term in T , is included. However, it is difficult to choose between the two, i.e., T^2 or $T^{3/2}$ term in the high-temperature range. The presence of the $T^{3/2}$ term in the low-temperature range could also be seen from the temperature derivative of resistivity versus temperature plots. The values of the coefficients, obtained from these fits, are used to calculate the Debye temperature (θ_D). The composition dependence of the various coefficients do not show any specific trend. The room-temperature value of electrical resistivity ρ is $(127 \pm 10) \mu\Omega \text{ cm}$ for the whole series. It does not show any composition dependence within the experimental accuracy.

The longitudinal ($\vec{J} \parallel \vec{M}$) and the transverse ($\vec{J} \perp \vec{M}$) magnetoresistances, given by $\Delta\rho_{\parallel}/\rho = (\rho_{\parallel} - \rho)/\rho$ and $\Delta\rho_{\perp}/\rho = (\rho_{\perp} - \rho)/\rho$, have been measured for samples with $x = 0, 6$, and 12 between 10 and 300 K using magnetic fields up to 16.5 kOe. We find that the ferromagnetic anisotropy of resistivity (FAR) is not

influenced by the replacement of B by Si. The temperature dependence of FAR is explained on the basis of Campbell's model. FAR versus temperature roughly follows the linear magnetostriction coefficient versus temperature graph as the origin of the two lies in the spin-orbit interaction present in a ferromagnet. The magnitude of the slope $\left(\frac{1}{\rho} \frac{d\rho}{dH}\right)$ as a function of temperature is also explained. It has been observed that the domain magnetization is not randomly oriented in these amorphous ribbons. Our analysis indicates that the replacement of B by Si does not change this special orientation of \vec{M} . The $R(T)$ data have been taken at constant fields of 2, 7, and 14 kOe. We find that the same temperature dependence of resistivity holds in the presence of external magnetic field as in the zero-field case. The effect of magnetic field on the various magnetic scattering process is also discussed.

The magnetization M as a function of temperature has been measured for samples with $x = 0, 6$, and 12 at $H = 6$ kOe. The data have been fitted in two ways, first with both $T^{3/2}$ as well as $T^{5/2}$ terms and secondly with the $T^{3/2}$ term alone. The $T^{3/2}$ term is the famous Bloch law, while the $T^{5/2}$ term is due to higher order terms in magnon dispersion relation. The coefficient of the $T^{3/2}$ term agrees very well with the literature values for $x=0$. It does not show any variation with Si concentration. The presence of the $T^{5/2}$ term could not be detected due to the relatively poor resolution of the data. The magnetic moment per iron atom is also calculated. The calculated values of spin-wave stiffness constant, D , do not have any composition dependence in contrast to the Fe-B-C system. The high-field susceptibility of $\text{Fe}_{80}\text{B}_{20}$ is

much larger than those containing Si at both room temperature and 19 K. The replacement of B by Si decreases the susceptibility which becomes nearly zero in the whole temperature range.

The low-field magnetization M as a function of temperature has been measured in the high-temperature range to study the crystallization process. For samples with $x = 0, 1$, and 2, the crystallization is a single-step process while for $x \geq 4$, the crystallization occurs in two steps. For samples ($x = 0-2$), the final crystallized phases are α -Fe and the metastable t -Fe₃B while for $x \geq 4$, the phases are α -Fe and t -Fe₂B. These results are confirmed by X-ray diffraction studies.

Mössbauer spectra, recorded at room-temperature, for samples with $x = 0, 2$, and 8 (as-received) and heat-treated at different temperatures for various time periods have been analyzed. The Mössbauer parameter isomer shift, as a function of Si concentration, is explained on the basis of charge-transfer model. The internal magnetic field shows a slight increase on the substitution of B by Si. Here Mössbauer spectroscopy has been used to study the crystallization process as well as to identify the crystallized phases. It has been observed that the final crystallized phases, for samples with $x = 0$ and 2 are α -Fe as well t -Fe₃B, but for $x = 8$ the phases are α -Fe, t -Fe₂B and FeSi (probably). The final phases are also identified by X-ray diffraction studies. We find from Mössbauer as well as high-temperature magnetization studies that the addition of Si increases the crystallization temperature implying an improvement in the thermal stability of the system.

Chapter IV highlights the conclusions of the thesis and

elaborates on further scope of work. It is hoped that the systematic investigation carried out by us using different techniques have added to our understanding of the magnetic properties of the $\text{Fe}_{80}\text{B}_{20-x}\text{Si}_x$ system.

ACKNOWLEDGMENT

I am deeply indebted to Prof.A.K. Majumdar for suggesting me this problem at a very crucial stage of my career. His valuable guidance and constant encouragement throughout the tenure has enabled me to complete this work. I am also grateful to Prof.R.M.Singru for his constant guidance throughout the work. I would like to acknowledge Prof.R.K. Ray who introduced me to this field.

I thank Dr.F.E. Luborsky for providing us the samples to carry out this work. I thank to Dr.V.A. Singh also for his valuable suggestions.

Excellent cooperation of my laboratory mates N. Sudhakar, Tapan K. Nath, Manoj Pillai , and Drs.Alok Banerjee and Amitava Mitra is greatly appreciated. Timely assistance of Mr.D.C. Banerjee in dealing with the technical and administrative details of work in the laboratory and all round help from Mr.Ram Prakash are gratefully acknowledged.

I would like to thank to Dr.U.C. Johri who extended his helping hand whenever it was needed. I thank Nobin Banerjee for his excellent cooperation and Drs.Sushma Tiwari and A.V.M. Rao for the lively atmosphere in the lab.

I thank the staff of Physics Workshop and Liquid Nitrogen Plant for their help as and when it was required.

I acknowledge the help rendered by M/s H.K. Panda, L.S. Rathor, G.R. Hoshing and Muralidhar. I thank Mr.G.B. Pant for his neat typing of the manuscript and Mr.B.K. Jain for some of the

drawings.

I thank all my friends Anu, Sangeeta, Nivedita, Manju, Damini, Chandra, Pratima, Beena, and Queeny and my cousin Manish who made my stay enjoyable at this place. It will remain always a pleasant memory with me.

I have never felt that I am away from home when I was in the company of Drs.S.K. Jain and Abhilasha.

Words shall never suffice to put all that the members of my family have done for me. Especially my mother's constant encouragement and patience has lead me to complete this work. This acknowledgment would not be complete if I do not acknowledge my father whose high spirits were always with me as a source of inspiration.

My words fail to thank Amitabh; at times his help became indispensable.

Rita Singhal

To

My Parents

CONTENT

	Page No.
LIST OF FIGURES	xiv
LIST OF TABLES	xix
CHAPTER I - INTRODUCTION	
1.1 Preamble	1
1.2 Theory	10
CHAPTER II - EXPERIMENTAL	
2.1 Electrical Resistivity and Magnetoresistance	41
2.2 Low-and High-Temperature Magnetization	44
2.3 Mössbauer Spectrometer	45
CHAPTER III - RESULTS AND DISCUSSIONS	
3.1 Electrical Resistivity	57
3.2 Magnetoresistance	68
3.3 Low-Temperature Magnetization	80
3.4 High-Temperature Magnetization	86
3.5 Mössbauer Spectroscopy	97
CHAPTER IV - CONCLUSIONS	122
REFERENCES	126

LIST OF FIGURES

	Page No.
Fig. 1.1 (a) Schematic energy level diagram of free atom or nucleus (b) Intensity $I(E)$ of spectral line as a function of transition energy E .	27
Fig. 1.2 Overlap of the emission and absorption lines showing the relation between E_o , E_γ^s , and E_γ^a for two cases: (a) optical case $E_R \ll \Gamma$ (b) nuclear case $E_R \gg \Gamma$.	30
Fig. 1.3 Decay scheme of ^{57}Co to ^{57}Fe .	32
Fig. 1.4 (a) Effect of monopole interaction on the energy levels of source and absorber (b) Mössbauer spectrum showing monopole interaction.	35
Fig. 1.5 Effect of magnetic hyperfine interaction on energy levels of ^{57}Fe . Peak positions of the six-finger pattern are shown at the bottom (C=Centroid).	40
Fig. 2.1 Schematic diagram of electrical resistivity set-up.	42
Fig. 2.2 Schematic block diagram of Mössbauer spectrometer.	46
Fig. 2.3 Schematic diagram of electromechanical velocity transducer.	48
Fig. 2.4 Three-peak pulse height spectrum of ^{57}Co source.	52
Fig. 3.1 Temperature dependence of the normalized resistivity r for amorphous $\text{Fe}_{80}\text{B}_{20-x}\text{Si}_x$ ($x = 0, 1, 2$, and 4) alloys. Each curve is displaced along the r axis by 0.01 with respect to the one below it.	58
Fig. 3.2 Temperature dependence of the normalized resistivity r for amorphous $\text{Fe}_{80}\text{B}_{20-x}\text{Si}_x$ ($x = 6, 8$, and 12) alloys. Each curve is	59

displaced along r the axis by 0.01 with respect to the one below it.

Fig. 3.3 Deviation versus temperature for $x = 0, 1, 6$, and 12 alloys. (a) denotes deviations of data points from fits to Eq. (1.7a) and (b) from fits to Eq. (1.7b). 64

Fig. 3.4 Temperature derivative of the normalized resistivity dr/dT (10^{-5} K^{-1}) as a function of temperature for $x = 0, 2, 6$, and 8 alloys. Each curve is displaced along the dr/dT axis by 10^{-4} with respect to the one below it. 65

Fig. 3.5 Magnetoresistance ($\Delta\rho/\rho$) versus external magnetic field at several constant temperatures for both longitudinal ($\vec{J} \parallel \vec{M}$) & transverse ($\vec{J} \perp \vec{M}$) orientations for $x = 0$. 69

Fig. 3.6 Magnetoresistance ($\Delta\rho/\rho$) versus external magnetic field at several constant temperatures for both longitudinal ($\vec{J} \parallel \vec{M}$) & transverse ($\vec{J} \perp \vec{M}$) orientations for $x = 6$. 70

Fig. 3.7 Magnetoresistance ($\Delta\rho/\rho$) versus external magnetic field at several constant temperatures for both longitudinal ($\vec{J} \parallel \vec{M}$) & transverse ($\vec{J} \perp \vec{M}$) orientations for $x = 12$. 71

Fig. 3.8 (a) Ferromagnetic anisotropy of resistivity (FAR) versus temperature for $x = 0, 6$, and 12. Linear magnetostriction coefficient λ_s is also shown for $x = 0$.
(b) High field slope ($\rho^{-1}d\rho/dH$) versus temperature for $x = 0, 6$, and 12 for some orientations. L and T in brackets refer to longitudinal and transverse orientations respectively. 73

Fig. 3.9 Temperature dependence of electrical resistance $R(T)$ at constant external magnetic fields of 2, 7, and 14 kOe for $x =$ 78

6. The curves are shifted along the R axis for clarity. The inset shows $\Delta R = R(T, 14 \text{ kOe}) - R(T, 7 \text{ kOe})$ versus temperature.

- Fig. 3.10 Magnetization M versus external magnetic field H at room temperature and at 19 K for $\text{Fe}_{80}\text{B}_{20-x}\text{Si}_x$ ($x = 0, 6, \text{ and } 12$) alloys. 81
- Fig. 3.11 Normalized magnetization $\sigma(T)/\sigma(0)$ versus temperature for amorphous $\text{Fe}_{80}\text{B}_{20-x}\text{Si}_x$ ($x = 0, 6, \text{ and } 12$) alloys. The curves are shifted along the σ axis for clarity. The solid curves are fits of the experimental data to Eq. (1.36). 83
- Fig. 3.12 Low-field magnetization M at $H \simeq 30 \text{ Oe}$ as a function of temperature for amorphous $\text{Fe}_{80}\text{B}_{20-x}\text{Si}_x$ ($x = 0 \text{ and } 4$) alloys. 87
- Fig. 3.13 Low-field magnetization M at $H \simeq 30 \text{ Oe}$ as a function of temperature for amorphous $\text{Fe}_{80}\text{B}_{20-x}\text{Si}_x$ ($x = 1 \text{ and } 12$) alloys. 88
- Fig. 3.14 Low-field magnetization M at $H \simeq 30 \text{ Oe}$ as a function of temperature for amorphous $\text{Fe}_{80}\text{B}_{20-x}\text{Si}_x$ ($x = 2 \text{ and } 6$) alloys. 89
- Fig. 3.15 (a) Curie temperature T_C versus x (b) Crystallization temperature T_x versus x for amorphous $\text{Fe}_{80}\text{B}_{20-x}\text{Si}_x$ ($x = 0, 1, 2, 4, 6, 8, \text{ and } 12$) alloys. 93
- Fig. 3.16 X-ray diffraction pattern after low-field, high-temperature magnetization studies for $\text{Fe}_{80}\text{B}_{20-x}\text{Si}_x$ ($x = 0, 1, 4, \text{ and } 8$) alloys. 95
- Fig. 3.17 Mössbauer spectra recorded at room temperature of as-received $\text{Fe}_{80}\text{B}_{20-x}\text{Si}_x$ ($x = 0, 2, \text{ and } 8$) alloys. 98
- Fig. 3.18 (a) Plot of isomer shift (I.S.) [measured with respect to $\alpha\text{-Fe}$] versus x (b) Internal magnetic field H versus x for amorphous $\text{Fe}_{80}\text{B}_{20-x}\text{Si}_x$ ($x = 0, 2, \text{ and } 8$) alloys. 100
- Fig. 3.19 Mössbauer spectra recorded at room temperature of $\text{Fe}_{80}\text{B}_{20}$, heat-treated at : 103

(a) 300°C (1 hr) (b) 300°C (2 hr) (c)
350°C (1 hr) (d) 350°C (2 hr).

Fig. 3.20 Mössbauer spectra recorded at room 105

temperature of $\text{Fe}_{80}\text{B}_{20}$, heat-treated at :
(a) 400°C (1 hr) (b) 400°C (4 hr), fitted
into four sub spectra. The symbols ●, ○, △,
□, and ▽ refer to raw spectra, I, II, III,
and IV sextet, respectively of Table 3.6.

Fig. 3.21 X-ray diffraction pattern at room 107

temperature, of $\text{Fe}_{80}\text{B}_{20-x}\text{Si}_x$, with $x = 0$
annealed at 400°C (4 hr), $x = 2$ at 475°C (4
hr), and $x = 8$ at 525°C (4 hr) after
Mössbauer measurements.

Fig. 3.22 Mössbauer spectra recorded at room 110

temperature of $\text{Fe}_{80}\text{B}_{18}\text{Si}_2$, heat-treated at :
(a) 300°C (1 hr) (b) 300°C (2 hr) (c) 350°C
(1 hr) (d) 350°C (2 hr) (e) 400°C (1 hr)
(f) 400°C (2 hr).

Fig. 3.23 Mössbauer spectra recorded at room 111

temperature of $\text{Fe}_{80}\text{B}_{18}\text{Si}_2$, heat-treated at :
(a) 475°C (1 hr) (b) 475°C (4 hr), fitted
into four sub spectra. The symbols ●, ○, △,
□, and ▽ refer to raw spectra, I, II, III,
and IV sextet, respectively of Table 3.8.

Fig. 3.24 Mössbauer spectra recorded at room 114

temperature of $\text{Fe}_{80}\text{B}_{12}\text{Si}_8$, heat-treated at :
(a) 300°C (1 hr) (b) 300°C (2 hr) (c) 350°C
(1 hr) (d) 350°C (2 hr).

Fig. 3.25 Mössbauer spectra recorded at room 115

temperature of $\text{Fe}_{80}\text{B}_{12}\text{Si}_8$, heat-treated at :
(a) 400°C (1 hr) (b) 400°C (2 hr) (c) 475°C
(1 hr) (d) 475°C (4 hr).

Fig. 3.26 Mössbauer spectra recorded at room 118

temperature of $\text{Fe}_{80}\text{B}_{12}\text{Si}_8$, heat-treated at :
(a) 525°C (1 hr) (b) 525°C (4 hr), fitted
using model A. The symbols ●, ○, and △

refer to raw spectra, I, and II sextet, respectively of Table 3.9.

Fig. 3.27 Mössbauer spectra recorded at room temperature of $\text{Fe}_{80}\text{B}_{12}\text{Si}_8$, heat-treated at : 119
 (a) 525°C (1 hr) (b) 525°C (4 hr), fitted using model B. The symbols \bullet , \circ , Δ , \square , and ∇ refer to raw spectra, I, II, III, and IV sextet, respectively of Table 3.9.

LIST OF TABLES

	Page No.
Table 3.1 Composition, coefficients for fits to Eq. (1.7) and resulting χ^2 coefficients for fits to Eqs. (1.8) and (1.9b) and resulting χ^2 and values of θ_D obtained from Eqs. (1.10)-(1.12) in $\text{Fe}_{80}\text{B}_{20-x}\text{Si}_x$ ($0 \leq x \leq 12$) amorphous ferromagnets.	61
Table 3.2 Magnetic field dependence of the coefficients of the magnetic terms [Eqs. (1.7b) and (1.8b)] in $\text{Fe}_{80}\text{B}_{20-x}\text{Si}_x$ ($x = 0, 6, \text{ and } 12$) amorphous ferromagnets.	79
Table 3.3 Comparison of σ (19 K), β , D, and $\bar{\mu}$ in $\text{Fe}_{80}\text{B}_{20-x}\text{Si}_x$ ($x = 0, 6, \text{ and } 12$) amorphous ferromagnets.	85
Table 3.4 X-ray analysis of $\text{Fe}_{80}\text{B}_{20-x}\text{Si}_x$ ($x = 0, 1, 2, 4, 6, \text{ and } 8$) after high-temperature magnetization studies.	96
Table 3.5 Mössbauer parameters, obtained from computer analysis, for the as-received $\text{Fe}_{80}\text{B}_{20-x}\text{Si}_x$ ($x = 0, 2, \text{ and } 8$) amorphous ferromagnets.	99
Table 3.6 Mössbauer parameters, obtained from computer analysis, for $x = 0$ sample after various heat treatments.	102
Table 3.7 X-ray analysis of crystallized $\text{Fe}_{80}\text{B}_{20-x}\text{Si}_x$ ($x = 0, 2, \text{ and } 8$) alloys after Mössbauer measurements.	106
Table 3.8 Mössbauer parameters, obtained from computer analysis, for $x = 2$ sample after various heat treatments.	112
Table 3.9 Mössbauer parameters, obtained from computer analysis, for $x = 8$ sample after various heat treatments.	116

CHAPTER I

INTRODUCTION

1.1 Preamble

The terms amorphous solid and glass have no precise meaning. These terms are generally accepted to mean "not crystalline on any significant scale". However, not all disordered materials are amorphous since there are disordered crystalline alloys where different atoms irregularly occupy sites of a regular crystal lattice. Amorphous solids have both structural disorder, i.e., the lack of crystallinity and chemical disorder which refers to the local environment. They are made by a variety of techniques, all of which involve rapid solidification of the alloying constituents from the gas or liquid phases. The solidification occurs so rapidly that the atoms are frozen in their liquid configuration. There are clear structural indications and indications from the various properties that nearest neighbour or local order does exist in most amorphous metallic alloys, but there is no long-range atomic order.

Because of the lack of atomic ordering it was believed for many years that ferromagnetism could not exist in amorphous alloys. But, for a material to be magnetic, all that is necessary is the existence of a magnetic moment (and therefore uncompensated spins) on an atom and the requirement that when these atoms are assembled in a solid, they interact via the short-range exchange forces. However, it was only in 1960 that Gubanov [1] theoretically foresaw the existence of ferromagnetism in an amorphous solid. This was based on the evidence that the

electronic band structure of crystalline solids do not change in any fundamental way on transition to the liquid state. This implies that the band structure is more dependent on short-range, rather than on long-range order. Hence, ferromagnetism, which depends on short-range order, should not be destroyed in the corresponding amorphous solid. After this important prediction was made, intense experimental and theoretical activities have pervaded the field.

Until recently the major efforts in solid-state physics have been confined to the understanding of crystalline materials. Amorphous solids now represent a new state of matter. Some of their properties are entirely as predicted but some others show anomalous behaviour. The most significant experimental results reported in the recent literature are the large absolute values of electrical resistivity, very small values of ferromagnetic anisotropy of resistivity and nearly temperature-independent anomalous Hall coefficient. Much of our understanding has come from comparison of the properties of the amorphous alloys with those of the same or similar crystalline alloys. However, this has only limited applicability because most of the interesting amorphous alloys have no simple or single crystalline counterpart. One of the singular advantages of studying amorphous alloys is that we can vary the composition continuously in preparing homogeneous alloys which can be studied as a function of composition and temperature without complicating interference from structural phase transitions. Interest in metallic glasses was accelerated because of the occurrence of ferromagnetism in them, hence, the study of magnetic properties bears a special

significance.

The electrical resistivity in metallic glasses is a very important subject as the non-crystallinity of the materials affects the electronic transport properties. In recent years, the study of these properties has been a subject of widespread interest. In particular, the electrical resistivity provides a very sensitive probe with which one can try to understand various scattering processes that occur in a given material.

Earlier [2] we had measured electrical resistivity (ρ), magnetoresistance, and Hall effect in $\text{Fe}_{100-x}\text{B}_x$ ($13 \leq x \leq 26$) binary metallic glasses. The temperature coefficient of resistivity and the concentration dependence of the absolute value of ρ were explained in terms of Ziman's theory [3] of liquid metals. An attempt was also made to find out the magnetic contribution to the resistivity between 20 and 100 K. Due to the relatively poor resolution of the data, no definite conclusion could be drawn. However, in magnetic materials, over and above the scattering of electrons by structural disorders and lattice vibrations, there must be some evidence of magnetic scattering. Theoretically, according to Richter et al. [4], the leading term in the magnetic resistivity of amorphous ferromagnets is a $T^{3/2}$ one followed by a higher-order T^2 term. An excellent review has been made recently by Vasvári [5]. Experiments which claim to have observed a magnetic contribution to ρ fall under two categories.

(a) A magnetic contribution proportional to T^2 . Bergmann and Marquardt [6] had concluded the existence of a T^2 -dependent magnetic term on the basis of straight-line plots of ρ versus T^2

in binary Ni-Au, Co-Au, and Fe-Au amorphous ferromagnets. This method is not conclusive since the structure factor term (see Sec. 1.2), which should be included in the total ρ , also has a T^2 dependence. Thummes et al. [7] found qualitative evidence of a T^2 magnetic term in $\text{Ni}_{80-x}\text{Fe}_x\text{Si}_8\text{B}_{12}$ ($2.4 \leq x \leq 16$) metallic glasses. They also found an unusually low Debye temperature ($\theta_D < 100$ K). Kaul et al. [8] have established, from a detailed quantitative analysis of the resistivity data of amorphous $\text{Fe}_{80}\text{B}_{20-x}\text{C}_x$ ($x = 0, 2, 4, \text{ and } 10$) alloys, that besides a dominant structural contribution there exists in such alloys a significant magnetic contribution to ρ proportional to T^2 .

(b) A magnetic contribution proportional to $T^{3/2}$. In Fe-Ni-P-B glasses, Babic et al. [9] obtained a $T^{3/2}$ term from linear total ρ versus $T^{3/2}$ plots for $T < T_C/3$. No structural contribution was considered. Kettler and Rosenberg [10] found a $T^{3/2}$ magnetic term in Ni-based $\text{Ni}_{80-x}\text{Fe}_x\text{B}_{16}\text{Si}_4$ ($x = 0 - 19$) and $\text{Ni}_{77-x}\text{Fe}_x\text{B}_{13}\text{Si}_{10}$ ($x = 0 - 15.4$) by subtracting at each temperature the total resistivity of the nickel parent alloy ($x = 0$) from those of the above alloys. This was done on the assumption that the magnetic contribution to the total ρ was due to the added iron. They also found that the magnetic term decreased with increasing Fe content.

Thus, it is quite clear that a controversy still exists in deciding the relative weight of the $T^{3/2}$ and T^2 magnetic contributions to the total resistivity in ferromagnetic metallic glasses. It should be emphasized here that such distinctions can not be made by merely observing ρ versus $T^{3/2}$ or ρ versus T^2 curves as straight lines. A quantitative criterion, e.g., the value of χ^2 in different fits, is needed as it has been used only

by Kaul et al. [8].

We have taken high-resolution electrical resistivity $\rho(T)$ data in seven $\text{Fe}_{80}\text{B}_{20-x}\text{Si}_x$ ($0 \leq x \leq 12$) ferromagnetic metallic glasses between 8 and 300 K with the following aim.

- (a) To determine whether there is any magnetic contribution at all in these materials.
- (b) If there is, does it occur through a $T^{3/2}$ term which is theoretically [4] the leading term in amorphous materials or through a T^2 term as found quantitatively by Kaul et al. [8] in a similar system ?

The measurement of magnetoresistance is useful in getting information about the magnetization process. With the study of magnetoresistance, the effect of magnetic field on various magnetic scattering can be probed to see whether the same temperature dependence of resistivity holds as in the zero-field case. $R(T)$ data have been taken at several constant magnetic fields. We propose, on the basis of analysis of the resistivity data, that at low temperatures, the magnetic contribution to the resistivity is through the $T^{3/2}$ term. With this sort of investigation, the effect of magnetic field on this magnetic contribution is studied. The quantity $(\frac{\rho_{\parallel s} - \rho_{\perp s}}{\rho})$ or $(\frac{\Delta\rho}{\rho})$, known as the ferromagnetic anisotropy of resistivity (FAR), represents an inherent property of the amorphous ferromagnetic alloys. It has been known for quite a long time that there exists ferromagnetic anisotropy of resistivity associated with the magnetization in ferromagnetic metals. Smit [11] had proposed a mechanism dependent on spin-orbit coupling to explain this phenomenon. Recently, a few papers [12-16] have appeared on the ferromagnetic

anisotropy effect. From the temperature dependence of FAR, Böhnke et al. [17] had suggested a direct relationship ($\Delta\rho/\rho = A\bar{\mu}^m$) between FAR and the saturation magnetization where $\bar{\mu}$ is the average saturation magnetic moment per transition metal atom. Until recently many authors [12-17] have observed that $\Delta\rho/\rho$ tends to track the magnetic moment in amorphous alloys. Kaul and Rosenberg [18] have pointed out, however, that FAR cannot be related to the saturation magnetic moment per transition metal atom by such a simple relation. From a detailed investigation of FAR of amorphous $(\text{Fe-Ni})_{80}\text{B}_{20}$ and $(\text{Fe-Ni})_{80}\text{P}_{14}\text{B}_6$ alloys, they have shown that the split-band (SB) model which could give a satisfactory explanation for the observed composition dependence of the linear saturation magnetostriction coefficient λ_s , spontaneous Hall coefficient R_s , and the coefficient of the electronic specific heat γ_s in these amorphous alloy series, fail to explain their observations. They have applied successfully the model based on two-current conduction (TCC), given by Campbell et al. [19], for the composition dependence of the FAR of these alloys. Magnetoresistance, both transverse and longitudinal, has been measured for $x = 0, 6$, and 12 between 10 and 300 K using magnetic fields up to 16.5 kOe in order to study the effect of the replacement of B by Si on FAR. In these measurements, the temperature dependence of FAR is also investigated.

As these glassy metals are metastable materials, they undergo a change of phase from the glassy, i.e., amorphous to the crystalline state at high temperatures. The crystallization process is quite complicated. As it is a kinetic process, it is not only temperature-dependent but also time-dependent. The study

of crystallization process gives important clues about the local structure of these glasses. The metallurgical changes, which occur when crystallization begins, were detected by using the magnetization versus temperature (M-T) curves. The magnetization falls with increasing temperature, typically to $M = 0$ at $T = T_C$. When crystallization starts, iron and some compounds, with high T_C values, appear causing an increase in M. The beginning of this rise in M is taken as the onset of crystallization. The equilibrium phases, present in any particular amorphous alloy, can be specified by identifying the Curie temperatures (T_C) of the different crystalline phases found in it. Here the thermomagnetic as well X-ray diffraction studies are used to explore the crystallization process of $\text{Fe}_{80}\text{B}_{20-x}\text{Si}_x$ ($0 \leq x \leq 12$) amorphous alloys. It is quite important to get the information concerning the structural changes with temperature for understanding the temperature dependence of various physical properties of amorphous materials. However, this bulk magnetization study measures only the sum of the magnetizations of all the magnetic components present in the sample. The purpose of the present work is to elucidate systematically the effect of the metalloid Si on the crystallization mechanism of Fe-B amorphous alloys. It was possible to use the thermomagnetic analysis for meaningful crystallization studies here because the Curie temperatures in the amorphous state happen to fall below the crystallization temperatures.

Mössbauer spectroscopic study, which reveals the properties of and distinguishes between all iron-nuclei belonging to different chemical compounds, becomes an ideal tool for the

investigation of the kinetics of the crystallization process. As these amorphous alloys are not very stable, their various properties such as the magnetic hyperfine field [20] and the Curie temperature are significantly changed by annealing treatments which do not cause crystallization. Furthermore, annealing at elevated temperatures inevitably causes crystallization irreversibly due to which the excellent characteristics inherent in the amorphous structure are lost. The systematic analysis of the Mössbauer spectra gives various Mössbauer parameters like isomer shift and internal magnetic fields at ^{57}Fe nuclei which, in turn, provide valuable information about the hyperfine interactions in these materials. The study of internal magnetic fields at the nuclear sites has been very useful in understanding their magnetic properties at the atomic level.

Here Mössbauer spectroscopy has been used to study the crystallization and the crystallized phases of $\text{Fe}_{80}\text{B}_{20-x}\text{Si}_x$ ($x = 0, 2, \text{ and } 8$) amorphous alloys. Precipitation of a crystallized phase containing the Mössbauer atom can be easily detected since it gives rise to a new set of inequivalent sites which have their own characteristic spectrum. Upon crystallization, the Mössbauer spectrum of an amorphous alloy becomes more complex (than the usual six-line pattern) due to the precipitation of two or more crystalline phases containing Mössbauer nuclei. Therefore, Mössbauer spectroscopy can be used to detect the onset of the crystallization process as well as to identify the various crystalline phases containing Mössbauer nuclei which exist after full crystallization has taken place.

The most extensively studied glasses are the binary

ones, $\text{Fe}_{1-x}\text{B}_x$ ($x < 0.25$), especially $\text{Fe}_{80}\text{B}_{20}$ because they are the simplest possible amorphous system. Two types of crystallization processes have been observed in these simple binary alloys. The first type [21-23] has been observed for amorphous Fe-B alloys with B concentration of less than 16 at.% and it consists of two steps. The first step of the crystallization is a precipitation of $\alpha\text{-Fe}$ until the composition of the remaining glasses transforms into a Fe_3B metastable compound. The second step is the decomposition of Fe_3B at higher temperatures into $\alpha\text{-Fe}$ and Fe_2B . The second type [21,23,24] of crystallization has been observed for amorphous Fe-B alloys with B concentration of more than about 16 at.% and consists of a single step, the crystallization takes place by an eutectic type of reaction. The two crystalline phases, $\alpha\text{-Fe}$ and Fe_3B are produced from the very beginning of the crystallization process and the $\alpha\text{-Fe}$ to Fe_3B ratio is constant throughout the transformation. In $\text{Fe}_{80}\text{B}_{20}$ [24-28] and $\text{Fe}_{78}\text{B}_{12}\text{Si}_{10}$ [29] alloy, $\alpha\text{-Fe}$ has been reported to precipitate during the crystallization process. However, it has been found out [20,30,31] that a Fe-Si alloy, instead of $\alpha\text{-Fe}$, is one of the crystalline products in a Fe-B-Si system. The study of the crystallization in $x = 2$ and 8 ($\text{Fe}_{80}\text{B}_{20-x}\text{Si}_x$) alloys has been done to confirm the final phases, i.e., whether one of the phases is $\alpha\text{-Fe}$ or Fe-Si or both.

The fundamental problem of ferromagnetism, from both the theoretical and experimental standpoints, is the determination of magnetization as a function of composition, magnetic field, and temperature. The most interesting problem is the temperature dependence of magnetization. Majumdar et al. [32] have shown the

evidence for the existence of a $T^{5/2}$ term in the low-temperature magnetization of $\text{Fe}_{80}\text{B}_{20-x}\text{C}_x$ ($0 \leq x \leq 8$) metallic glasses. They have also shown that the addition of carbon increases the spin-wave stiffness constant due to structural changes. We also wanted to study the effect of Si concentration on spin wave stiffness constant.

1.2 Theory

A Electrical Resistivity

Customarily the temperature dependence of electrical resistivity $\rho(T)$ in amorphous materials is explained in terms of the Ziman theory of liquid metals in which the temperature dependence of resistivity comes through the structure factor. An expression for $\rho(T)$ can be written as [3]

$$\rho_{\text{str}}(T) = \frac{30\pi^3 \hbar^3}{m e^2 k_F^2 E_F \Omega} \sin^2[\eta_2(E_F)] \times \left\{ 1 + [S_0(2k_F) - 1] e^{-2(W(T) - W(0))} \right\}, \quad (1.1)$$

where k_F is the Fermi wave vector, Ω is the atomic volume, $W(T)$ is Debye-Waller factor at a temperature T , $\eta_2(E_F)$ is the d -partial-wave phase shift at the Fermi energy E_F , $S_0(2k_F)$ is the structure factor at 0 K, corresponding to $k = 2k_F$ and \hbar , m and e have their usual meanings. The asymptotic temperature dependence of $W(T)$ in the Debye approximation is given by

$$W(T) = \begin{cases} W(0) + 4W(0) \frac{\pi^2}{6} \left[\frac{T}{\theta_D} \right]^2, & T \ll \theta_D, \end{cases} \quad (1.2a)$$

$$W(T) = \begin{cases} W(0) + 4W(0) \left[\frac{T}{\theta_D} \right], & T \geq \theta_D, \end{cases} \quad (1.2b)$$

$$\text{where } W(0) = \frac{3}{8} \frac{\hbar^2 k_F^2}{M k_B \theta_D}, \quad (1.3)$$

M is the atomic mass, k_B is the Boltzmann constant, and θ_D is the Debye temperature. An estimate of $W(0)$, obtained by substituting the values $\theta_D \cong 300\text{K}$, $M \simeq 8 \times 10^{-23}\text{g}$ and $E_F \simeq 10\text{ eV}$, typical of metallic glasses, in Eq. (1.3), shows that $W(0) \leq 1$. Eqs. (1.1) and (1.2) can be combined and the exponential function in Eq. (1.1) expanded in power series to yield the asymptotic temperature dependence of ρ_{str} as

$$\rho_{\text{str}}(T) = C \left\{ S_0(2k_F) + \left[\frac{2\pi}{\theta_D} \right]^2 \frac{W(0)}{3} [1 - S_0(2k_F)] T^2 \right\}, \quad T \ll \theta_D, \quad (1.4a)$$

$$= C \left\{ S_0(2k_F) - 2W(0) [1 - S_0(2k_F)] + \frac{8W(0)}{\theta_D} [1 - S_0(2k_F)] T \right\}, \quad T \geq \theta_D, \quad (1.4b)$$

$$\text{where } C = \frac{30 \pi^3 \hbar^3}{m e^2 k_F^2 E_F \Omega} \sin^2[\eta_2(E_F)].$$

Eqs. (1.4a) and (1.4b), in the simplified form, can be

written as

$$r_s(T) = \rho_s(T)/\rho(0^\circ\text{C}) = a_0 + b_2 T^2, \quad T \ll \theta_D, \quad (1.5a)$$

$$= a'_0 + c_1 T, \quad T \geq \theta_D, \quad (1.5b)$$

where $\rho(0^\circ\text{C})$, the resistivity at 273 K, is used for normalizing the data.

Richter et al. [4] have calculated the spin-disorder resistivity of amorphous ferromagnets by using the force-force correlation function method up to second order in the s - d exchange constant. They found, at low temperatures ($T \ll T_C$, where T_C is the Curie temperature) and zero external field, that

$$r_m(T) = \rho_m(T)/\rho(0^\circ\text{C}) = \rho_0 + aT^{3/2} + bT^2, \quad (1.6)$$

neglecting a small correction to the electron-magnon coherent scattering due to the influence of topological disorder. ρ_0 is proportional to the residual spin-disorder resistivity. The $T^{3/2}$ dependence comes from (a) the elastic scattering of electrons by a temperature-dependent, randomly distributed local magnetic moments which decreases with increasing temperature and (b) incoherent electron-magnon momentum nonconserving scattering which increases with increasing temperature. The latter term overcompensates the former and, as a result, the net $T^{3/2}$ term is positive. However, this term vanishes for the crystalline case. The T^2 term comes from the coherent electron-magnon scattering, as in the crystalline case. For low T ($\ll \theta_D$), the contribution should be predominantly from the $T^{3/2}$ term whereas, for moderate

$T (\simeq \theta_D)$, it should be from the T^2 term. In both the cases it is assumed that $T \ll T_C$.

If the magnetic contribution occurs through the T^2 term, then assuming Mathiessen's rule

$$\rho(T) = \rho_s(T) + \rho_m(T),$$

the total normalized resistivity becomes [by adding Eqs. (1.5a) and (1.6), except for the $T^{3/2}$ term]

$$\begin{aligned} r(T) &= (a_0 + \rho_0) + (b_2 + b) T^2 \\ &= \alpha_0 + \alpha_2 T^2, \quad T \ll \theta_D. \end{aligned} \quad (1.7a)$$

If the magnetic contribution occurs through the $T^{3/2}$ term, then [by adding Eqs. (1.5a) and (1.6), except for the T^2 magnetic term]

$$\begin{aligned} r(T) &= (a_0 + \rho_0) + b_2 T^2 + a T^{3/2} \\ &= \alpha_0 + \alpha_2 T^2 + \alpha_{3/2} T^{3/2}, \quad T \ll \theta_D. \end{aligned} \quad (1.7b)$$

Similarly, by adding Eqs. (1.5b) and (1.6), one gets

$$\begin{aligned} r(T) &= (a'_0 + \rho_0) + c'_1 T + b T^2 \\ &= \alpha'_0 + \alpha'_1 T + \alpha'_2 T^2, \quad T \geq \theta_D \end{aligned} \quad (1.8a)$$

and

$$\begin{aligned} r(T) &= (a'_0 + \rho_0) + c'_1 T + a T^{3/2} \\ &= \alpha'_0 + \alpha'_1 T + \alpha'_{3/2} T^{3/2}, \quad T \geq \theta_D. \end{aligned} \quad (1.8b)$$

If the magnetic contribution is not considered at all, then

$$r(T) = \alpha_0 + \alpha_2 T^2, \quad T \ll \theta_D \quad (1.9a)$$

and

$$r(T) = \alpha'_0 + \alpha'_1 T, \quad T \geq \theta_D \quad (1.9b)$$

Using Eqs. (1.9), i.e., without considering any magnetic contribution, one gets

$$\theta_D^1 \approx \frac{\pi^2}{6} \frac{\alpha'_1}{\alpha_2} \quad (1.10)$$

If we consider Eqs. (1.7a) and (1.8a), i.e., the magnetic term is proportional to T^2 in both ranges of temperature, θ_D will be given by

$$\theta_D^2 \approx \frac{\pi^2}{6} \frac{\alpha'_1}{\alpha_2 - \alpha'_2} \quad (1.11)$$

If we consider that the magnetic term goes as $T^{3/2}$ in both ranges of temperature, then the value of θ_D can be found, with use of Eqs. (1.7b) and (1.8b), to be

$$\theta_D^3 \approx \frac{\pi^2}{6} \frac{\alpha'_1}{\alpha_2} \quad (1.12)$$

B Magnetoresistance

The electrical resistivity of a polycrystalline ferromagnet depends on the angle between the current density \vec{J} and the magnetization \vec{M} . The longitudinal magnetoresistance ($\vec{J} \parallel \vec{M}$)

is positive while the transverse magnetoresistance ($\vec{J} \perp \vec{H}$) is negative at low fields. At higher fields there is a slow decrease in resistivity, i.e., a negative magnetoresistance is observed in both orientations. For a cubic single crystal the resistivity ρ can be written as [33]

$$\rho(\alpha_1, \beta_1) = a_0 + a_1 (\alpha_1\beta_1 + \alpha_2\beta_2 + \alpha_3\beta_3)^2 + 2(a_2 - a_1)(\alpha_1\alpha_2\beta_1\beta_2 + \alpha_2\alpha_3\beta_2\beta_3 + \alpha_3\alpha_1\beta_3\beta_1), \quad (1.13)$$

where α_1, α_2 , and α_3 are the direction cosines of the spontaneous magnetization with respect to the crystal axes and the resistivity is measured in a direction characterized by the direction cosines β_1, β_2 , and β_3 . The saturation values of ρ in a polycrystal for longitudinal and transverse magnetic fields can be calculated by taking the averages of Eq. (1.13) when all the spins are either parallel or perpendicular to the current. One can then write

$$\rho_{\parallel S} = a_0 + \frac{3}{5} a_1 + \frac{2}{5} a_2 \quad (1.14)$$

and

$$\rho_{\perp S} = a_0 + \frac{1}{5} a_1 - \frac{1}{5} a_2. \quad (1.15)$$

In random polycrystals, where all the orientations of magnetization with respect to the crystal axes are equally probable and the crystallites are oriented at random, the resistivity ρ_0 in the demagnetized state (zero internal field) can be written as

$$\rho_0 = \frac{1}{3} \rho_{\parallel S} + \frac{2}{3} \rho_{\perp S} = a_0 + \frac{a_1}{3}. \quad (1.16)$$

In this case

$$\frac{\rho_{\parallel S} - \rho_0}{\rho_{\perp S} - \rho_0} = \frac{\Delta\rho_{\parallel S}}{\Delta\rho_{\perp S}} = -2. \quad (1.17)$$

The assumptions introduced in the calculation of ρ_0 are strictly fulfilled only in rare cases. Because of the magnetocrystalline anisotropy, the spontaneous magnetization lies along the easy direction of magnetization. It is not equally distributed among all directions with respect to the crystal axes. Thus the ratio $\Delta\rho_{\parallel S}/\Delta\rho_{\perp S}$ depends completely on the orientation of this preferred axis.

Ferromagnetic Anisotropy of Resistivity (FAR)

Though the ratio $\Delta\rho_{\parallel S}/\Delta\rho_{\perp S}$ depends on the initial processing, subsequent heat treatment, etc., of the material, the quantity $(\Delta\rho_{\parallel S} - \Delta\rho_{\perp S})$ does not depend on the initial magnetic domain structure and hence is a very important inherent property of a ferromagnet. This difference, which is practically always positive, is known as the anisotropic magnetoresistance. The experimentally measured quantity is the relative change in resistivity between the two orientations, $\Delta\rho/\rho_0$, and is called the ferromagnetic anisotropy of resistivity, FAR. Thus

$$\text{FAR} = \frac{\Delta\rho}{\rho_0} = \frac{\rho_{\parallel S} - \rho_{\perp S}}{\rho_0}, \quad (1.18)$$

where ρ_0 , the resistivity in the demagnetized state, can be written from Eq. (1.16) as

$$\rho_0 = \rho + \frac{1}{3} \Delta\rho_{\parallel s} + \frac{2}{3} \Delta\rho_{\perp s}, \quad (1.19)$$

where ρ is the resistivity for $H_{\text{ext}} = 0$. In a ferromagnet, because of the presence of spontaneous magnetization within each Weiss domain, the effective magnetic field is given by

$$H_{\text{eff}} = H_{\text{int}} = H_{\text{ext}} - H_{\text{demag}} = H_{\text{ext}} - \alpha (4\pi M_s), \quad (1.20)$$

where α is the demagnetization factor which depends on the relative orientation of the magnetic field with respect to the dimensions of the sample and M_s is the saturation magnetization at a particular temperature.

As stated earlier, to get ρ_0 , one has to do some kind of averaging over all the possible orientations of the spontaneous domain magnetization. In metallic glasses, since we have a uniaxial anisotropy and the domains are not at all random, it is very difficult to do such averaging. However, fortunately enough these materials have very small magnetoresistance and thus instead of calculating ρ_0 we can use

$$\rho_0 = \rho \quad . \quad (1.21)$$

Thus Eq. (1.18) can be written as

$$\text{FAR} = \frac{\Delta\rho}{\rho} = \frac{\rho_{\parallel s} - \rho_{\perp s}}{\rho} \quad . \quad (1.22)$$

To get the anisotropic magnetoresistance $(\rho_{\parallel s} - \rho_{\perp s})$ in terms of the measured quantities we can write

$$\rho_{\parallel S} = \rho + \Delta\rho_{\parallel S} = \rho \left[1 + \frac{\Delta\rho_{\parallel S}}{\rho} \right] \quad (1.23)$$

and

$$\rho_{\perp S} = \rho + \Delta\rho_{\perp S} = \rho \left[1 + \frac{\Delta\rho_{\perp S}}{\rho} \right] \quad (1.24)$$

and thus

$$\rho_{\parallel S} - \rho_{\perp S} = \left[\frac{\Delta\rho_{\parallel S}}{\rho} - \frac{\Delta\rho_{\perp S}}{\rho} \right] \rho, \quad (1.25)$$

where $\frac{\Delta\rho_{\parallel S}}{\rho}$ and $\frac{\Delta\rho_{\perp S}}{\rho}$ are obtained by extrapolating $\Delta\rho/\rho$ versus H_{ext} plots to $H_{\text{ext}} = H_{\text{demag}}$ such that $H_{\text{int}} = 0$.

Hence, in terms of experimentally measured quantities, FAR [Eq. (1.22)] can be written as

$$\text{FAR} = \frac{\Delta\rho_{\parallel S}}{\rho} - \frac{\Delta\rho_{\perp S}}{\rho} \quad (1.26)$$

Origin of FAR

According to Mott's theory, 4s-electrons are mainly the carriers of current in ferromagnetic materials. It was assumed that during a transition from an s to an s- or a d-state, there is no spin-flip and therefore the spin exchange between the s-electrons can be ignored. According to this assumption, the current is divided into two independent parts, one current of the s-electrons with parallel (to the magnetization) spin direction and the other with antiparallel spin. This model is referred as the two-current conduction (TCC) model. The effect of magnetic field on the resistance can be understood as a decrease in the

density of the parallel 3d-states at the Fermi surface with increasing magnetization which results in less scattering of s-electrons with parallel spin to d-states.

Smit [11] showed that an anisotropy in resistance could be introduced only through the interaction between the spin-system and the lattice via the spin-orbit coupling. Due to this coupling, there will be some mixing of parallel and antiparallel states. As a result even at $T = 0$ K, there will be vacant parallel d-states. On general grounds, it is seen that these holes are not equally distributed over the 5 possible d-orbitals, but there is a deficit of hole-orbits perpendicular to the direction of magnetization. So, even at 0 K, there will be some resistance which is responsible for the anisotropy.

The transition for an s-electron in going to a d-state is caused by lattice disorder or lattice vibrations. As there are relatively few holes in orbits perpendicular to the magnetization, the s-electrons moving in the direction of magnetization, are more easily trapped than in the perpendicular directions. As the resistance is given by the scattering of s-electrons moving in the direction of the current, it is concluded that the resistance in the parallel direction ($\vec{J} \parallel \vec{M}$) is greater than the one in the perpendicular direction ($\vec{J} \perp \vec{M}$), i.e., $R_{\parallel} > R_{\perp}$.

Campbell et al. [19], on the basis of this model, had obtained the following expression for the ferromagnetic anisotropy of resistivity at low temperatures for Ni-based alloys.

$$\frac{\Delta\rho}{\rho} = r(\alpha-1), \quad (1.27)$$

where $\alpha = \frac{\rho_{\downarrow}}{\rho_{\uparrow}}$ and $\gamma = \frac{3}{4} \left[\frac{\lambda}{H_{\text{ex}}} \right]^2$.

λ is the average value of the spin-orbit coupling constant in the d-band and H_{ex} is the exchange energy that splits d_{\uparrow} - and d_{\downarrow} -bands. Basically, γ is a measure of the strength of the spin-orbit coupling. The value of γ has been estimated to be ≈ 0.01 on the basis of experimental data on the FAR of Ni- and Fe-based alloys.

Formulation of θ , the angle between \vec{J} and \vec{M}

Since in metallic glasses, we have uniaxial anisotropy, i.e., the domains are preferentially oriented at some angle θ with respect to the ribbon axis, the resistivity in the demagnetised state can be expressed as

$$\rho_0 = \rho_{\perp s} \sin^2 \theta + \rho_{\parallel s} \cos^2 \theta, \quad (1.28)$$

where θ is the angle between \vec{J} and \vec{M} . Hence the longitudinal magnetoresistance is

$$\begin{aligned} \frac{\Delta \rho_{\parallel s}}{\rho_0} &= \frac{\rho_{\parallel s} - \rho_0}{\rho_0} = \frac{\rho_{\parallel s} - \rho_{\perp s} \sin^2 \theta - \rho_{\parallel s} \cos^2 \theta}{\rho_0} \\ &= \frac{(\rho_{\parallel s} - \rho_{\perp s}) \sin^2 \theta}{\rho_0}. \end{aligned}$$

or, $\frac{\Delta \rho_{\parallel s}}{\rho_0} = \text{FAR} \sin^2 \theta. \quad (1.29)$

Similarly, the transverse magnetoresistance is

$$\frac{\Delta\rho_{\perp S}}{\rho_0} = -\text{FAR} \cos^2\theta \quad . \quad (1.30)$$

From Eqs. (1.29) and (1.30), we get

$$\text{FAR} = \frac{\Delta\rho_{\parallel S}}{\rho_0} - \frac{\Delta\rho_{\perp S}}{\rho_0}$$

$$\text{and } \cot^2\theta = - \frac{\Delta\rho_{\perp S}/\rho_0}{\Delta\rho_{\parallel S}/\rho_0} \quad .$$

$$\text{or, } \tan^2\theta = - \frac{\Delta\rho_{\parallel S}/\rho_0}{\Delta\rho_{\perp S}/\rho_0} \quad . \quad (1.31)$$

Dependence of ρ on H above Saturation

This is purely ferromagnetic in origin. As observed by Smit [11], if we compare the change in resistance with the magnetostriction, then the linear saturation magnetostriction coefficient λ_s corresponds to the ferromagnetic anisotropy of resistivity, both being tensor, dependent on the orientation of the magnetization. In contrast, the volume magnetostriction corresponds to the small negative value of $\partial\rho/\partial H$ at high fields, independent of the orientation (longitudinal or transverse). It is clear that these volume effects are due to the increase of intrinsic magnetization with increasing field. The direct influence of the volume magnetostriction on resistance is very small [11] ($\frac{1}{\rho} \frac{d\rho}{dH}$ values are very small) and hence the effects observed are due to a change of the specific resistance. Assuming

that the resistivity depends only on the magnetization M_S , one can write

$$\frac{\partial \rho}{\partial H} = \left[\frac{\partial \rho}{\partial M_S} \right] \left[\frac{\partial M_S}{\partial H} \right] \quad (1.32)$$

Now, again assuming that ρ does not vary appreciably with magnetization M_S for normal fields, the dependence of $\partial \rho / \partial H$ on H is determined by that of $\partial M_S / \partial H$, the high field susceptibility, on H .

C Low-Temperature Magnetization

The low-temperature magnetization of a typical crystalline ferromagnet, according to the spin-wave theory, is in good approximation given by [34]

$$\frac{\Delta \sigma(T)}{\sigma(0)} = \frac{\sigma(T) - \sigma(0)}{\sigma(0)} = \beta T^{3/2} + \gamma T^{5/2} \quad (1.33)$$

The first term is the famous Bloch $T^{3/2}$ law, while the second one is due to higher order terms in magnon dispersion relation. The existence of spin waves in amorphous ferromagnets was proved by Kaneyoshi [35]. In amorphous structures the wave vector is not well defined and no simply defined Brillouin zone exists. Krey [36] assumed the structure of a metallic glass to be adequately described by a relaxed dense random packing of hard spheres and the localized spins to interact via a short-range Heisenberg interaction. With this assumption he has shown that the temperature dependence of the magnetization of an amorphous

ferromagnetic metallic glass is given by the same equation as Eq.(1.33).

The spin-wave dispersion relation, in the presence of a magnetic field H and in the long-wavelength limit ($k \rightarrow 0$), has the form [34]

$$\epsilon(k) = g\mu_B H + Dk^2 + Ek^4, \quad (1.34)$$

where g is the gyromagnetic factor, μ_B the Bohr magneton, k the wave vector, D the spin-wave stiffness constant, and E the constant of proportionality for the k^4 term. The first term in Eq. (1.34) is an energy gap in the magnon spectrum. One defines a gap temperature

$$T_g = \frac{g\mu_B H}{k_B}, \quad (1.35)$$

where k_B is the Boltzmann constant. Because of the energy gap in Eq. (1.34), Eq. (1.33) takes the form

$$\frac{\Delta\sigma(T)}{\sigma(0)} = \beta z \left[\frac{3}{2}, \frac{T_g}{T} \right] T^{3/2} + \gamma z \left[\frac{5}{2}, \frac{T_g}{T} \right] T^{5/2}. \quad (1.36)$$

The functions $z \left[\frac{3}{2}, \frac{T_g}{T} \right]$ and $z \left[\frac{5}{2}, \frac{T_g}{T} \right]$ are given by Argyle et al. [37]

$$z \left[\frac{3}{2}, \frac{T_g}{T} \right] = \frac{1}{2.612} \sum_{n=1}^{\infty} n^{-3/2} \exp \left[-n \frac{T_g}{T} \right]$$

$$\approx \frac{1}{2.612} \left\{ -3.54 \left[\frac{T_g}{T} \right]^{1/2} + 2.612 + 1.46 \frac{T_g}{T} - 0.104 \left[\frac{T_g}{T} \right]^2 + \dots \right\} . \quad (1.37)$$

$$z \left[\frac{5}{2} , \frac{T_g}{T} \right] = \frac{1}{1.341} \sum_{n=1}^{\infty} n^{-5/2} \exp \left[-n \frac{T_g}{T} \right] \\ \approx \frac{1}{1.341} \left\{ 2.36 \left[\frac{T_g}{T} \right]^{3/2} + 1.341 - 2.61 \frac{T_g}{T} - 0.730 \left[\frac{T_g}{T} \right]^2 + \dots \right\} . \quad (1.38)$$

The parameter β is related to the spin-wave stiffness constant D by

$$D = \frac{k_B}{4\pi} \left[\frac{2.612 g \mu_B}{\sigma(0) \rho \beta} \right]^{2/3} , \quad (1.39)$$

where ρ is the density.

The parameter γ is related to the mean-square range $\langle r^2 \rangle$ of exchange interaction by

$$\langle r^2 \rangle = 1.948 \left[\frac{16}{k_B} \right] \frac{\gamma D}{\beta} , \quad (1.40)$$

where $\langle r^2 \rangle$ is the mean-square range of the exchange interaction. In Eq.(1.33), the $T^{3/2}$ term comes from the harmonic (k^2) term in the spin-wave dispersion relation and the $T^{5/2}$ term has its origin in the anharmonic (k^4) term. Because of the temperature dependence of D , some additional higher order terms may also

enter, depending on the relationship between D and T . According to the localized models of Dyson [38] and others [39], at low temperatures, magnon-magnon interactions can give rise to a leading $T^{5/2}$ term in D in the long-wavelength limit. On the other hand, itinerant models of Izuyama and Kubo [40] and others [41] predict a $T^{5/2}$ term due to magnon-magnon interaction and a T^2 term due to the interaction between the spin waves and the thermally excited itinerant electrons. Due to the presence of these terms in D , Eq. (1.36) will have a $T^{7/2}$ term and/or a T^4 term in addition to the $T^{5/2}$ term.

D Mössbauer Spectroscopy

Mössbauer effect is the name given to the phenomenon of recoilless emission or absorption of nuclear gamma rays when a particular nuclei are embedded in a solid. It was discovered by the German physicist, R.L. Mössbauer [42] in 1958. Soon after this discovery it was realized that Mössbauer effect provides a simple but precise technique of measuring relative changes in nuclear energy levels which are typically of the order of 1 part in 10^{13} when ^{57}Fe are used as Mössbauer atoms (nuclei). Here the Mössbauer atom refers to the atom whose nucleus is involved in emission or absorption of gamma-ray photons. This high resolution (10^{-13}) allows the observation of hyperfine interactions of the nucleus with its surroundings which, in turn, provides information about the electronic structure of the relevant atom and its environment. These features have rendered Mössbauer spectroscopy an attractive and powerful tool for studying different kinds of problems in diverse disciplines like solid state physics,

chemistry, metallurgy, biology, geology, theory of relativity, etc.

In the present section we shall describe briefly the basic principles of Mössbauer spectroscopy (MS) and hyperfine interactions (HI).

Let us consider a system of mass M (which may be a nucleus or an atom) having two energy levels A and B separated by an energy E_0 as shown in Fig. 1.1(a). Considering the transition of the system from level B to level A by the emission of a photon of energy $E_{ph} = E_\gamma^S$, we can write the recoil energy E_R of the system by applying the law of conservation of momentum as

$$E_R = \frac{P^2}{2M} = \frac{p^2}{2M} = \frac{(E_\gamma^S)^2}{2Mc^2}, \quad (1.41)$$

where p and P are the linear momenta of the photon and the recoiling system respectively and c is the velocity of light. As we know $Mc^2 \gg E_0$, we can write

$$E_R = \frac{E_0^2}{2Mc^2}. \quad (1.42)$$

By the law of conservation of energy

$$E_0 = E_\gamma^S + E_R \quad \text{or} \quad E_\gamma^S = E_0 - E_R. \quad (1.43)$$

Similarly we can consider the excitation of the system from the level A to B and realize that the energy E_γ^a of the incident photon should provide an extra amount of recoil energy

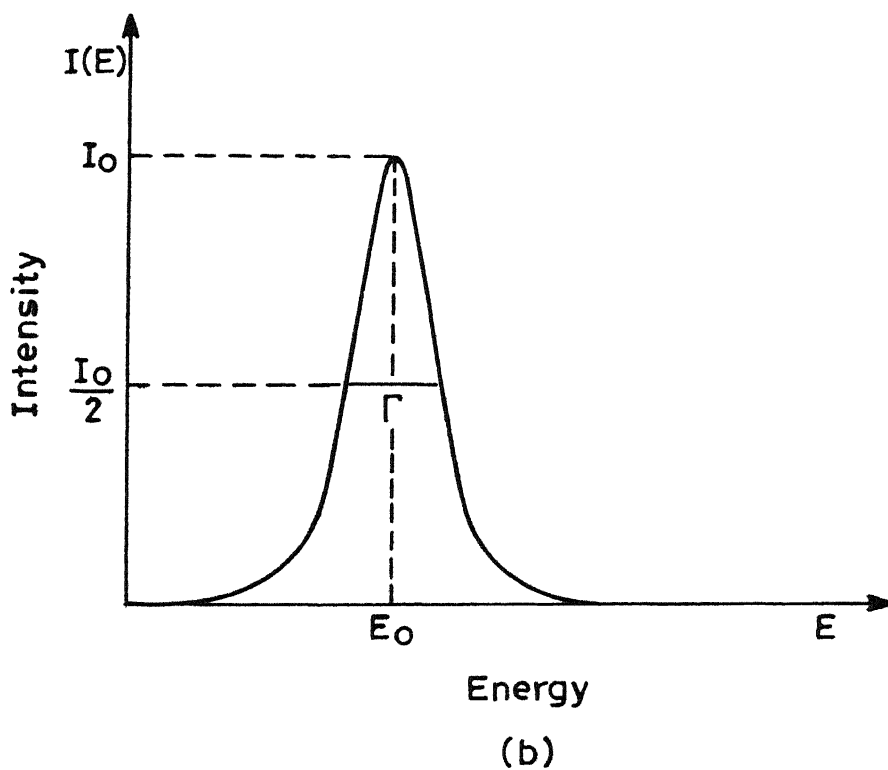
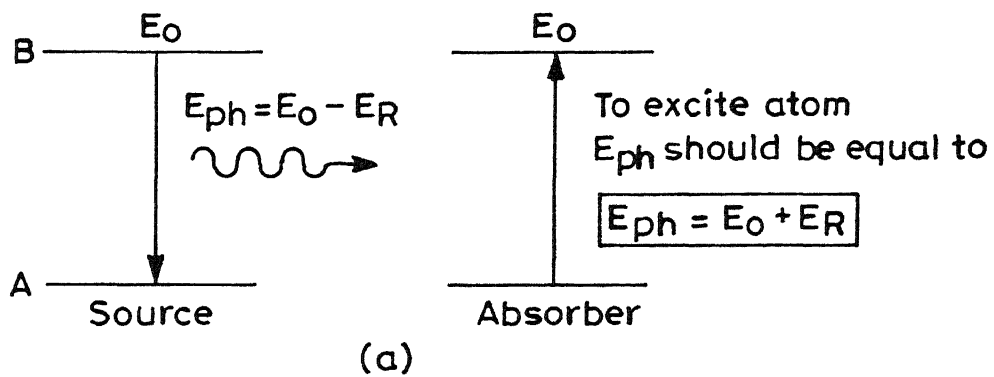


Fig. 1.1 (a) Schematic energy level diagram of free atom or nucleus (b) Intensity $I(E)$ of spectral line as a function of transition energy E .

over and above the transition energy E_0 . We thus have

$$E_\gamma^a = E_0 + E_R \quad . \quad (1.44)$$

Further it is well known that the excited state B does not possess a single energy E_0 but is characterized by a spectral lineshape $\omega(E)$ centered around E_0 [Fig.1.1(b)] given by

$$\omega(E) = \frac{1}{1 + 4 (E-E_0)^2/\Gamma^2} \quad , \quad (1.45)$$

where Γ , the natural line width of the state, is related to the mean life time, τ , through Heisenberg's uncertainty principle

$$\Gamma\tau = h/2\pi \quad , \quad (1.46)$$

where h is the Planck's constant. The energy of the stable ground state is very sharp because it has $\tau \rightarrow \infty$ and $\Gamma \rightarrow 0$. As a result the energy of the photon emitted in the transition from level B to A displays a natural line shape similar to Eq. (1.45) but centered around E_γ^S which is given by Eq. (1.43). Similarly the energy of the photon, which can induce a transition from level A to B, also displays a distribution similar to that of Eq. (1.45) but centered around E_γ^a . An emission of photon will be followed by a resonant absorption when $E_\gamma^a = E_\gamma^S$ and is determined by the overlap of the two distributions

$$\omega_S(E) = \left[1 + \frac{4(E-E_\gamma^S)^2}{\Gamma^2} \right]^{-1}$$

and (1.47)

$$\omega_a(E) = \left[1 + \frac{4(E-E_\gamma^a)^2}{\Gamma^2} \right]^{-1}.$$

The nature of this overlap for the two cases : (a) the atomic system (emission of an optical photon) where $E_R \ll \Gamma$ and (b) the nuclear system (emission of a gamma ray) where $E_R \gg \Gamma$, is shown in Fig. 1.2. It may be noticed that the overlap is very small in the case of the nuclear system.

Mössbauer discovered that in the case of nuclear gamma rays, the overlap of the emission and absorption line shape spectra can be increased by a significant amount if the emitting and absorbing atoms are sufficiently tightly bound inside a solid lattice thus increasing the efficiency of the resonant absorption.

In terms of quantum mechanics, Mössbauer effect can be described by saying that it consists of an enhancement of the probability for observing the zero phonon events (i.e., events in which there is no transfer of energy to or from lattice) over one phonon, two phonon or higher events.

It has been shown that the probability, f , for zero phonon event (f is usually termed as recoil-free fraction) for a Debye solid at $T = 0$ K is given by

$$f = \exp \left[-3E_R/2k_B\theta_D \right], \quad (1.48)$$

where k_B is the Boltzmann's constant and θ_D is the Debye temperature of the solid.

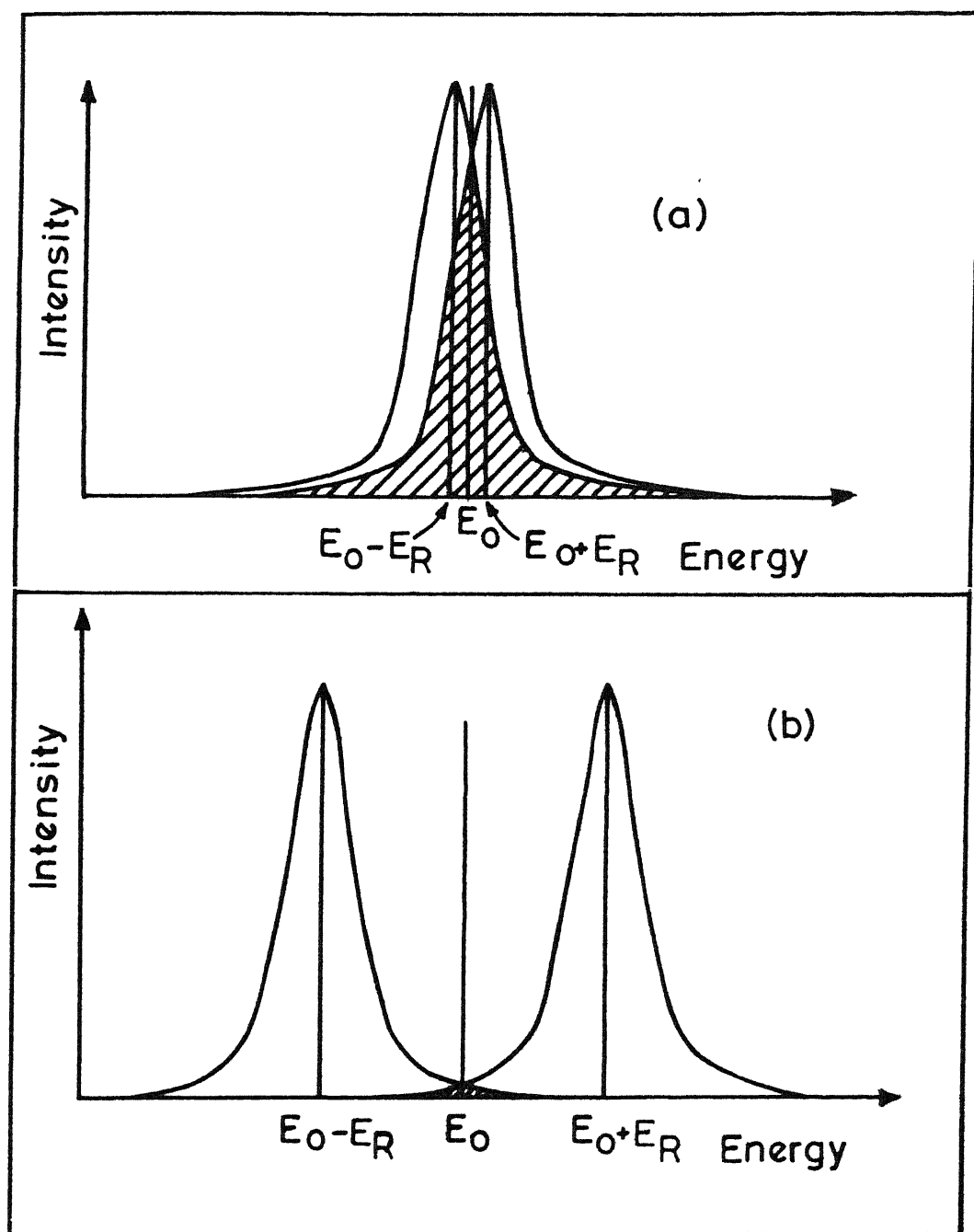


Fig. 1.2 Overlap of the emission and absorption lines showing the relation between E_0 , E_γ^S , and E_γ^a for two cases: (a) optical case $E_R \ll \Gamma$ (b) nuclear case $E_R \gg \Gamma$.

The above discussion makes it clear why the Mössbauer effect can be observed only for a small number of nuclides. For the observation of Mössbauer effect f must be significantly large implying that $E_R \ll k_B \theta_D$. As $E_R \propto E_0^2$ we may think that the solution lies in using very low energy gamma rays. However, very low energy gamma rays will have a poor emission yield and will need very thin absorbers. In most of the practical cases Mössbauer effect is observed in the range $10 \text{ keV} < E_0 < 150 \text{ keV}$, depending on the θ_D value of the element involved.

The nucleus in which the Mössbauer effect is most often observed is ^{57}Fe . Most of the studies in Mössbauer spectroscopy have been carried out in solids containing ^{57}Fe . It is well-known that at room temperature iron exists in the bcc cubic lattice structure and ^{57}Fe nucleus has a ground state with spin $I = 1/2$ and excited state at 14.4 keV with spin $I = 3/2$. The radioactive source ^{57}Co decays to ^{57}Fe with a halflife of about 270 days via electron capture (Fig. 1.3) and can be easily produced through the nuclear reaction $^{56}\text{Fe} (d,n) ^{57}\text{Co}$. As seen in Fig. 1.3, the radioactive decay of ^{57}Co leads to the excited state of ^{57}Fe and the transition from the $(3/2)$ state to the $(1/2)$ state provides the gamma ray for studying the Mössbauer effect in the ^{57}Fe nucleus. In the present study we have used ^{57}Fe as Mössbauer nuclide.

Hyperfine Interactions

The nature of the Mössbauer spectrum and the number and positions of the peaks observed in a Mössbauer spectrum are sensitive to the extranuclear environment and as a result

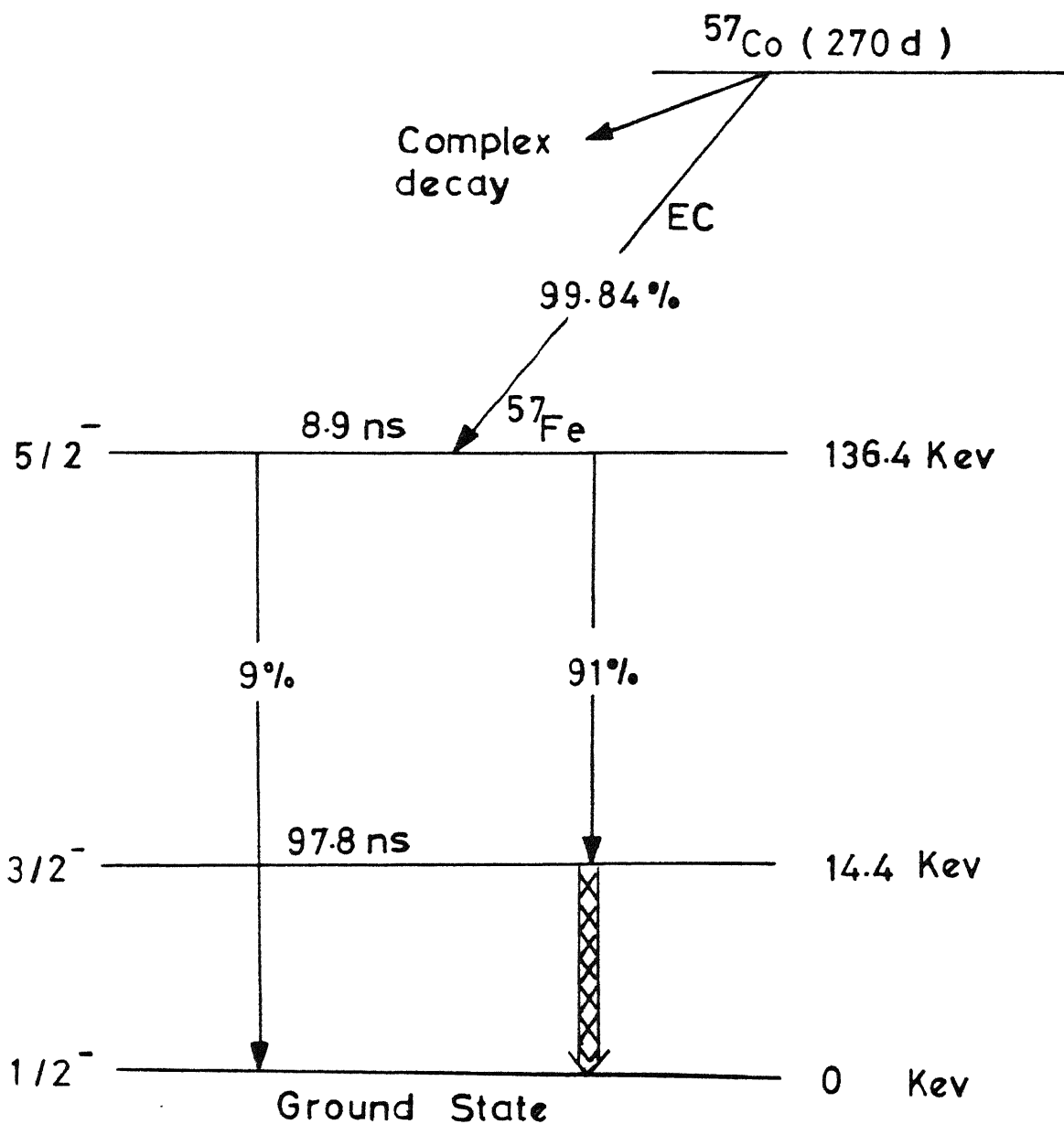


Fig. 1.3 Decay scheme of ^{57}Co to ^{57}Fe .

different spectra are observed from different compounds of ^{57}Fe . To understand these differences in the spectra, one has to understand the effects of the so-called hyperfine interactions. The hyperfine interactions are the result of interaction between nuclear moments and electromagnetic field at the nucleus which is produced by the surrounding electrons and ligands, when a nucleus is bound in a solid. The interaction energy is small (10^{-6} - 10^{-9} eV) and hence the name 'hyperfine interaction'.

These hyperfine interactions can be described in terms of the Hamiltonian

$$H = E_0 + E_2 + M_1 + \dots \quad (1.49)$$

where

$E_0 \rightarrow$ Electric monopole interaction between nucleus and the surrounding electrons [This part gives rise to isomer shift (IS)].

$E_2 \rightarrow$ Electric quadrupole interaction between the nuclear electric quadrupole moment and the electric field gradient of the surrounding electrons [This part gives rise to quadrupole splitting (QS)].

$M_1 \rightarrow$ Magnetic dipole interaction between the nuclear magnetic moment and the surrounding extranuclear magnetic field [This part gives rise to nuclear Zeeman effect].

Electric Monopole Interaction

The electric monopole interaction affects the position (or the centroid) of the resonance line on the energy (or

velocity) scale thus giving rise to the so-called isomer shift (IS). The electric monopole interaction results from the electrostatic interaction between the charge distribution of the finite-sized nucleus and those atomic electrons which have a finite probability of being found in the nuclear region. As a result of this interaction, the nuclear energy levels do not show any splitting but there is a small but measurable shift of the Mössbauer energy levels in a compound compared to that in a free atom. This effect is illustrated in Fig. 1.4(a), where this shift is shown to be different in source and absorber. The energy of the Mössbauer gamma ray in the source is denoted by E_γ^S while that in absorber is E_γ^A and the difference between E_γ^S and E_γ^A is typically of the order of 10^{-9} eV. In order to observe resonance, one will have to provide a Doppler velocity v to the source (or absorber) so that $[E_\gamma^S \pm \frac{v}{c} E_\gamma^S] = E_\gamma^A$.

In the absence of electric quadrupole or magnetic dipole interaction, isomer shift manifests itself as the shift of the single resonance from the zero velocity [Fig.1.4(b)]. If the electric quadrupole or magnetic dipole interactions are also present, the isomer shift is determined from the centre of gravity of the Mössbauer spectrum and it gives a measure of the strength of the electric monopole interaction.

The isomer shift can be computed classically by considering the effect of the overlap of s -electron density with the nuclear charge density [43]. The nucleus is assumed to be an uniformly charged sphere of radius R . The s -electron density at the nucleus is denoted by $[\psi(0)_s]^2$ and assumed to be constant over the nuclear volume. Let δE denote the energy difference between

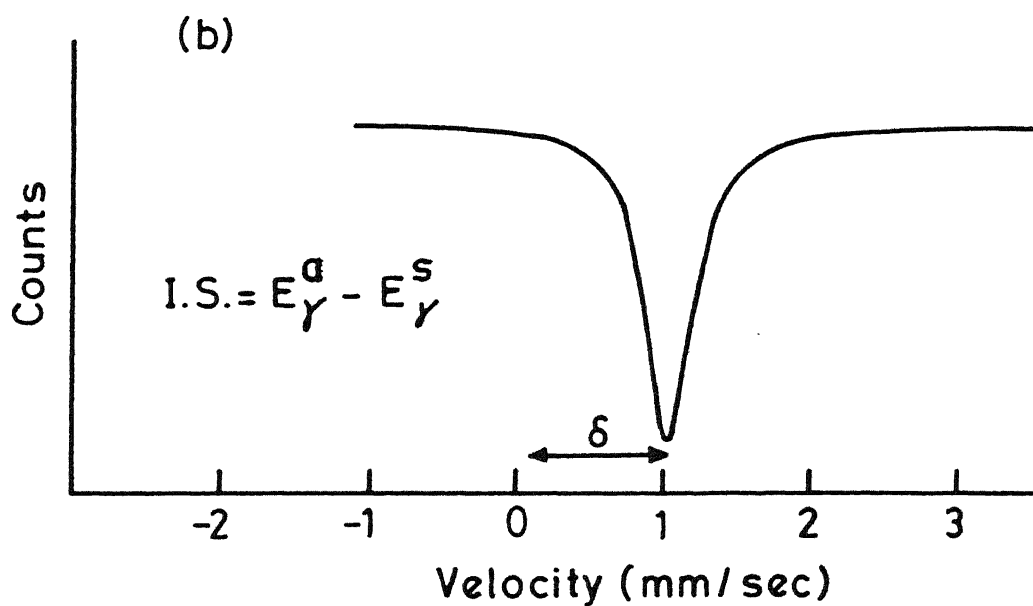
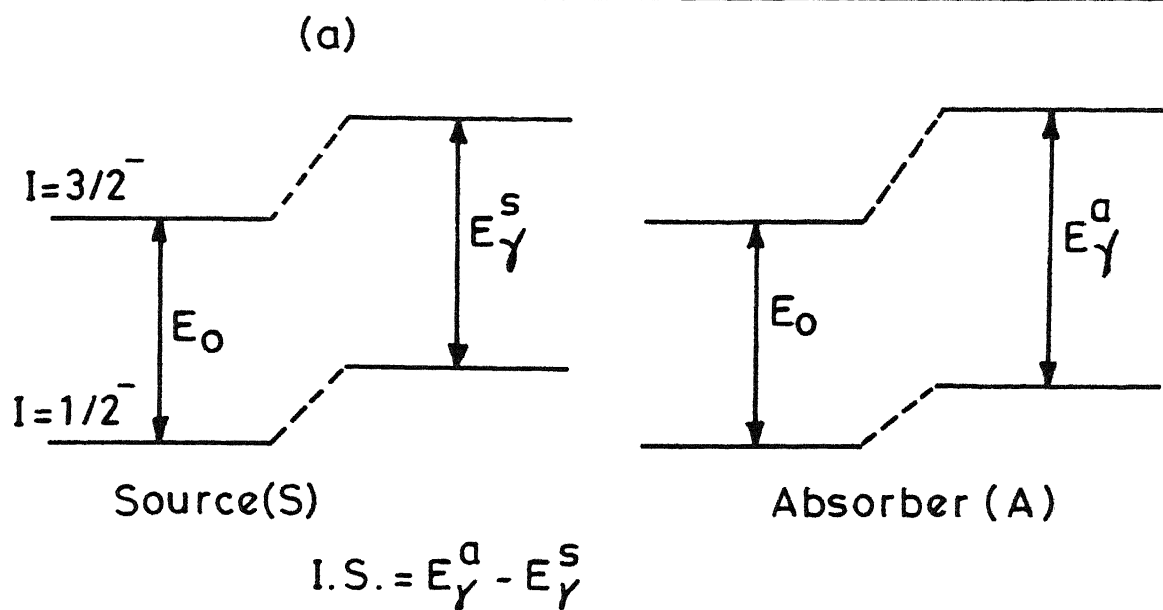


Fig. 1.4 (a) Effect of monopole interaction on the energy levels of source and absorber (b) Mössbauer spectrum showing monopole interaction.

the electrostatic interaction of a point nucleus with $[\psi(0)_s]^2$ and the interaction of a finite-sized nucleus having radius R with $[\psi(0)_s]^2$. It can be written as

$$\delta E = k [\psi(0)_s]^2 R^2, \quad (1.50)$$

where k is a nuclear constant. As R is generally different for ground and excited nuclear states, δE will be different for both. Using the subscripts e and g for the excited and ground nuclear states respectively, we have

$$\delta E_e - \delta E_g = K [\psi(0)_s]^2 (R_e^2 - R_g^2). \quad (1.51)$$

For a given nucleus (e.g., ^{57}Fe), the R -values will be constant but the values of $[\psi(0)_s]^2$ will vary from one compound of iron to another. In Mössbauer experiments the above energy difference becomes measurable by comparing the nuclear transition energy in a source (E_γ^s) with that in an absorber (E_γ^a). The isomer shift is the Doppler velocity which is provided to the source to observe the resonance and is given by the difference of Eq. (1.51) for the source and the absorber, i.e.,

$$\text{IS} = K(R_e^2 - R_g^2) \left[[\psi(0)_s]_a^2 - [\psi(0)_s]_s^2 \right], \quad (1.52)$$

where the subscripts a and s refer to the absorber and source respectively. In usual practice, one uses a standard source material (e.g., ^{57}Co in Rh) for ^{57}Fe Mössbauer spectra. As the change in radius $\delta R = (R_e - R_g)$ is very small, the isomer shift can

then be written as

$$IS = 2KR^2 \frac{\delta R}{R} \left[[\psi(0)_s]_a^2 - C \right] , \quad (1.53)$$

where C is a constant characteristic of the source used. Thus the isomer shift depends on a nuclear factor δR and an extranuclear factor $[\psi(0)_s]^2$. For a given nucleus ^{57}Fe , δR is a constant and so the isomer shift is directly proportional to the s -electron density at the nucleus. In the case of ^{57}Fe , δR is negative and thus the isomer shift becomes more negative with an increase in the s -electron density at the absorber nucleus (^{57}Fe). In addition, changes in p - or d -electron density also induce changes in IS value even though the p - or d -electrons do not directly interact with the nuclear charge density.

Magnetic Dipole Interaction

A nucleus having a spin I has a magnetic dipole moment μ_N , given by the equation

$$\mu_N = g_N \beta_N I , \quad (1.54)$$

where g_N is the nuclear Landé splitting g factor and $\beta = \frac{eh}{2M} =$ nuclear magneton.

The effective magnetic field, H_{eff} , at the Mössbauer nucleus is

$$H_{\text{eff}} = H_{\text{ext}} + H_{\text{int}} , \quad (1.55)$$

where H_{ext} is the externally applied magnetic field and H_{int} is the internal magnetic field having contributions from three terms as given below

$$H_{\text{int}} = H_c + H_L + H_d, \quad (1.56)$$

where H_c is the Fermi contact field which arises from a net s -electron spin density at the nucleus as a consequence of spin polarization of inner filled s -shell by spin-polarized partially filled outer shells; H_L is the contribution from the orbital motion of valence and partially filled inner shell electrons and H_d is the spin dipolar term arising from the spin of the electrons outside the Mössbauer atom.

Magnetic Splitting

The magnetic dipole moment μ can interact with an effective magnetic field (H_{eff}) at the nucleus. The Hamiltonian M_1 for this interaction (which is also called magnetic dipole interaction or nuclear Zeeman effect) is given by

$$M_1 = -\mu H_{\text{eff}} = -g_N \beta_N I H_{\text{eff}}. \quad (1.57)$$

The energy eigenvalues of M_1 corresponding to the eigenvector $|I m_I\rangle$ is given by

$$E_M(m_I) = -\frac{\mu H m_I}{I} = g_N \beta_N m_I. \quad (1.58)$$

It is obvious from Eq. (1.58) that this interaction

causes a nuclear state $|I m_I\rangle$ to split into $(2I + 1)$ substates $(|I m_I\rangle, |I m_I - 1\rangle, \dots, |I - m_I\rangle)$.

Let us consider the case of ^{57}Fe in which there is a transition between the states $|I = \frac{3}{2} m_I\rangle$ and $|I = \frac{1}{2} m_I\rangle$. The state $I = 3/2$ will be split into four substates with an energy splitting of $\mu_e H m_{I_e} / I_e$ with respect to the energy of the unperturbed (or unsplit) state. Similarly, the state $I = 1/2$ will be split into two substates with an energy splitting of $(\mu_g H m_{I_g} / I_g)$. In the above discussion the suffixes e and g refer to the excited state $I = 3/2$ and the ground state $I = 1/2$ respectively. This is shown in Fig. 1.5. Taking into account the selection rule $\Delta m_I = 0, \pm 1$, the transitions from $I_e = 3/2$ to $I_g = 1/2$ give rise to six symmetric lines with respect to the centroid. The centroid in the spectrum is the position of the spectral line if the $I_e = 3/2$ and $I_g = 1/2$ states were not split.

By measuring the positions of the resonance lines in the Mössbauer spectra, $H_{\text{eff}} = H$ at ^{57}Fe can be found out as $H = 0.843 \times 10^5 [L_5 - L_3] \times \text{calibration (mms}^{-1} \text{ channel}^{-1}) \text{ Oe}$, where L_3 and L_5 are the positions of the third and fifth lines, respectively.

The study of the effective magnetic field at the nuclear sites has been very useful in understanding the magnetic properties of solids on atomic scale. We shall use such an analysis to characterize the nature of the magnetic phases precipitated in the metallic glasses studied by us.

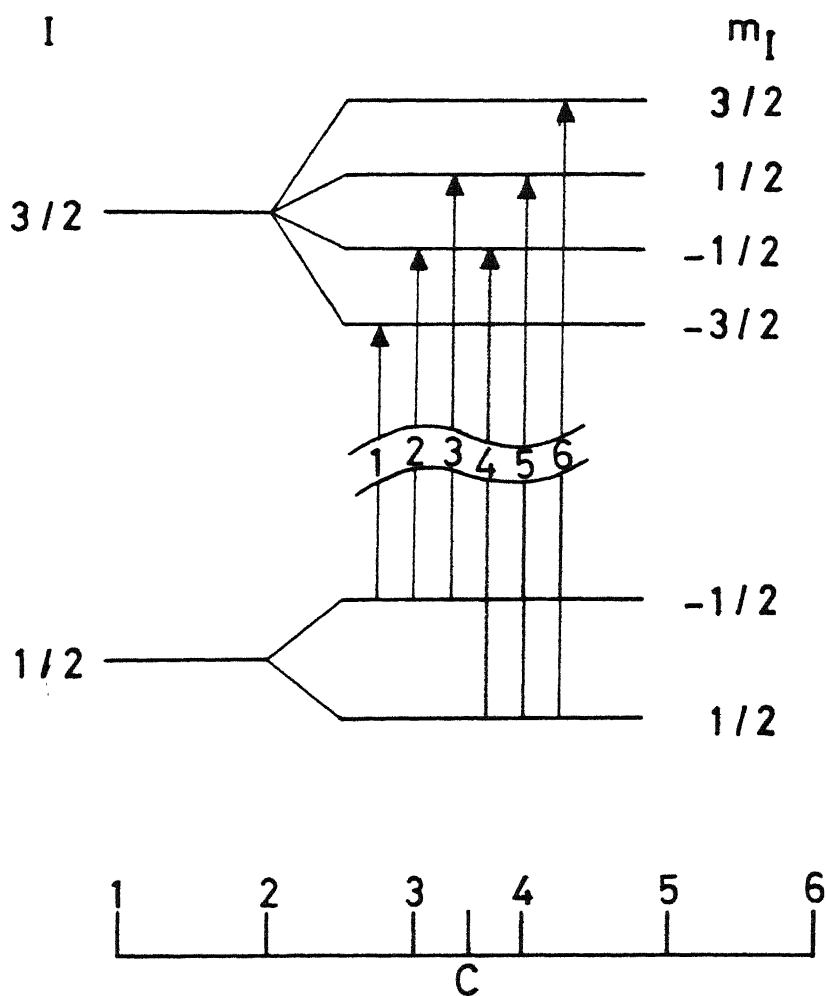


Fig. 1.5 Effect of magnetic hyperfine interaction on energy levels of ^{57}Fe . Peak positions of the six-finger pattern are shown at the bottom (C =Centroid).

CHAPTER II

EXPERIMENTAL

2.1 Electrical Resistivity and Magnetoresistance

Amorphous $\text{Fe}_{80}\text{B}_{20-x}\text{Si}_x$ ($x = 0, 1, 2, 4, 6, 8, \text{ and } 12$) alloy ribbons were obtained from F.E. Luborsky of the General Electric Company, U.S.A. These amorphous ribbons were prepared by melt-quenching onto the surface of a rotating wheel. Their amorphous nature was checked by X-ray diffraction.

The schematic diagram of electrical resistivity set-up is shown in Fig. 2.1. dc-electrical resistivity measurements were made between 8 and 300 K using a four-probe method. Temperatures down to 8 K were achieved by using a closed-cycle helium refrigerator (CTI and Cryosystems). In these refrigerator systems compressed helium gas is made to expand in a chamber with a piston and an assembly of regenerators. The temperature, lowered as a result of the expansion of helium gas in this chamber, is carried by a oxygen-free-high-conductivity (OFHC) copper disc. The helium gas after expansion is returned to the compressor by the motion of the piston and the valves. The movement of the piston is controlled electrically and synchronized properly. Thus the low temperature is available on a plate of diameter of about 1 inch, and the sample, placed on this, is cooled by conduction. This requires a proper thermal contact between the plate and the sample but a good electrical insulation between the two is also necessary for electrical measurements. To achieve the twin requirements simultaneously cigarette paper was pasted on the copper disc with GE varnish and then the sample of typical length

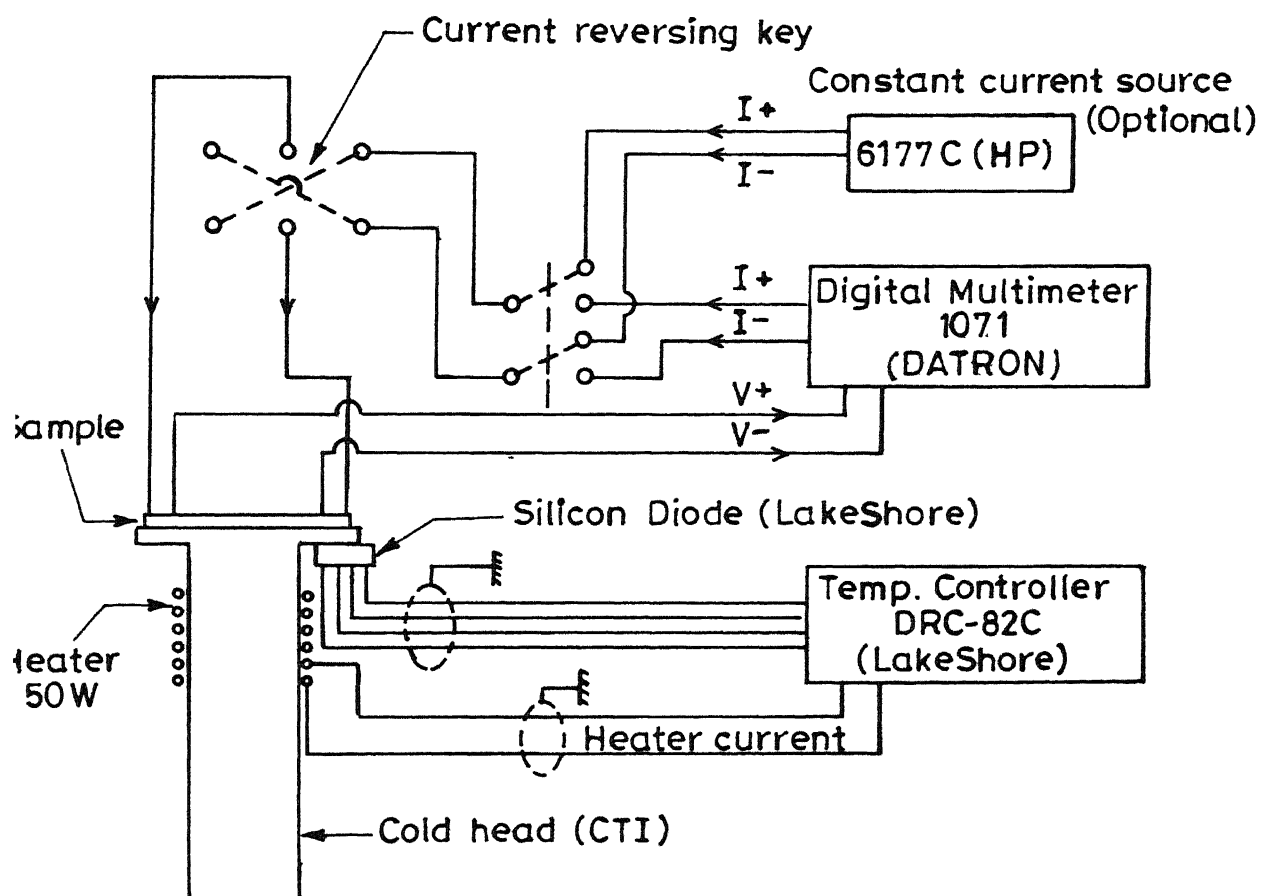


Fig. 2.1 Schematic diagram of electrical resistivity set-up.

of about 2-3 cm was pasted on it again with GE varnish. This varnish gives a good thermal contact of the sample with the disc. The nonmagnetic copper-phosphorous alloy electrical leads were soldered to the sample using low-melting point nonsuperconducting solder (eutectic CdZn) with a low wattage soldering iron to prevent partial crystallization of the sample.

In measuring the resistance in zero magnetic field a Datron 1071 Autocal digital multimeter (DMM) was directly used. The measuring current in this case was 10 mA and was provided by the DMM itself. A pre-calibrated Si diode (DT-470, Lake Shore) was attached to the copper disc by indium foils for good thermal contact. The temperature was monitored and controlled by a temperature controller (DRC-82C, Lake Shore). This silicon diode senses the temperature of the copper disc and hence of the sample. The heater is wound non-inductively just below the copper disc. A proper choice of PID (proportional-integral-derivative) values of the temperature controller ensured a temperature stability within ± 0.1 K. Without using any heater power, the temperature obtained by the cold-head is 8 K. For taking data, first one sets the temperature. Once the temperature is reached within ± 0.1 K, the resistance R_+ of the sample at that particular temperature is taken. After the current direction is reversed, R_- is noted. The average of these two values of R is the actual resistance of the sample at that particular temperature. The current direction is reversed to minimize thermo e.m.f. effects. The accuracy of $\Delta R/R$ was better than 1 part in 10^5 .

For samples $x = 0, 6$, and 12 magnetoresistance was measured in both orientations (current density $\vec{J} \parallel \vec{M}$ and $\vec{J} \perp \vec{M}$

where \vec{M} is the magnetization) at several constant temperatures. In measuring magnetoresistance an external constant current source (6177 C, Hewlett Packard) was used to provide a current of 100 mA. The voltage developed across the sample was measured with the Datron DMM. The magnetic field up to 16.5 kOe was provided by a 15 inch Varian V-3800 electromagnet. The external magnetic field, in both the orientations was always in the plane of the ribbon to ensure low demagnetization factors. The temperature was sensed by a pre-calibrated carbon-glass resistance thermometer (CGR-1-1000, Lake Shore) which had very low magnetoresistance (-0.2% at 10K and 2.5 Tesla) even at the lowest temperature. The temperature was monitored and controlled by a temperature controller (DRC-93C, Lake Shore). In these measurements the accuracy of $\Delta R/R$ was about 1 part in 10^6 . Resistance measurements were also taken at about 110 temperatures between 10 and 300 K at constant magnetic fields of 2, 7, and 14 kOe.

2.2 High- and Low-Temperature Magnetization

These magnetic measurements were done by using a vibrating sample magnetometer (155, PAR). The magnetometer was calibrated with the help of a standard Ni sample after the usual saddle-point adjustments. Several pieces of the metallic glass samples of length 2-3 mm each were loaded in the sample holder with the magnetic field in the plane of the ribbon. The output from the magnetometer was directly recorded on an X-Y recorder. A high-temperature oven assembly (151, PAR), in conjunction with the VSM, enabled us to make measurements above 300 K. These measurements were done in the residual field (30 Oe) of a 9-inch

Varian V-7200 electromagnet. The sample was heated in the temperature range of 300 to 990 K. A chromel-alumel thermocouple was used to measure the temperature with an accuracy of ≈ 1 K. The typical heating-rate used in the experiment was 5 K/min, but near the transition temperature, the rate was lowered to 2 K/min. X-ray diffraction at room temperature was taken on the crystallized samples, obtained after thermomagnetic study, using Rich and Seifert Isodebyeflex 2002 diffractometer with a CrK_{α} source.

For low-temperature measurements below 300 K a closed-cycle helium refrigerator (CTI and Cryosystems) was used. The minimum temperature that could be reached was 19 K. The temperature was measured with a 100 Ω platinum resistance thermometer (Pt-100, Lake Shore). dc-magnetic fields up to 16.5 kOe were obtained from a 15-inch Varian V-3800 electromagnet.

2.3 Mössbauer Spectrometer

The Mössbauer spectrometer, shown schematically in Fig. 2.2, consists of the following units :

- (i) Radioactive source which emits gamma-ray photons appropriate for observing Mössbauer effect.
- (ii) Mössbauer drive which can provide measurable relative velocities between the source and the absorber, usually with a constant acceleration.
- (iii) Sample to be studied (containing ^{57}Fe nuclei) as an absorber.
- (iv) Gamma ray detection and amplification system.
- (v) Multichannel analyzer (MCA) for data storage and

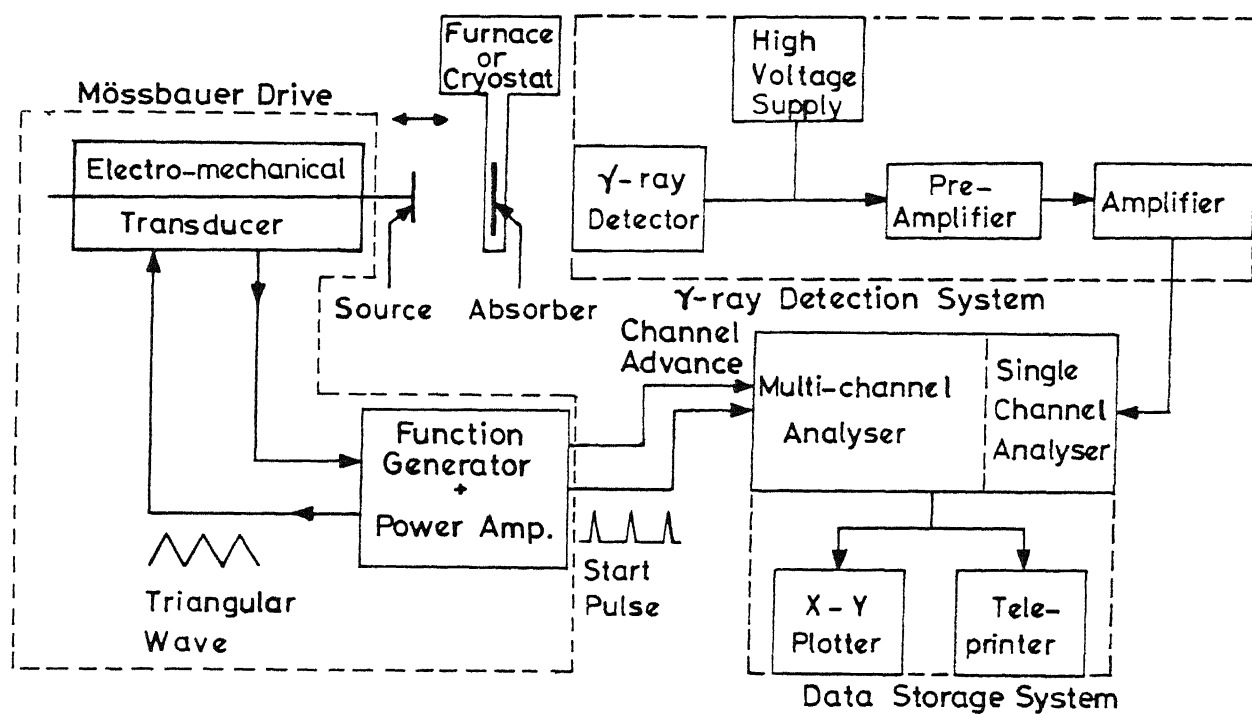


Fig. 2.2 Schematic block diagram of Mössbauer spectrometer.

analysis.

A good Mössbauer spectrometer is built with an appropriate and optimum combination of the above parts. In the following section we shall briefly discuss the details of the above units used in the present work.

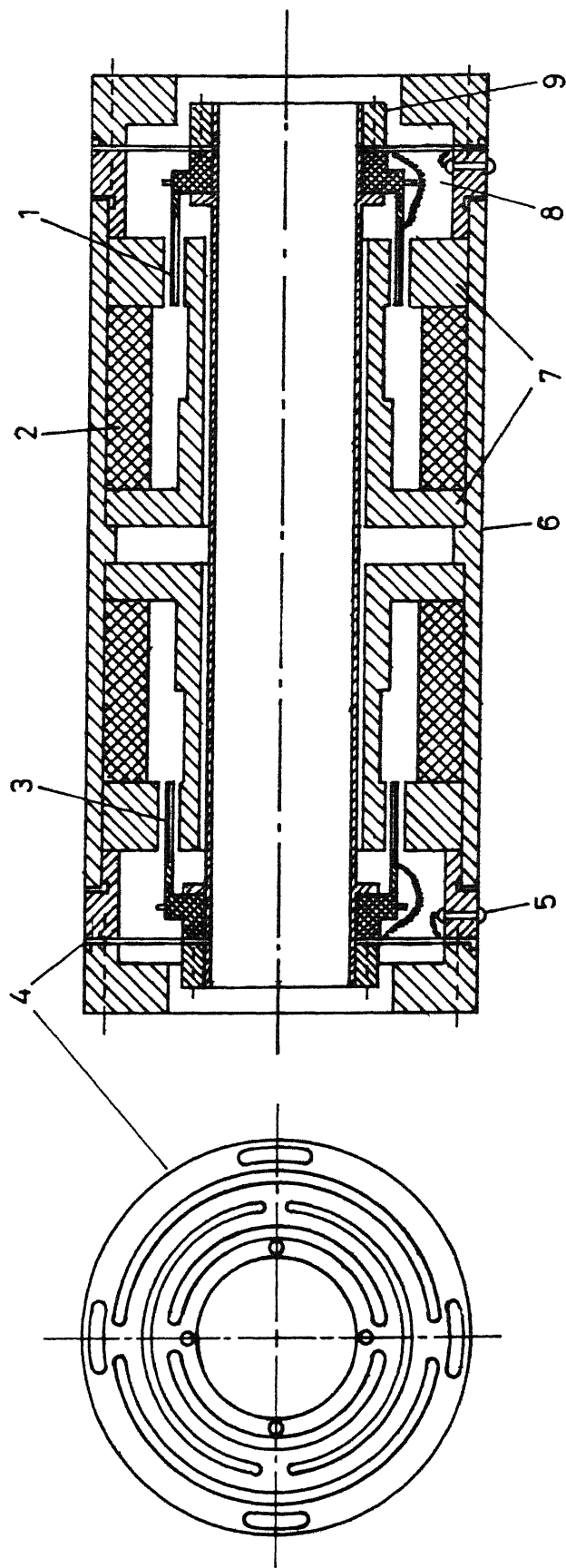
i) Gamma-ray photon source

In our experiments we used a radioactive source of ^{57}Co diffused in Rh matrix. It had an initial activity of 25.5 mCi and had a recoil-free fraction equal to 0.76. This source provided 14.4 keV gamma rays in ^{57}Fe which were appropriate for Mössbauer spectroscopy and it was supplied by New England Nuclear Inc., U.S.A.

ii) Mössbauer drive

The Mössbauer spectrometer, used in the present work was based on the system supplied by WISSEL (Wissenschaftliche Elektronik GmbH), West Germany. It consists of a velocity transducer (model MA-260), a function generator (model DFG-1200) and a driving unit (power amplifier, model MR-360).

The velocity transducer is based on the principle of two mechanically coupled loudspeakers [44,45] and it consists of a pair of rigidly connected coils (driving and pick-up coils) wound on the sample holder. The schematic diagram of the velocity transducer is shown in Fig. 2.3. A permanent magnet produces a homogeneous magnetic field in the air gap of the coil system and this field is constant (within few parts in 10^4) along the axis of motion. The constant magnetic field ensures high linearity of the



- 1-Pickup coil, 2-Permanent magnet, 3-Drive coil, 4-Guide spring,
 5-Electrical feed through, 6-Connecting tube, 7-Magnet yokes, 8-Coil shell,
 9-Flange for mounting source.

Fig. 2.3 Schematic diagram of electromechanical velocity transducer.

driving system. The magnetic induction is approximately 0.25 Tesla. The function generator produces a reference signal which is fed to the power amplifier. The output of the power amplifier, which is proportional to the ideal velocity of the transducer, is fed to the driving coil. The actual velocity is sensed by the pick-up coil in the form of a pick-up signal. The difference between the reference signal and the pick-up signal is known as the difference (or error) signal. This difference signal is proportional to the deviation of the actual velocity from its stipulated value. The difference signal is then amplified and fed back to the driving coil through a feed-back loop amplifier to minimize the deviation from the ideal velocity.

iii) Absorbers

In our measurements we used (i) natural iron (α -Fe, enriched in ^{57}Fe) and (ii) 310 stainless steel (310 SS) as standard absorbers to calibrate the Mössbauer spectrometer. These standard absorbers were obtained from Amersham International Limited, Amersham, U.K.

The sample absorbers were prepared from the ribbons of $\text{Fe}_{80}\text{B}_{20-x}\text{Si}_x$ ($x = 0, 2$ and 8) placed parallel and close to each other by pasting them over copper rings with inner diameter of 1 cm.

iv) Gamma-ray photon detection system

The gamma-ray spectrometer, used in the present work, consists of the following :

- a) Proportional counter : model I 1331, ECIL.

- b) Preamplifier : model 2006, Canberra, U.S.A.
- c) High voltage power supply : model 456, EG & G ORTEC, U.S.A
- d) Spectroscopy amplifier : model 2021, Canberra, U.S.A.

The gas-filled proportional counter, used in the present work, contained krypton and has an aluminised mylar window. It is well-known that the proportional counter receives the gamma-ray photons and converts them into linear charge (or electrical) pulses. These linear charge pulses are received by the preamplifier which gives as output a set of linear tail voltage pulses. The amplitude (or the height) of these linear tail pulses is directly proportional to the energy of gamma-ray photons received by the proportional counter. A high-voltage power supply, capable of supplying +1500 to +3000 volts at 0.1 to 1.0 mA, is used to operate the proportional counter. The output pulses from the preamplifier are further fed into a linear amplifier which delivers analog output pulses in the range 0-10 volts. The analog pulses carry the energy information about the gamma-ray photons which are received by the proportional counter [46,47]. Before recording the Mössbauer spectrum in the transmission mode it is necessary to fix the energy window of the gamma-ray spectrum to ensure that the appropriate 'Mössbauer' radiation is selected. In the case of ^{57}Co - ^{57}Fe Mössbauer spectroscopy (which was used in the present work), the appropriate Mössbauer radiation is the 14.4 keV gamma ray. This was achieved by using a single channel analyzer (SCA) or by using a multichannel analyzer in the pulse height analysis (PHA) mode.

v) Multichannel analyzer

In the present work we used the multichannel analyzer (MCA) (model no. ND-65) supplied by Nuclear Data Inc., U.S.A. It was used in the pulse height analysis (PHA) mode for fixing the energy window and in the multichannel scaling (MCS) mode for recording the Mössbauer spectrum. Data acquired in the MCA was printed out using a Teletype printer which was interfaced with the MCA.

Experimental Procedure

The velocity transducer, source absorber, and proportional counter were mounted and aligned carefully on a vibration-free optical bench. By adjusting the distance between the source and the detector, a well-resolved three-peak pulse height spectrum was obtained (Fig. 2.4). The intensity of the low-energy X-rays (6.2 keV) was reduced off by inserting a thin aluminium foil between the source and the absorber. Next, the lower level discriminator (LLD) and upper level discriminator (ULD) controls of the MCA were adjusted to store those pulses whose height corresponded to the full photopeak of the 14.4 keV gamma ray in the pulse height spectrum of the ^{57}Co source.

In the transmission Mössbauer spectroscopy, as used in the present work, the transmission rate of gamma rays through a resonant absorber was measured as a function of the relative velocity between the source and the absorber. The relative velocity between the source and the absorber was swept rapidly through the range of interest, $-V_{\text{max}} \leq 0 \leq +V_{\text{max}}$, in both the directions with the help of a function generator which provided

symmetric saw-tooth voltage waveform (or the reference signal) to the velocity transducer. The gamma rays transmitted through the absorber were detected by a gamma-ray detection system and were stored in 512 channels of the MCA in the MCS mode. Synchronization of the channel number in the MCA with the velocity increment ΔV , between V and $V + \Delta V$, was achieved by advancing the address of the memory, one by one, through an external clock (i.e., channel advance pulses which were produced by the function generator) and it divided the period of reference signal into 512 pulses. A 'start' pulse, which coincided with the beginning of the reference signal, enabled the MCA to start with channel number 1 being advanced by the clock pulse.

The calibration of the present Mössbauer spectrometer was done by using the standard α -Fe absorber whose Mössbauer parameters are well-known. The peak positions of the Mössbauer spectral lines of α -Fe are known to be situated at -5.328, -3.083, -0.838, +0.838, +3.083, and +5.328 mms^{-1} , respectively. A typical Mössbauer spectrum of α -Fe showed

- a) Centroid position at 127.8 channels,
- b) Velocity per channel = 0.097 mms^{-1} , and
- c) Line-width (full-width at half-maximum) = 0.28 mms^{-1} .

Geometrical Effects

The performance of the Mössbauer spectrometer is affected considerably by the geometry of the source-absorber-detector system. We outline below the two major types of such geometrical effects which give rise to distortions in the Mössbauer spectrum.

i) Source-detector distance variation effect

In a transmission Mössbauer experiment the source is usually made to move back and forth about its mean position and the absorber is kept at rest. As a result, the distance between the source and the detector changes periodically during one cycle of motion. The number of gamma-ray photons, received by the detector per second, is directly proportional to the solid angle subtended by the source at the detector window and this number changes continuously and periodically as the source moves towards and away from the detector. This results in a non-flat behaviour of the baseline of the Mössbauer spectrum.

This type of geometrical effect can be eliminated by folding the two Mössbauer spectra in the MCA (these two Mössbauer spectra, the so-called right and left spectra, are the consequences of the symmetric nature of the saw-tooth waveform of the signal fed to the Mössbauer drive).

ii) Cosine effect

The cosine effect is caused by the finite size of the source, absorber and of the detector window and it results in the broadening of absorption peaks with a slight shift in peak positions. The gamma-ray photons reaching the detector fall at different angles with respect to the direction of relative motion. The energy of the gamma-ray photons which enter the detector is given by

$$E(\theta) = E_0 \left[1 - \frac{v}{c} \cos \theta \right],$$

where θ is the angle between the propagation direction of the gamma-ray photon and the direction of the relative motion. The

possible values of θ for a particular geometry varies between 0 and θ_{\max} and hence it is not possible to consider a single effective velocity. If θ is large (i.e., source-detector distance is small), this effect will be pronounced resulting in a broad and distorted spectrum. If source-detector separation is large, the cosine effect will decrease. However, at large source-detector separations, the counting rate will become lower thus requiring longer time for recording spectrum. In our measurements, this effect was minimized by optimizing the distance between the source and the absorber.

Data Analysis

Mössbauer data are usually analyzed with the help of a computer program which assumes the peaks to be Lorentzian. This approximation is reasonably good when the source and the absorber have low effective layer thickness.

A number of computer programs are available for carrying out the analysis of Mössbauer data. The basic concept is almost the same in all the programs. In our analysis we have used a program based on the method developed by Law and Bailey [48]. This program finds the value of adjustable parameters (i.e., guess values) to get closest agreement between the experimental data and the value predicted by the assumed function.

Let the function $\phi = \phi_i(B_1, B_2, \dots, B_n)$ be the functional form chosen to fit the experimental points Y_i . The condition for getting the set of parameters is that

$$S^2 = \sum_{i=1}^N S_i^2 = \sum_{i=1}^N (Y_i - \phi_i)^2$$

is a minimum, where N is the number of experimental data points.

CHAPTER III

RESULT AND DISCUSSION

3.1 Electrical Resistivity*

The temperature dependence of the normalized resistivity $r(T) = \rho(T)/\rho(0^\circ\text{C})$ in the temperature range 8 - 300 K for the amorphous $\text{Fe}_{80}\text{B}_{20-x}\text{Si}_x$ ($x = 0, 1, 2, 4, 6, 8$, and 12) series is shown in Figs. 3.1 and 3.2. In this temperature range these glasses are ferromagnetic with T_C more or less constant between 645 and 680 K. The values of ρ at different temperatures have been normalized to their respective resistivity value at 273 K because there is a large error ($\sim 10\%$) in the measurements of the ribbon thickness and width, resulting in a large inaccuracy in the absolute values of ρ . The latter has been calculated by measuring the sample resistance at room temperature. The room-temperature value of ρ is $(127 \pm 10) \mu\Omega\text{cm}$ for the whole series. The ρ versus x plot does not show any specific trend within the experimental accuracy. Figures 3.1 and 3.2 show that ρ changes by 3-4% from 8 to 300 K. Minima in ρ are observed at temperatures (T_{\min}) below 20 K. Typically, T_{\min} varies from 11 to 16 K. Such minima at low temperatures are observed in various ferromagnetic and nonferromagnetic amorphous glasses. This feature is known to arise as a result of structural disorder, electron localization etc. [49]. Since the temperature range below T_{\min} is hardly available to us, we could not investigate this further.

We analyze the region above T_{\min} on the lines of the

*The work reported under sections 3.1 and 3.2 has been accepted
J. Appl. Phys. 64 (August 1991)

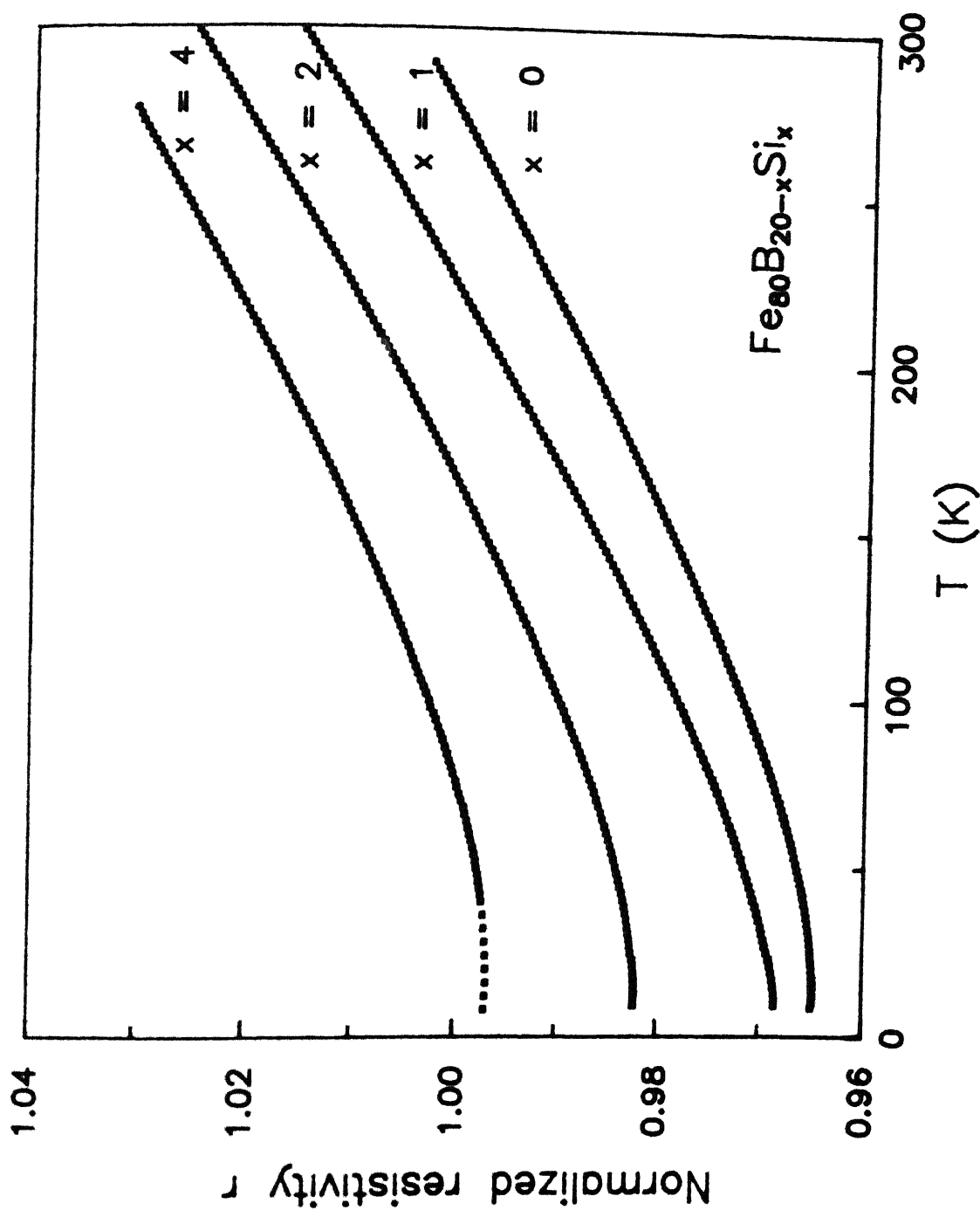


Fig. 3.1 Temperature dependence of the normalized resistivity r for amorphous $\text{Fe}_{80}\text{B}_{20-x}\text{Si}_x$ ($x = 0, 1, 2$, and 4) alloys. Each curve is displaced along the r axis by 0.01 with respect to the one below it.

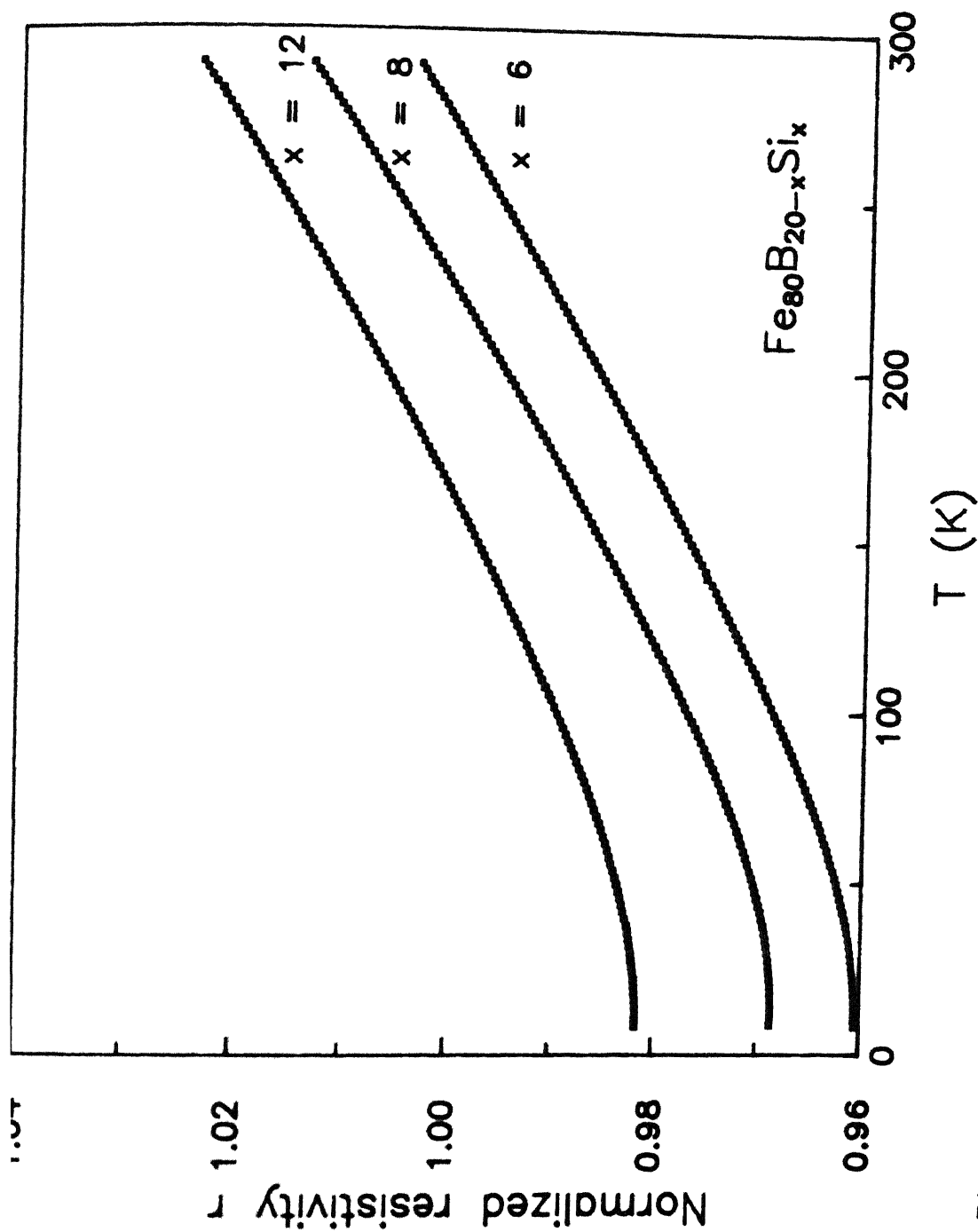


Fig. 3.2 Temperature dependence of the normalized resistivity r for amorphous $\text{Fe}_{80}\text{B}_{20-x}\text{Si}_x$ ($x = 6, 8$, and 12) alloys. Each curve is displaced along r the axis by 0.01 with respect to the one below it.

predictions of the model by Richter et al. [4] for amorphous ferromagnets. These samples are ideal for verifying the predictions of this model as they remain ferromagnetic in the whole temperature range used for analysis. We have taken data points every 1 K apart at low temperatures and every 2 K at higher temperatures. The dispersion in the data is rather small and the number of data point are sufficiently large for us to draw meaningful conclusions from their fits to Eqs. (1.7)-(1.9). A least-squares-fit program in Pascal on an IBM PC microcomputer was used. Table 3.1 shows the fits of the data between 35 and 85 K to Eqs. (1.7) for all the samples with two terms [Eq.(1.7a)] and three terms [Eq.(1.7b)]. In Eq. (1.7a) only two terms are considered, the temperature independent part (ρ_0) and the T^2 term. The latter comprises of contributions from both the structural and the magnetic term since the functional dependence of both these are the same and thus makes them indistinguishable from each other. If the magnetic term is considered to be of the form $T^{3/2}$, then we have this term as well in addition to the ρ_0 and T^2 terms of Eq. (1.7b). One should note that $r(T)$ in Eqs. (1.7) to (1.9) is of the order of 1, thus a χ^2 of the order of 10^{-10} represents a very good fit since the accuracy of $R(T)$ itself is only a few parts in 10^6 . Here we have defined χ^2 as

$$\chi^2 = \sum_{i=1}^N \left[r(T)_i(\text{measured}) - r(T)_i(\text{fitted}) \right]^2 / N,$$

where N is the number of data points. It is obvious from the values of χ^2 that the inclusion of the $T^{3/2}$ term invariably improves the fit very significantly and, in some cases, even by

Table 3.1

Composition, coefficients for fits to Eq. (1.7) and resulting χ^2 , coefficients for fits to Eqs.(1.8) and (1.9b) and resulting χ^2 and values of θ_D obtained from Eqs.(1.10)-(1.12) in $\text{Fe}_{80}\text{B}_{20-x}\text{Si}_x$ ($0 \leq x \leq 12$) amorphous ferromagnets.

x (at. %)	Range of fit : 35-85 K			Range of fit : 200-300 K			χ^2 (10^{-10})	θ_D (K)
	$10^7 \alpha_2$ (K^{-2})	$10^6 \alpha_{3/2}$ ($\text{K}^{-3/2}$)	χ^2 (10^{-10})	$10^4 \alpha'_1$ (K^{-1})	$10^7 \alpha'_2$ (K^{-2})	$10^6 \alpha'_{3/2}$ ($\text{K}^{-3/2}$)		
0				1.8			41.9	386 ¹
	7.5		3.9					
				1.3	1.1		1.8	319 ²
1 ^a	5.6	2.0	0.9	0.7		4.4	1.9	217 ³
				1.9			69.9	353
	9.0		42.4					
2				1.4	1.1		8.3	288
	2.1	7.8	1.6	0.9		4.4	8.7	694 ^b
4 ^a				1.9			28.3	385
	8.1		9.2					
				1.6	0.7		4.3	346
6	5.2	3.0	2.1	1.2		2.8	4.2	381
				1.7			15.6	435
8	6.6		10.0					
				1.4	0.7		5.1	396
	5.8	0.9	9.4	1.1		3.0	5.0	303
10								
				2.0			17.1	367
	8.7		7.2					
12				1.7	0.5		7.0	339
	5.9	2.9	0.5	1.4		2.2	7.0	402

				2.1		48.3	376
	9.0		2.7				
8				1.5	1.1	2.4	315
	7.7	1.4	1.2	1.0		4.7	206
				1.9		33.6	364
	8.6		15.0				
12				1.5	0.7	13.6	323
	4.5	4.2	0.9	1.2		3.1	432
Ave-	8.2±0.9			1.9±0.1	0.8±0.3		381±
rage				1.5±0.1			329±
	5.8±1.1	2.4±1.2		1.1±0.2		3.4±1.0	324±

a. For $x = 1$ and 4 , range of fit at low temperatures is 45-95 K.

b. The numbers in this row are not used for calculating the average

more than an order of magnitude. The fact that there is another term present over and above the T^2 term (here $T^{3/2}$) is further demonstrated in Fig. 3.3. It shows the deviations of individual data points from the best fitted curve (a) using Eq. (1.7a) and (b) Eq. (1.7b) for samples with $x = 0, 1, 6$, and 12 . It is clear that, in the case of (a), the deviation is large and systematic whereas, in the case of (b), it is small and random (i.e., intersecting the zero deviation line more frequently).

Fitting the data between 200 and 300 K to Eqs. (1.8) and (1.9b), significant improvement in the value of χ^2 is achieved with the inclusion of either T^2 [Eq. (1.8a)] or $T^{3/2}$ [Eq.(1.8b)] term over the linear term only [Eq.(1.9b)]. However, there is nothing much to choose between the two alternatives from the χ^2 values. Thus, it is very difficult to conclude whether it is a T^2 or a $T^{3/2}$ term that has to be added to the linear electron-phonon term at high temperatures. We have also tried to fit the data between 200 to 300 K with both terms together, i.e., T^2 and $T^{3/2}$ terms in addition to the linear one. We find that the coefficient of one of the terms (T^2 or $T^{3/2}$) becomes negative and, hence, it is unacceptable in the present context. It should be pointed out that any quantitative analysis involving more terms (here four) demands better resolution of the data.

In order to establish a magnetic contribution (be it T^2 or $T^{3/2}$) on a firmer basis, in Fig. 3.4, $dr(T)/dT$ is plotted against temperature for samples with $x = 0, 2, 6$, and 8 . For $35 < T < 85$ K region, the derivative varies slower than T , which definitely implies that over and above a T^2 term there is a term which varies faster than T but slower than T^2 . The 85-200 K

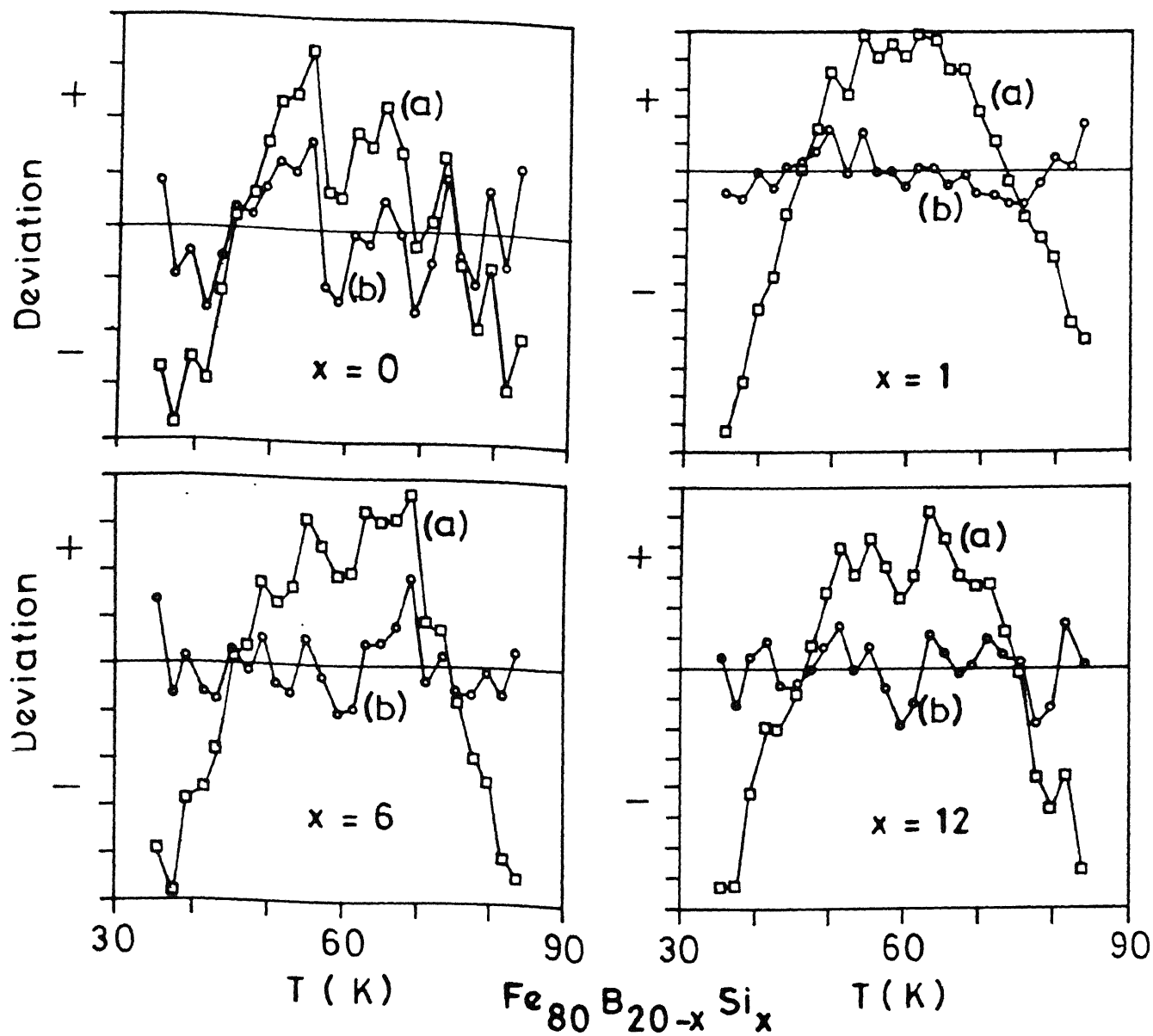


Fig. 3.3 Deviation versus temperature for $x = 0, 1, 6$, and 12 alloys. (a) denotes deviations of data points from fits to Eq. (1.7a) and (b) from fits to Eq. (1.7b).

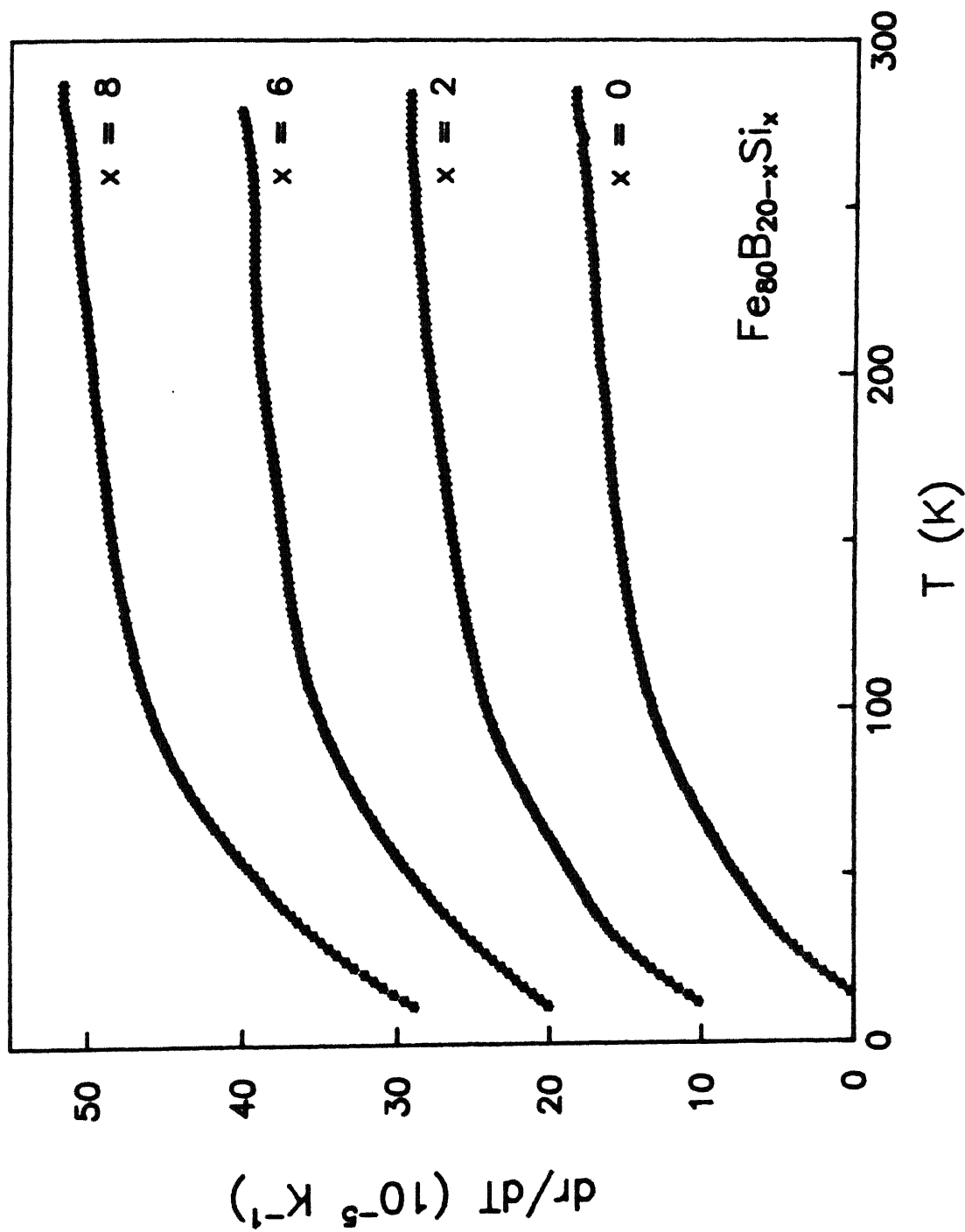


Fig. 3.4 Temperature derivative of the normalized resistivity dr/dT (10^{-5} K^{-1}) as a function of temperature for $x = 0, 2, 6$, and 8 alloys. Each curve is displaced along the dr/dT axis by 10^{-4} with respect to the one below it.

region is one of a transition between two regions where different mechanisms come into play and, hence, has been left out in this quantitative analysis. The derivative curves above 200 K are not horizontal. If there were only a linear term in $r(T)$ (i.e., no magnetic contribution), the derivative would have been a constant. An additional T^2 term will give a derivative which is linear in T . A slight curvature observed here might indicate the presence of a $T^{3/2}$ term instead of a T^2 one.

The values of θ_D , obtained from Eqs. (1.10)-(1.12), are given in Table 3.1. We have intentionally not included the values of α_0 and α'_0 in the table since they are subsequently not used. However, the values are ≈ 0.96 .

It is also observed that the coefficients are rather sensitive to the temperature range of the various fits. Hence, their composition dependence, as well as that of θ_D , which solely depends on these coefficients, could not be determined from the present work. Since the transition-metal (Fe) content is the same in all the alloys, a strong composition dependence is also not expected. However, the coefficients of the magnetic terms [viz., $\alpha_{3/2}$, $\alpha'_{3/2}$, and α'_2 of Eqs. (1.7b), (1.8b) and (1.8a), respectively] depend on various parameters, such as the unit-cell volume, the spin of the local magnetic moment, spin-wave stiffness constant, structure factor, Fermi momentum, etc. [4]. The different kinds of composition dependence of all these factors put together may be partly responsible for the random variation of these coefficients. More reproducible and higher-resolution data are necessary to quantitatively find the effect of composition on these coefficients. The present work only establishes their

values within a factor of 2. Thus, we have included their averages and standard deviations at the end of Table 3.1.

If T^2 is taken as the magnetic term, then the average values of the coefficients $10^7\alpha_2$, $10^4\alpha'_1$, and $10^7\alpha'_2$, obtained by Kaul et al. [8] in $\text{Fe}_{80}\text{B}_{20-x}\text{C}_x$ ($x = 0, 2, 4$, and 10) (5.5 ± 0.7 , 1.0 ± 0.1 , and 0.7 ± 0.3 , respectively) agree very well with those found by us (Table 3.1), namely, 8.2 ± 0.9 , 1.5 ± 0.1 , and 0.8 ± 0.3 , respectively. The resulting θ_D values (330 ± 40) K are realistic and consistent with the literature value for the $x = 0$ alloy [50]. Nevertheless, we also find equally good fits, if not much better at low temperatures, if $T^{3/2}$ is taken as the magnetic term. The values of the coefficients $\alpha_{3/2}$ and $\alpha'_{3/2}$ are nearly equal to each other ($\approx 3 \times 10^{-6} \text{ K}^{-3/2}$) implying that the same $T^{3/2}$ term could exist over the entire temperature range. Their values have the same order of magnitude as that in a different amorphous material Co_4P [4] where the value is $16 \times 10^{-6} \text{ K}^{-3/2}$. However, the values of θ_D , then (if the magnetic term is $T^{3/2}$) become widely different from one another with an average of (324 ± 97) K.

One possible explanation for the apparent discrepancy in θ_D could be the following. Eq. (1.6) is valid for $T \ll T_C$. The lower temperature range for fitting our data to Eqs. (1.7a) and (1.7b) is 35 - 85 K for which $T \leq 0.13 T_C$. Thus, our observation of the $T^{3/2}$ term dominating over the T^2 term at lower temperatures seems quite reasonable. But the higher range for fitting the data to Eqs. (1.8a) and (1.8b) is 200 - 300 K ($T \leq 0.45 T_C$). The latter range may not satisfy the criterion of $T \ll T_C$. As a result, the use of Eq. (1.6) as predicting the magnetic

contribution in this range may not be correct. Thus, the coefficient of the linear term (electron-phonon scattering) α'_1 will be erroneous and will affect the value of θ_D adversely [see Eqs. (1.11) and (1.12)]. However, if that was the case, the set of more reasonable θ_D , obtained from Eq. (1.11), would have to be taken as fortuitous. Thus, we conclude that the magnetic contribution to the total resistivity is indeed through the $T^{3/2}$ term at least for $T \ll \theta_D$. Also, the temperature range $T \geq \theta_D$ is likely to be outside the domain of Eq. (1.6) in predicting the magnetic term.

3.2 Magnetoresistance

The longitudinal ($\vec{J} \parallel \vec{H}$) and transverse ($\vec{J} \perp \vec{H}$) magnetoresistances, given by $\frac{\Delta\rho_{\parallel}}{\rho} = (\rho_{\parallel} - \rho)/\rho$ and $\frac{\Delta\rho_{\perp}}{\rho} = (\rho_{\perp} - \rho)/\rho$, are plotted against H_{ext} for samples with $x = 0, 6$, and 12 in Figs. 3.5, 3.6, and 3.7, respectively at several constant temperatures. We find that these amorphous materials behave very much the same way as their crystalline counterparts, namely, at low fields the longitudinal magnetoresistance is positive while the transverse one is negative. The longitudinal magnetoresistance rises rather fast with increasing field whereas the transverse one drops much more slowly with increasing field. The technical saturation in $\Delta\rho_{\parallel}/\rho$ is attained at a lower field value than that in $\Delta\rho_{\perp}/\rho$. It implies that the domain rotation processes occur at lower applied magnetic field for the longitudinal case than that for the transverse one. This is due to the demagnetization field which depends on the dimension of the sample and its orientation with respect to H_{ext} . In our samples

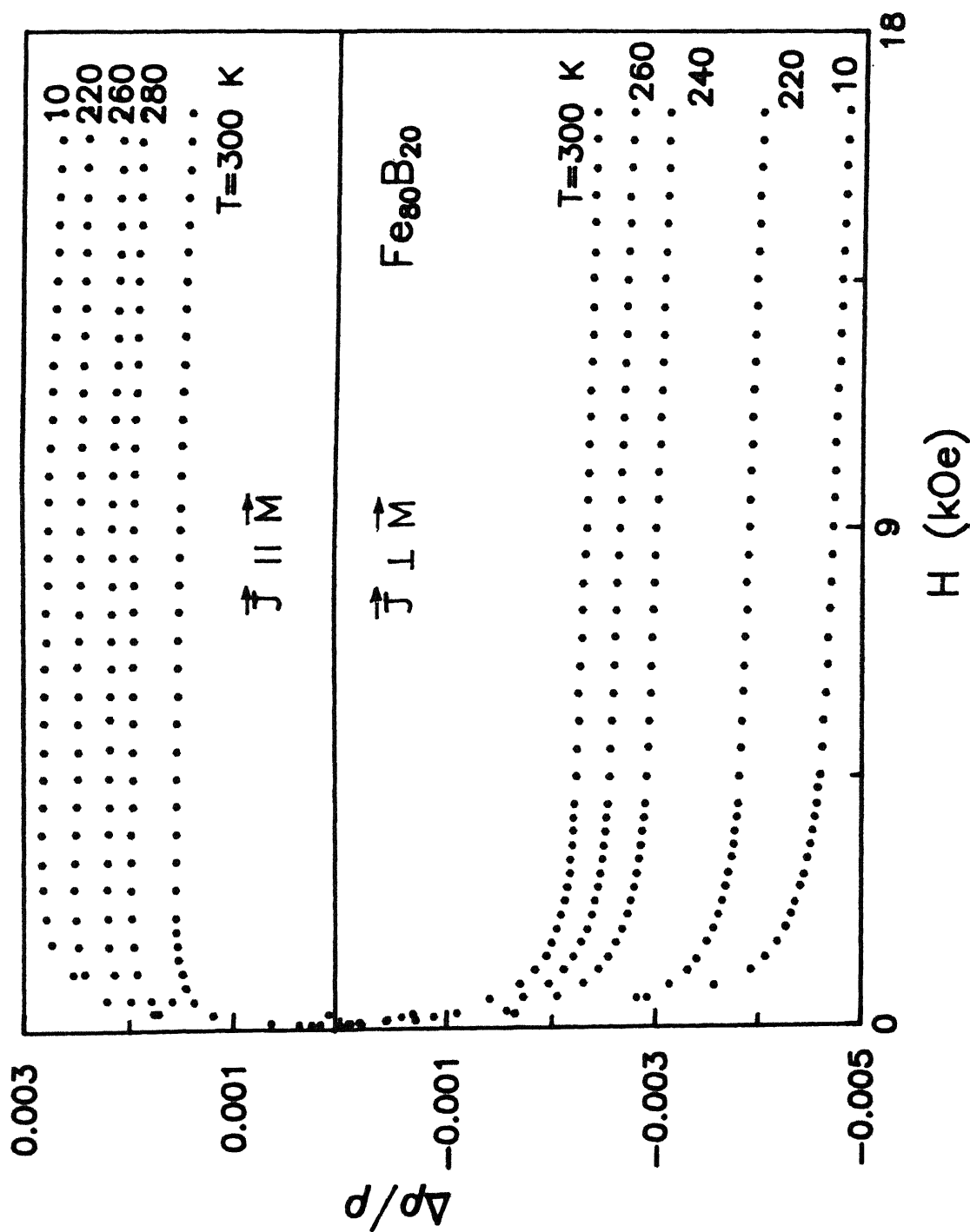


Fig. 3.5 Magnetoresistance ($\Delta\rho/\rho$) versus external magnetic field at several constant temperatures for both longitudinal ($\vec{J} \parallel \vec{M}$) and transverse ($\vec{J} \perp \vec{M}$) orientations for $x = 0$.

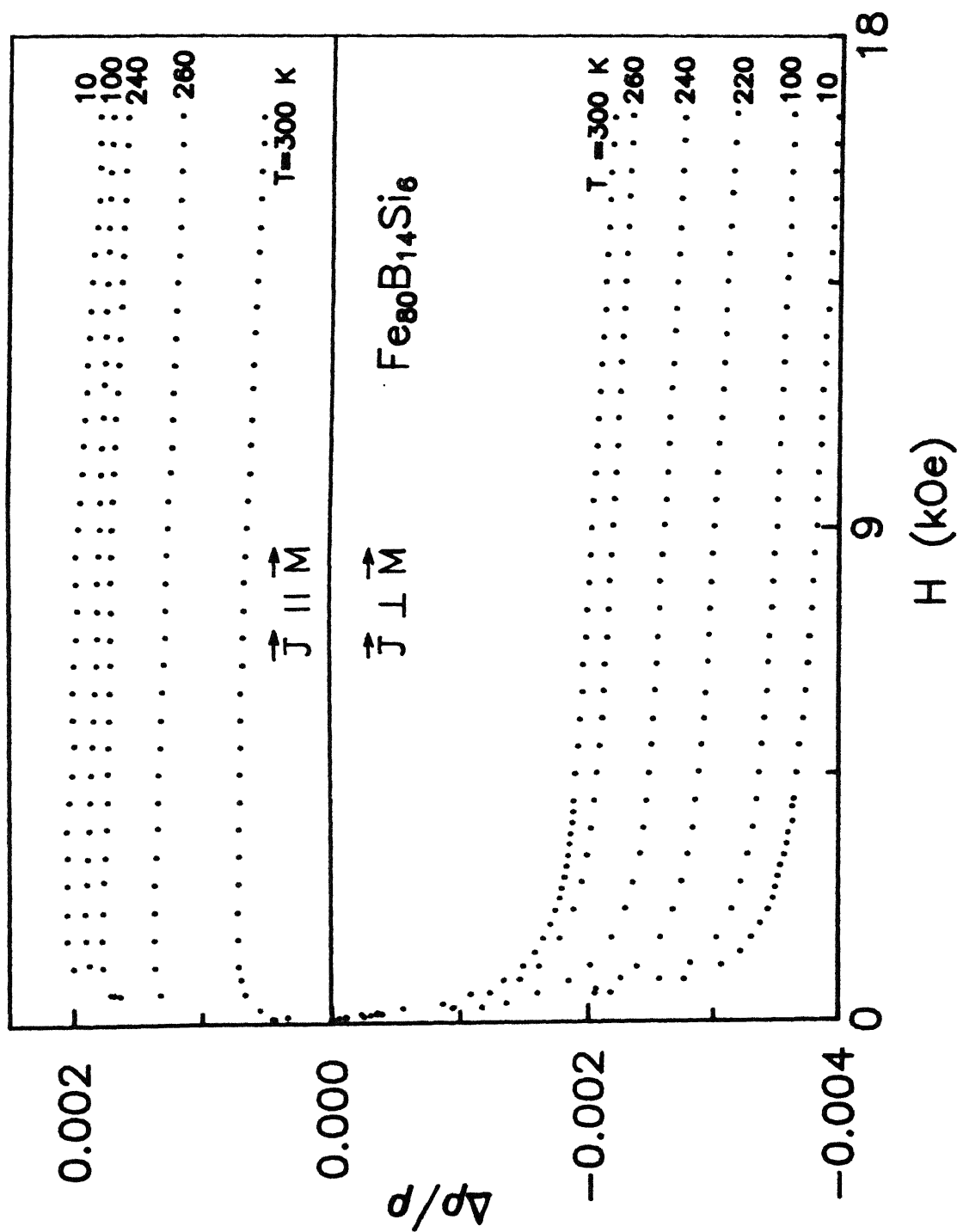


Fig. 3.6 Magnetoresistance ($\Delta\rho/\rho$) versus external magnetic field at several constant temperatures for both longitudinal ($\vec{J} \parallel \vec{M}$) and transverse ($\vec{J} \perp \vec{M}$) orientations for $x = 6$.

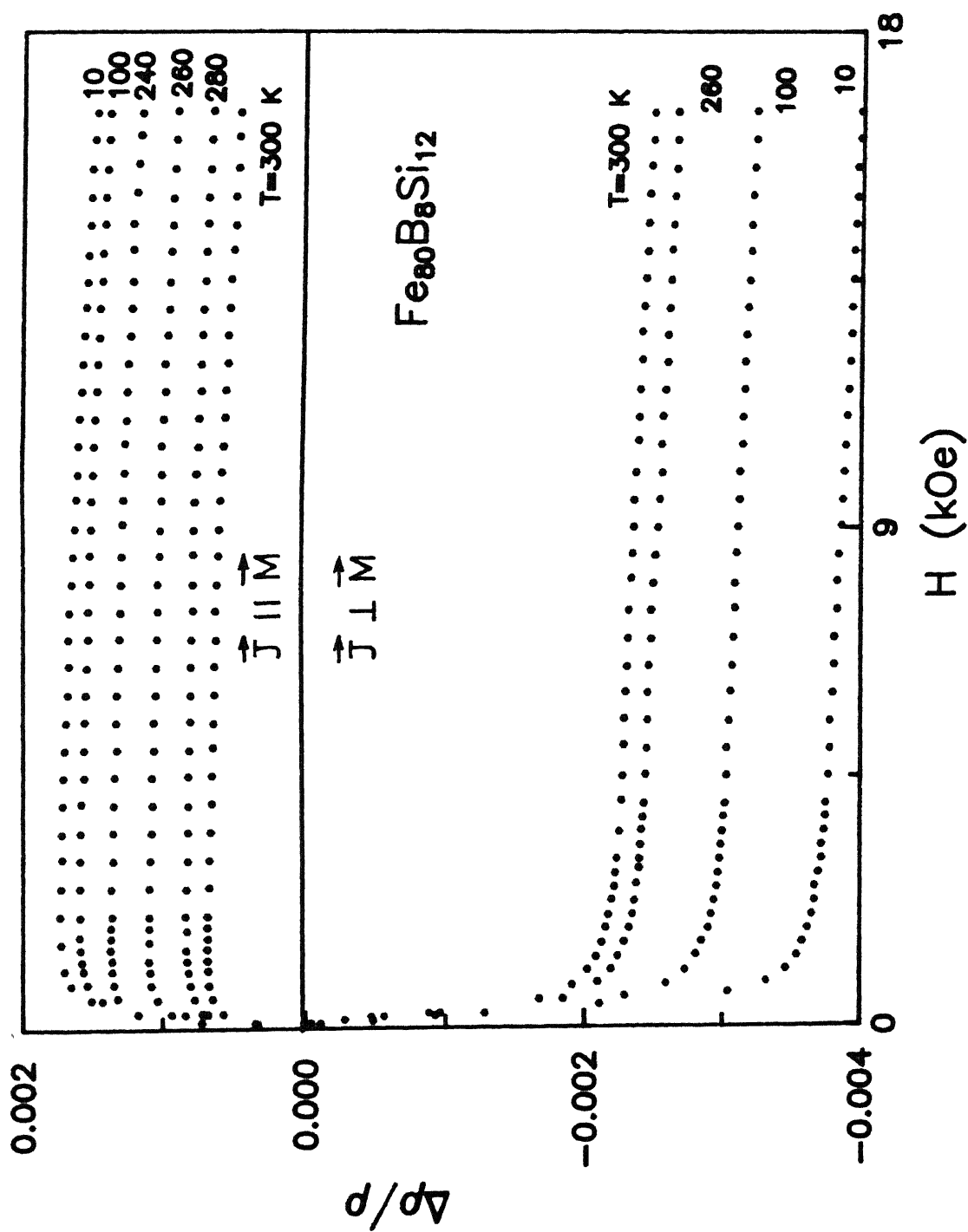


Fig. 3.7 Magnetoresistance ($\Delta\rho/\rho$) versus external magnetic field at several constant temperatures for both longitudinal ($\vec{J} \parallel \vec{M}$) and transverse ($\vec{J} \perp \vec{M}$) orientations for $x = 12$.

H_{demag} is typically 1 Oe for the longitudinal case and 400 Oe for the transverse one, so one has to apply larger field for the transverse case (as $H_{\text{int}} = H_{\text{ext}} - H_{\text{demag}}$). $\Delta\rho_{\perp}/\rho$, in magnitude, is always larger than $\Delta\rho_{\parallel}/\rho$. At higher fields, both of them decrease very slowly but linearly with field above saturation. This negative magnetoresistance observed after saturation can be explained in terms of both the localized and the band models. In the localized model, this effect, i.e., the negative magnetoresistance is due to less electron-magnon scattering as magnons are quenched at higher fields. But in the band model, it is related to the slow increase of magnetization above saturation. This behaviour must be contrasted with the Lorentz force magnetoresistance which is positive for both longitudinal and transverse orientations with $\rho_{\perp} > \rho_{\parallel}$. It varies as H^2 and is sizable only for pure metals or dilute alloys at low temperatures and high magnetic fields.

The ferromagnetic anisotropy of resistivity (FAR) is plotted against temperature for $x = 0, 6$, and 12 in Fig. 3.8(a). The FAR is found to be positive and its value decreases with increasing temperature but at low temperatures (< 200 K) the decrease is very slow. This is also clear from Figs. 3.5-3.7 where we find that the curves for ($T \geq 220$ K) are well separated from each other, resulting in a faster decrease of the FAR with increasing temperature. The slow decrease of FAR with increasing temperature at low temperatures is due to the fact that, in this range of temperature, $T < T_C/3$, where the typical Curie temperature is 660 K. It has been shown by Smit [11] that $\rho_{\parallel} > \rho_{\perp}$, which results in a positive FAR. The ferromagnetic anisotropy

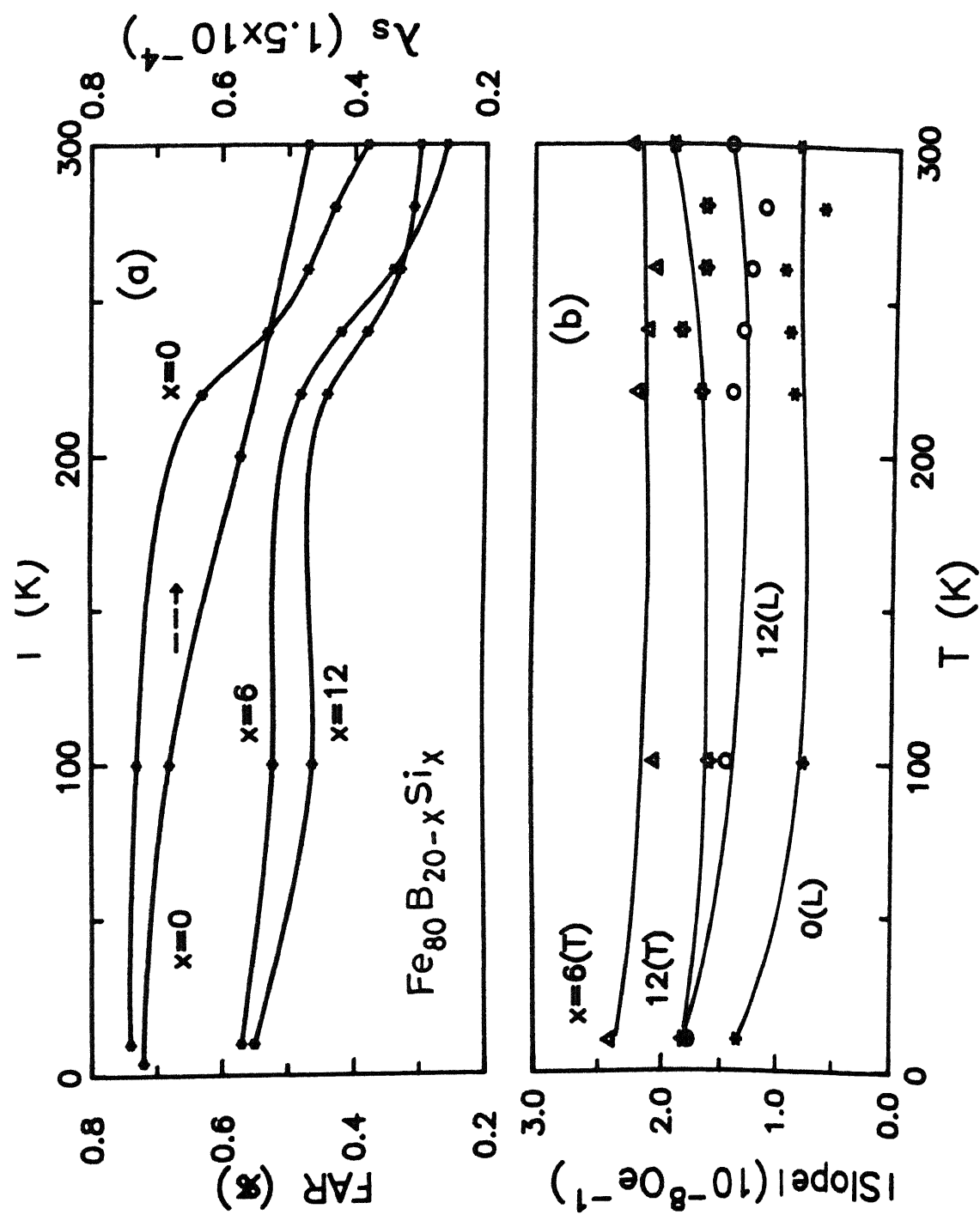


Fig. 3.8 (a) FAR versus temperature for $x = 0, 6$, and 12 . λ_s is also shown for $x = 0$. (b) $\rho^{-1} d\rho/dH$ versus temperature for $x = 0, 6$, and 12 for some orientations. L and T in brackets refer to longitudinal and transverse orientations respectively.

of resistivity has its origin in the spin-orbit interaction present in a ferromagnet. The expression for FAR [Eq. (1.27)] was derived [19] for Ni-based alloys. It has been suggested [51] that the same expression would hold good for Fe-rich alloys if α is defined as $\alpha = \rho_{\uparrow}/\rho_{\downarrow}$. A positive FAR implies that $\alpha > 1$, i.e., $\rho_{\uparrow} > \rho_{\downarrow}$. It is due to the presence of holes in both the d -bands in these alloys. The temperature dependence of FAR can be explained from the above expression. As the temperature increases, thermal vibrations, i.e., the number of phonons also increases. The phonons compete with the exchange splitting, ρ_{\uparrow} tends to equalize with ρ_{\downarrow} , resulting in a decrease of the value of α and hence of the FAR. This justifies the general shape of Fig. 3.8(a). This expression is also used in studying the band structure. According to the analysis by Kaul and Rosenberg [18] in $\text{Fe}_{80}\text{Ni}_{20-x}\text{B}_x$ system, $\text{Fe}_{80}\text{B}_{20}$ has holes in both d_{\uparrow} - and d_{\downarrow} -bands and is a weak ferromagnet on the verge of becoming a strong ferromagnet. Magnetization results [52] of $\text{Fe}_{80}\text{B}_{15}\text{Si}_5$ also indicate the presence of holes in both the exchange split d -bands. Thus, with the addition of Si, no significant change in d -bands occurs. This is also evident from our magnetoresistance results. According to Eq.(1.27), $\Delta\rho/\rho$ is expected to be large for strong ferromagnets and small for weak ferromagnets. A strong ferromagnet has vacant states only in d_{\downarrow} -band while a weak ferromagnet has holes and electrons in both d_{\uparrow} - and d_{\downarrow} -bands. ρ_{\uparrow} and ρ_{\downarrow} have comparable values for a weak ferromagnet since vacant states are available in both d_{\uparrow} - and d_{\downarrow} -bands for s -electrons to make transitions. But for a strong ferromagnet, the value of ρ_{\downarrow} greatly exceeds that of ρ_{\uparrow} as s - d scattering is allowed only for spin-down electrons

because there are no vacant d_{\uparrow} -states at Fermi level. For $\text{Fe}_{80}\text{B}_{20-x}\text{Si}_x$, FAR is quite large indicating that these alloys are more like a strong ferromagnet. Since T_C and the saturation magnetization [53] are found to vary slowly with the Si concentration x , one would expect the FAR to be weakly dependent on x . Our measured value (0.38%) of FAR at room temperature for $x = 0$ is consistent with the literature values [12,14]. However, we find that although the FAR values for $x = 6$ and 12 are nearly the same, they are 30% lower than that for $x = 0$. The large value of the FAR for $x=0$ may be due to the fact that this particular composition is from a different batch of samples. The observation that the value of FAR for $x = 6$ and 12 are the same, is consistent with that of Yao et al. [16]. They also observed that the FAR is not influenced by replacing B by Si but the addition of P, instead of Si, decreases the value of FAR significantly. Kaul and Rosenberg [18] have also noticed, from the observed values of FAR for $\text{Fe}_{80}\text{Ni}_{20-x}\text{B}_x$ and $\text{Fe}_x\text{Ni}_{80-x}\text{B}_{19}\text{Si}_1$, that the FAR does not get affected by the replacement of B by Si. Naka et al. [14] had also observed for $\text{Fe}_{80}\text{B}_{20-x}\text{P}_x$, that the replacement of B by P decreases FAR. We have also plotted the spontaneous linear magnetostriction coefficient λ_s [54] versus T for $x = 0$ in Fig. 3.8(a). It roughly follows the FAR versus T graph since the origin of the two effects lies in the spin-orbit interaction present in a ferromagnet.

In isotropic crystalline ferromagnets, where orientations of spontaneous magnetization are equally probable [see Eq. (1.17)], the ratio $\frac{(\rho_{\parallel s} - \rho)}{(\rho_{\perp s} - \rho)} = -2$. Here, for all three samples, we find that this ratio is ≈ -0.5 . This implies that the

domain magnetization is not randomly oriented in these amorphous ribbons. Using Eq. (1.31), we find from our data at 10 K that $\theta = 38.4^\circ$, 37.3° , and 34.7° for $x = 0$, 6, and 12, respectively. Indeed Mössbauer, scanning electron microscopy and ferromagnetic resonance techniques [55] have established for $x = 0$ that the magnetization \vec{M} lies in the plane of the ribbon and the value of $\theta \simeq 30^\circ$. Thus, our analysis indicates that the replacement of B by Si does not change this special orientation of \vec{M} .

The high-field slope $1/\rho \, d\rho/dH$ ($= d(\Delta\rho/\rho) / dH$), found by a least-squares-fit program, for all the three samples is negative at all temperatures, its magnitude is larger for the perpendicular orientation. This is shown in Fig. 3.8(b) for some cases. In general, the magnitude of the slope [33] should decrease with decreasing temperature since electron-magnon scattering could be effectively reduced as magnons are quenched at higher fields. Its value is proportional to the high-field magnetic susceptibility [12] which decreases with decreasing temperature. However, we find here that, although the slope does not strongly depend on temperature, its magnitude has a small increase to the contrary at lower temperatures. The large slope at lower temperatures thus implies the lack of complete alignment of spin even at 10 K ($T \ll T_C$). We do find from our dc-magnetization measurements that, for $x = 0$, the high-field (15 kOe) susceptibility is as high $1.12 \times 10^{-4} \text{ cm}^3/\text{g}$ at 10 K and not too different from $1.15 \times 10^{-4} \text{ cm}^3/\text{g}$ at 180 K. This observation of increasing magnitude of slope with decreasing temperature is rather common in Fe-based alloys having Invar properties [2]. However, Fig. 3.8(b) shows that the addition of Si suppresses this

effect since the magnitude of the slope does not decrease significantly at higher temperatures.

The raw $R(T)$ data for the $x = 6$ alloy at constant fields of 2, 7, and 14 kOe are plotted in Fig. 3.9. We observe that the resistance decreases with increasing magnetic field for external fields above technical saturation. This is in agreement with the negative slope observed in Fig. 3.8(b) at all temperatures. It must be emphasized here that the data at lower fields are affected by the FAR due to the domain structure and, hence, must be avoided in the analysis of magnetic scattering. The effect of the magnetic field on R is very small, a field difference of 10 kOe changes R by 0.02% only. So, in Fig. 3.9 the curves are shifted along the R -axis so that the difference between them shows up. In the inset of Fig. 3.9, the difference $R(T, 14 \text{ kOe}) - R(T, 7 \text{ kOe})$ has been plotted against temperature.

The $r(T)$ data at constant magnetic fields of 2, 7, and 14 kOe were analyzed in a manner similar to the zero-field case using the same least-squares-fit program. We find that the data fits equally well ($x^2 \simeq 10^{-10}$) to Eqs. (1.7) and (1.8) even in the presence of external magnetic fields. This proves that the temperature dependence of the resistivity is still described by the same equations. However, the coefficients for the magnetic terms show some field dependence only at low temperatures, as is evident from Table 3.2. The inset of Fig. 3.9 also shows that the difference between the data (say, 14 kOe and 7 kOe) initially decreases with increasing temperature and then remains more or less constant at higher temperatures. This could be qualitatively understood as follows: The incoherent electron-magnon scattering

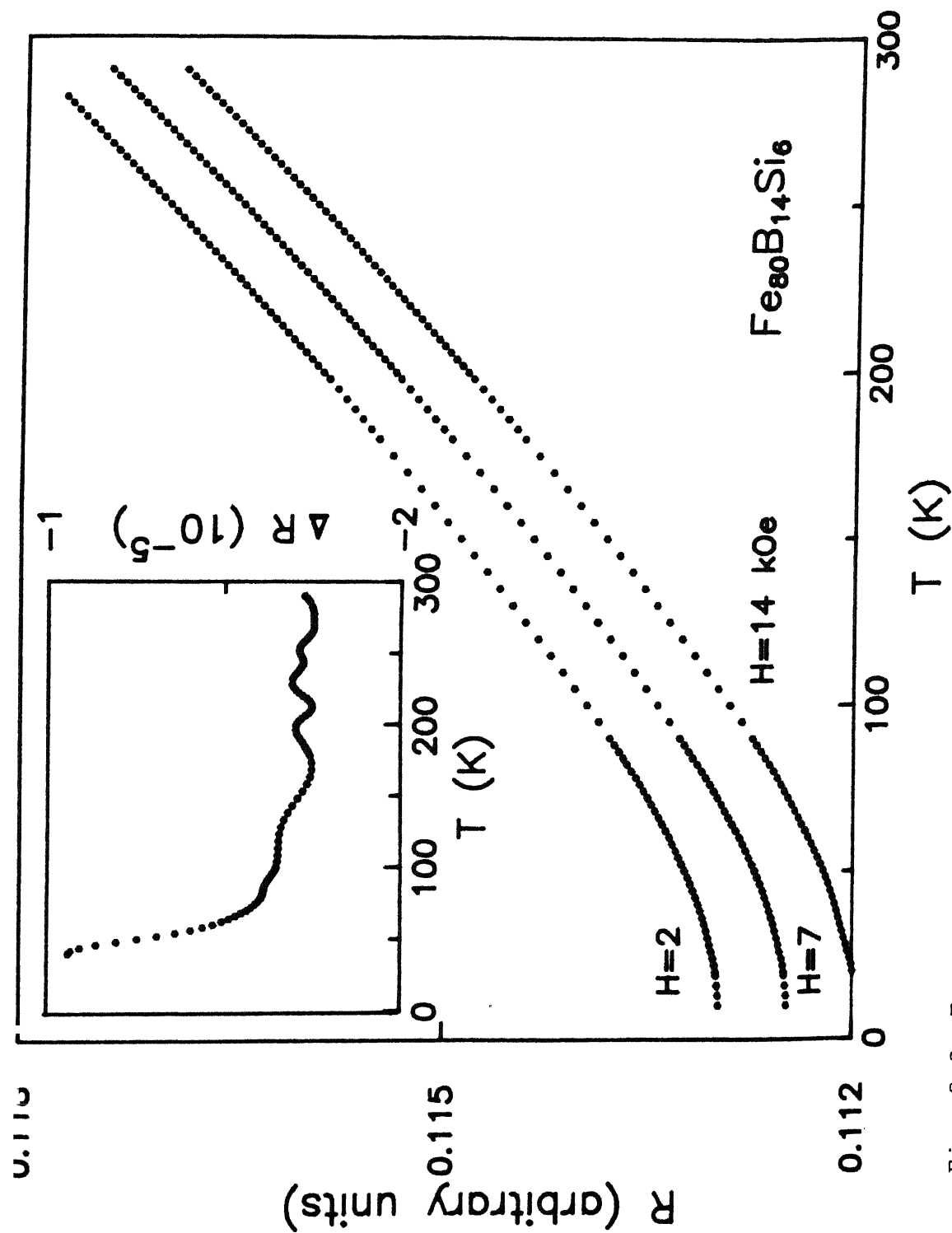


Fig. 3.9 Temperature dependence of electrical resistance $R(T)$ at constant external magnetic fields of 2, 7, and 14 kOe for $x = 6$. The curves are shifted along the R axis for clarity. The inset shows $\Delta R = R(T, 14 \text{ kOe}) - R(T, 7 \text{ kOe})$ versus temperature.

Table 3.2

Magnetic field dependence of the coefficients of the magnetic terms [Eqs. (1.7b) and (1.8b)] in $\text{Fe}_{80}\text{B}_{20-x}\text{Si}_x$ ($x = 0, 6$, and 12) amorphous ferromagnets.

x (at.%)	Range of fit : 35-85 K				Range of fit : 200-300 K			
	$10^6 \alpha_{3/2} (\text{K}^{-3/2})$				$10^6 \alpha'_{3/2} (\text{K}^{-3/2})$			
	H(kOe)	2	7	14	H(kOe)	2	7	14
0(L)		3.4	3.3	3.2		3.9	3.9	4.0
0(T)		2.1	2.1	2.0		4.8	4.8	4.8
6(L)		4.0	3.9	3.8		5.2	5.3	5.3
6(T)		-	4.9	4.8		-	5.8	5.8
12(L)		4.5	4.5	4.3		-	-	-

L : $\vec{J} \parallel \vec{M}$,

T : $\vec{J} \perp \vec{M}$

term, giving $+\alpha_{3/2}(H)T^{3/2}$ dependence, should be smaller at higher fields because of the quenching of magnons resulting in less electron-magnon scattering. This implies that $\alpha_{3/2}$ should decrease with field as is observed at lower temperatures (35-85 K). At higher temperatures (200 - 300 K), the other term $-\alpha_{3/2}(H)T^{3/2}$ [see discussion after Eq. (1.6)] will not decrease that much at higher magnetic fields since the magnetic moment itself increases with field. Thus, the resultant coefficient $\alpha_{3/2}$ may not change with field. This does not happen at lower temperatures because the change of magnetic moment is much less for $T \ll T_C$.

3.3 Low-Temperature Magnetization

The plots of magnetization (M) as a function of applied magnetic field (H) up to 16 kOe at room temperature and at the lowest temperature (19 K) for samples $x = 0, 6$, and 12 are shown in Fig.3.10. The high-field susceptibility (at 15 kOe) of $\text{Fe}_{80}\text{B}_{20}$ is much larger than those containing silicon at both room temperature and 19 K. It is known that the susceptibility of alloys showing Invar effects are large. This indicates that the complete alignment of spins do not take place even at 19 K. This behaviour is also reflected in the magnetoresistance of this sample where the magnitude of the high-field slope ($1/\rho \, d\rho/dH$) at 10 K is larger than that at room temperature. But with the addition of Si in place of B, the susceptibility decreases, becoming nearly zero in the whole range of temperature between 300 and 19 K (within the experimental resolution). This result

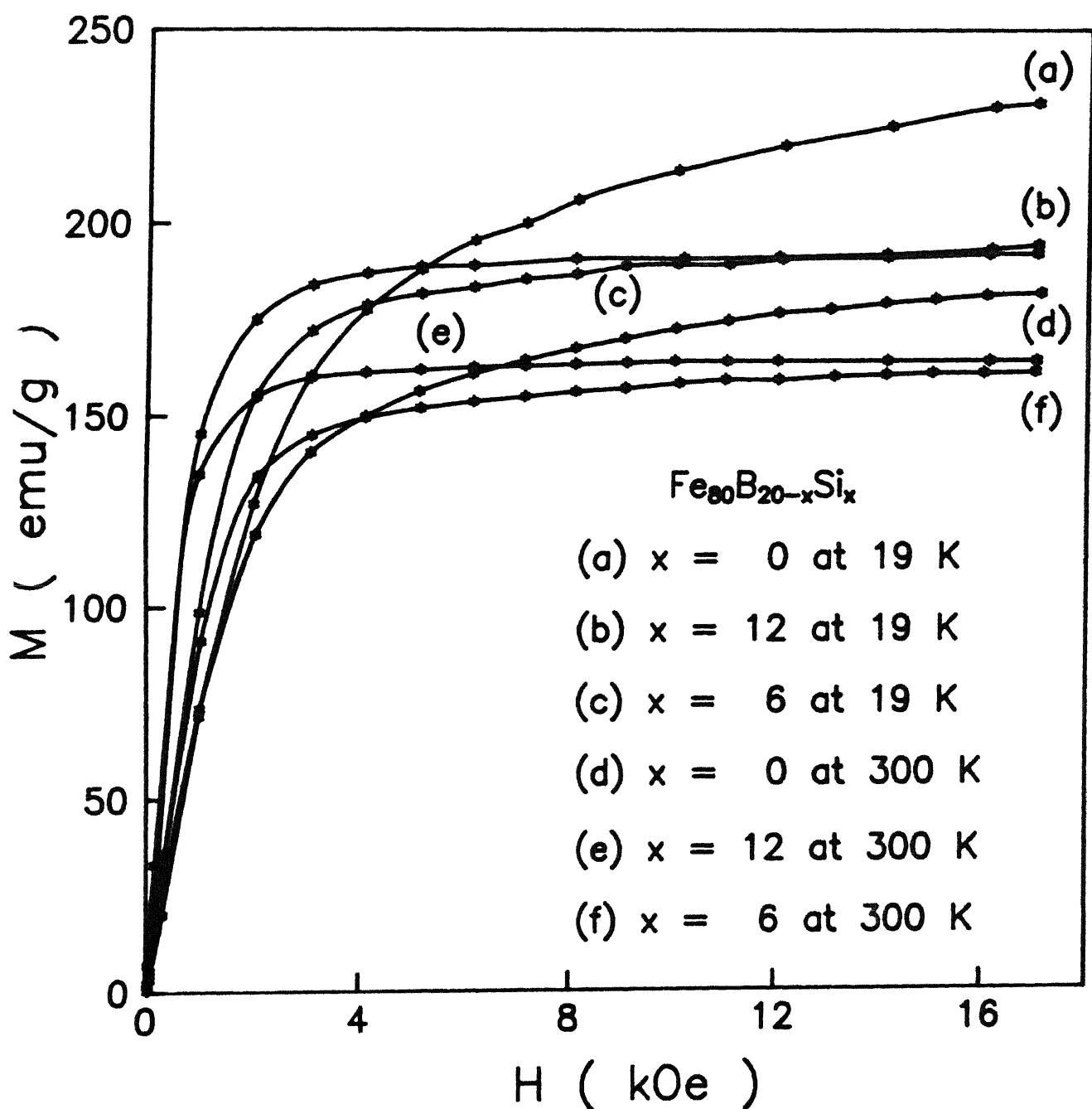


Fig. 3.10 Magnetization M versus external magnetic field H at room temperature and at 19 K for $Fe_{80}B_{20-x}Si_x$ ($x = 0, 6$, and 12) alloys.

however does not correlate with the magnetoresistance data. The magnitude of the high-field slope, as a function of Si concentration, shows an increase at both 300 and 19 K, rather than the expected decrease. The high-field linear extrapolation of M to zero field for all the three samples does not show any variation with the Si content. The magnetic moment per Fe atom at 19 K is calculated from the value of M at 6 kOe. The value of $1.95 \mu_B$, thus obtained, is in agreement with those reported in the literature [56]. However, it is smaller than that of pure Fe in crystalline form ($2.2 \mu_B$). This reduction is understood on the basis of the charge-transfer model (rigid-band model). In this model it is assumed that the metalloid atoms contribute some of their s - and p -electrons to fill the d -bands of the transition metal. This leads to a decrease in the magnetization of the amorphous metal with increasing metalloid content.

The magnetization, as a function of temperature in an external field of 6 kOe is shown in Fig. 3.11 and is taken with the cryotip switched off for eliminating the noise generated by the movement of the piston in the expansion engine of the cryotip while it is on. In this condition the heating rate, though very rapid initially, stabilizes to about 1 K/min at higher temperatures. This ensures near equilibrium condition. A positive pressure of helium exchange gas is maintained in the sample zone and the platinum resistance thermometer almost touches the sample ensuring that the temperature measured and the sample temperature are nearly the same. The T_C , obtained from high-temperature magnetization studies, is in the range of 660 K. In amorphous materials, it is observed that the region in temperature where the

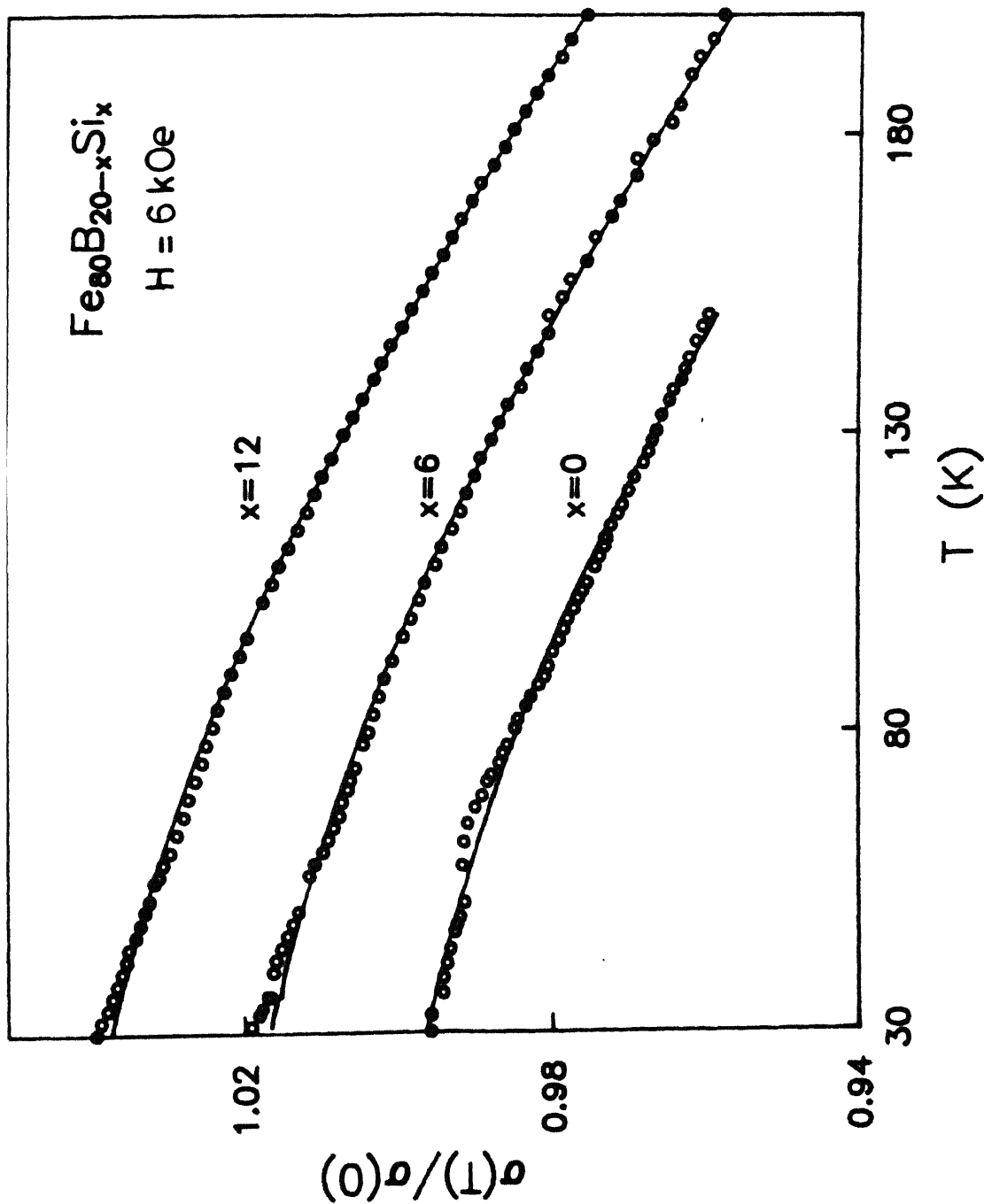


Fig. 3.11 Normalized magnetization $\sigma(T)/\sigma(0)$ versus temperature for amorphous $\text{Fe}_{80}\text{B}_{20-x}\text{Si}_x$ ($x = 0, 6$, and 12) alloys. The curves are shifted along the σ axis for clarity. The solid curves are fits of the experimental data to Eq. (1.36).

spin-wave picture holds good extends to temperatures beyond $0.4 T_C$. Here we have analyzed the data between 19 and 200 K, though the first few data points are left out. We have fitted the data to Eq. (1.36) in two ways, once by including the $T^{5/2}$ term and the other by excluding it (i.e., including only the $T^{3/2}$ term). The function $Z[3/2, T_g/T]$ and $Z[5/2, T_g/T]$ are calculated by using Eqs. (1.37) and (1.38). The gap temperature $T_g = g\mu_B H/k_B$ is about 1.8 K. The data fits well in the second case till $0.4 T_C$ in all three samples with a χ^2 value consistent with the experimental resolution. The coefficient β , thus obtained ($2.5 \times 10^{-5} \text{ K}^{-3/2}$), is in agreement with the value ($2.6 \times 10^{-5} \text{ K}^{-3/2}$) for $\text{Fe}_{80}\text{B}_{20}$ from magnetization measurements [57]. On substitution of B by Si, the value of β hardly shows any change. In the first case, when the $T^{5/2}$ term is also included in the fit, its coefficient γ is of random sign and the χ^2 values do not show any significant improvement, thereby suggesting that the additional terms cannot be meaningfully incorporated. Thus the higher order terms, viz., T^2 , $T^{5/2}$, $T^{7/2}$, T^4 , etc., normally arising due to single particle excitations, additional terms in the dispersion relation, temperature dependence of the spin-wave stiffness constant etc., could not be considered here. The data are not accurate enough to resolve these terms, whose coefficients are generally about 1000 times smaller than that of the dominant $T^{3/2}$ term [32]. This result is in contrast to those obtained in Fe-B-C system where a change of about 30% occurs in the value of β between $\text{Fe}_{80}\text{B}_{20}$ and $\text{Fe}_{80}\text{B}_{12}\text{C}_8$ [32]. Thus, the effect of replacing B by Si is negligible as compared to B by C. The value of β remains almost the same and since M at 19 K also shows no significant change, the

value of D obtained (assuming that the density does not vary significantly with the addition of Si) also does not show any measurable change (Table 3.3). The value of $D = 84 \text{ meV } \text{\AA}^2$ is in agreement with the reported value ($83 \text{ meV } \text{\AA}^2$) in $\text{Fe}_{80}\text{B}_{20}$ [57].

Table 3.3

Comparison of $\sigma(19 \text{ K})$, β , D , and $\bar{\mu}$ in $\text{Fe}_{80}\text{B}_{20-x}\text{Si}_x$
($x = 0, 6$, and 12) amorphous ferromagnets.

x (at.%)	$\sigma(19 \text{ K})$ (emu/g)	$-\beta$ ($10^{-5} \text{ K}^{-3/2}$)	D ($\text{meV } \text{\AA}^2$)	$\bar{\mu}$ (μ_B)
0	195.5	2.50 ($2.6^a, 1.9^c$)	83.5 ($83^a, 99^c$)	1.95 (1.94) ^b
6	183.3	2.44	88.2	1.83
12	189.0	2.48	85.5	1.89

^aReference 57, ^bReference 56, and ^cReference 32

The calculated D values are nearly half of that obtained from neutron scattering measurements [58]. It is observed that there is a discrepancy in the value of the spin-wave stiffness constant D , obtained from magnetization/Mössbauer and neutron scattering measurements. The discrepancy is large in $\text{Fe}_{1-x}\text{B}_x$ alloys ($x = 14$ and 20). This is explained in terms of the Invar effects observed in these alloys [59]. The value of D is also known to be a function of T_C . D decreases as T_C goes down. In these alloys the value of T_C shows only a small increase and therefore does not significantly affect D .

From the above observations, we see that the addition of

Si in place of B does not change the magnetic properties (within the experimental error). This is in contrast to that expected from a charge-transfer model. Carbon and silicon have similar outer electron configuration, and so should have similar effects on the magnetic properties. That the charge-transfer model does not satisfactorily explain the effect of addition of metalloids to transition metals is also in evidence from Mössbauer experiments. The data of Wagner et al. [60] on $\alpha\text{-Fe}_{80}\text{G}_y\text{B}_{20-y}$ ($\text{G} = \text{Ge}, \text{Si}, \text{C}$ or P) show that replacement of B by C causes a slight increase in the average hyperfine field distribution $\langle H_{\text{hyp}} \rangle$, whereas according to the rigid-band model it should have decreased. Similarly, with the substitution of B by Si or Ge, $\langle H_{\text{hyp}} \rangle$ is expected to decrease, but the experimental evidence is in contradiction to it. We also observe a similar increase in $\langle H_{\text{hyp}} \rangle$ in the alloys with Si. However, the substitution of B by P causes a decrease. This shows that the charge-transfer model does not explain the results completely. It is suggested that the size of the metalloids could play a role.

3.4 High-Temperature Magnetization

Figs. 3.12 - 3.14 show the low-field magnetization M (in arbitrary units) as a function of temperature T for $\text{Fe}_{80}\text{B}_{20-x}\text{Si}_x$ ($x = 0, 1, 2, 4, 6$, and 12) alloys. The following observations can be made from these plots. The first fall corresponds to the transition from an amorphous ferromagnetic (a_f) to an amorphous paramagnetic (a_p) state. This temperature is identified as the Curie temperature (T_C) of the glassy phase. Secondly, on further increase of temperature each sample exhibits a rapid increase in M

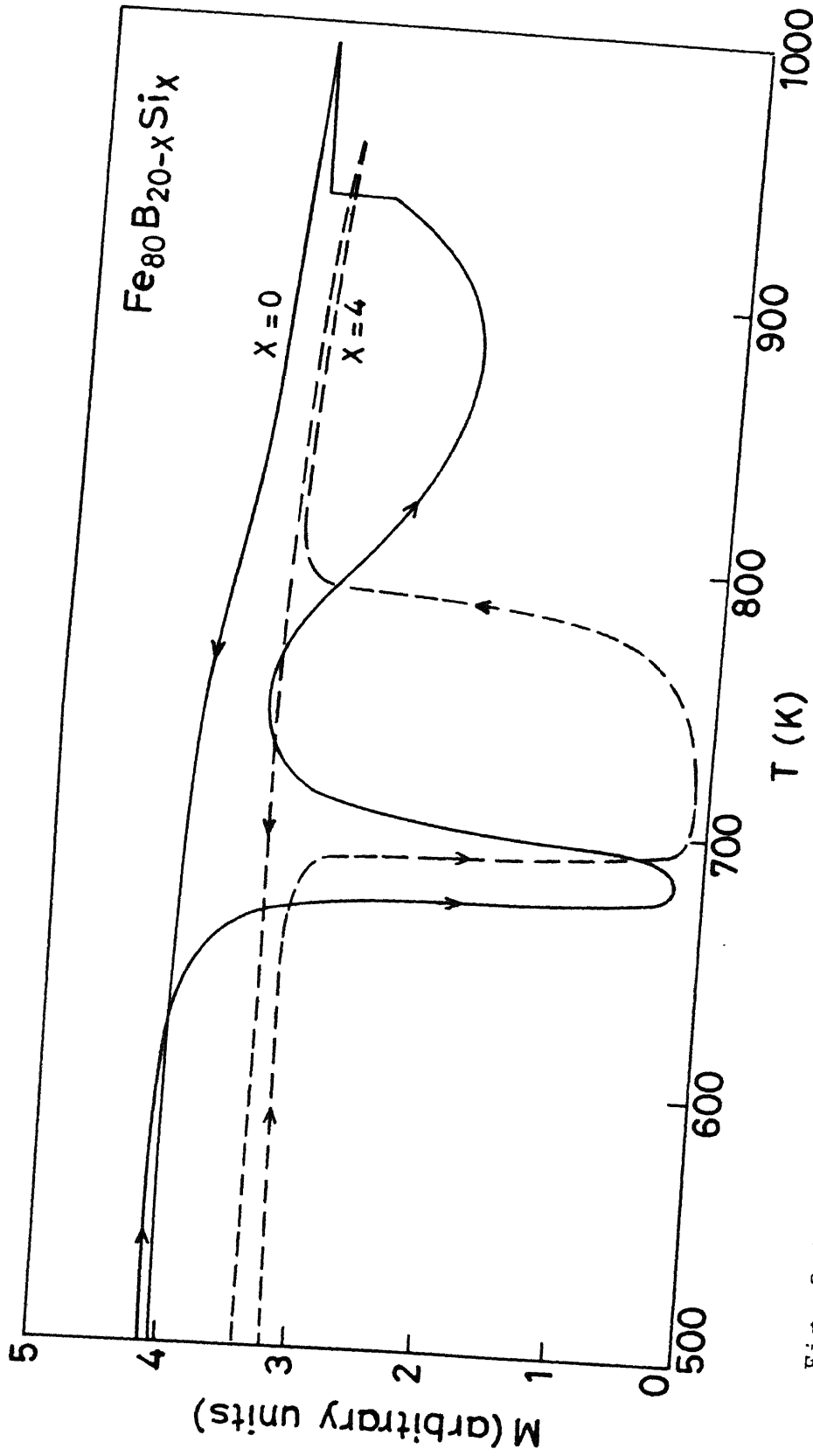


Fig. 3.12 Low-field magnetization M at $H \approx 30$ Oe as a function of temperature for amorphous $\text{Fe}_{80}\text{B}_{20-x}\text{Si}_x$ ($x = 0$ and 4) alloys.

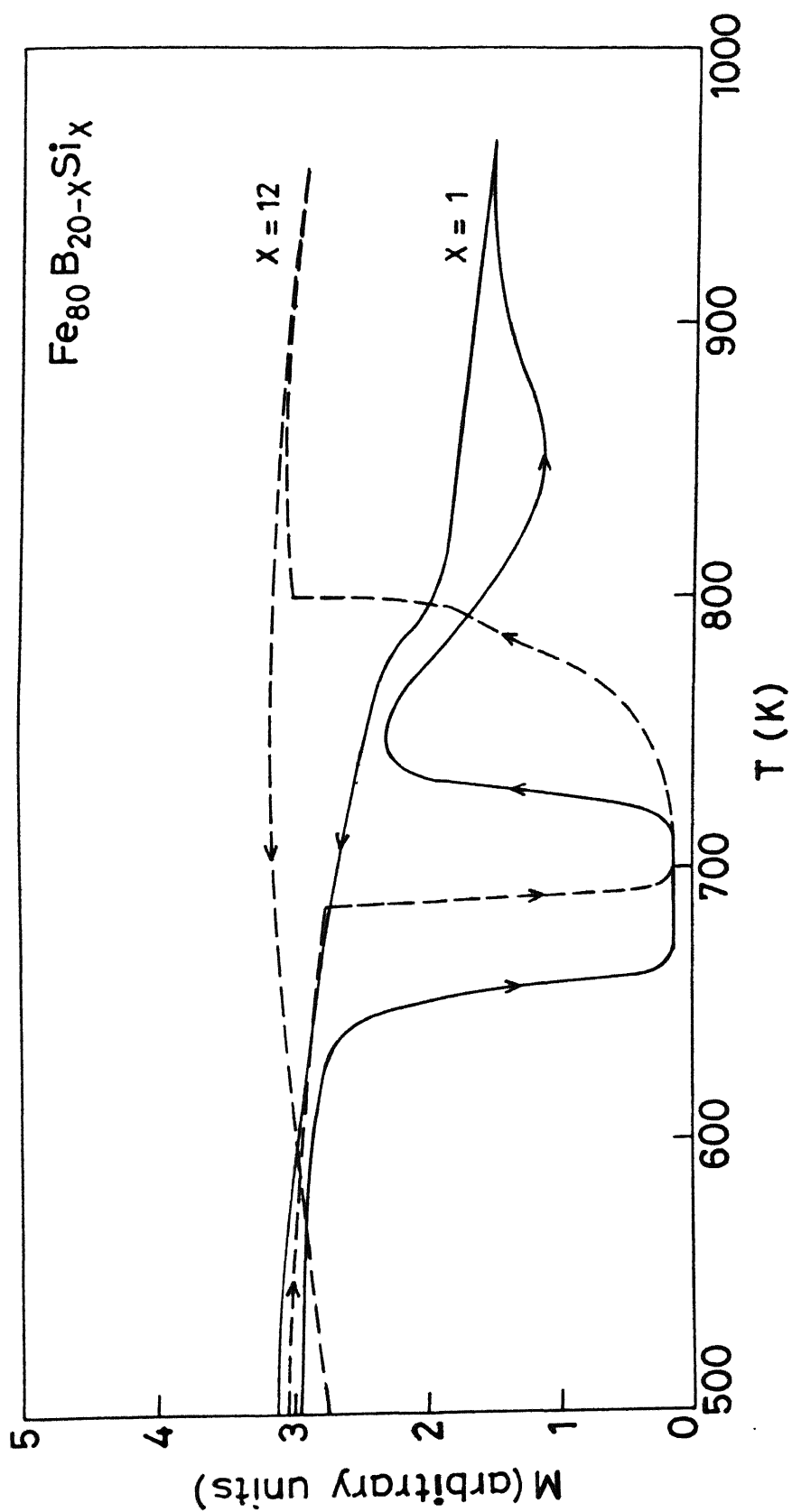


Fig. 3.13 Low-field magnetization M at $H \approx 30$ Oe as a function of temperature for amorphous $\text{Fe}_{80}\text{B}_{20-x}\text{Si}_x$ ($x = 1$ and 12) alloys.

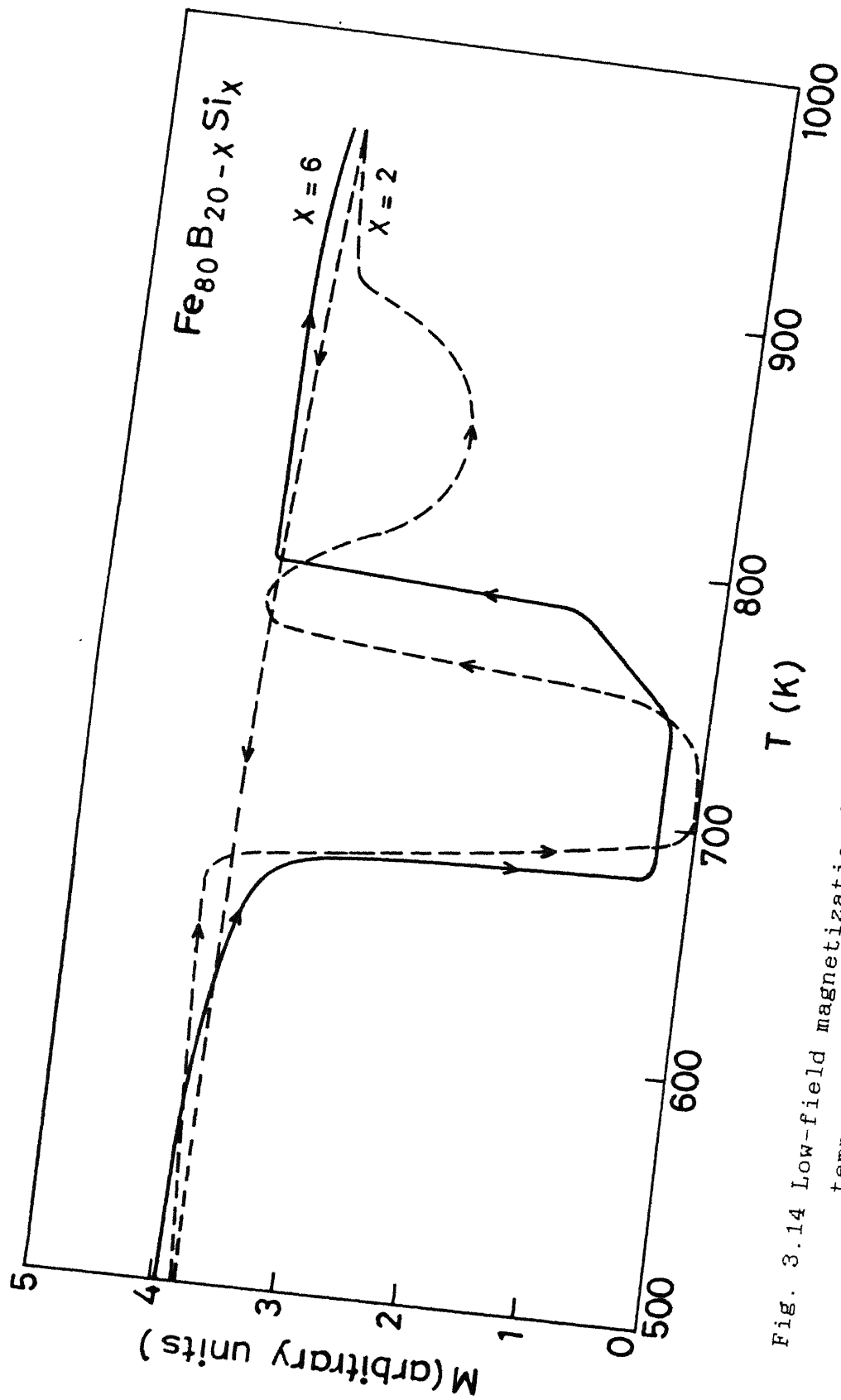
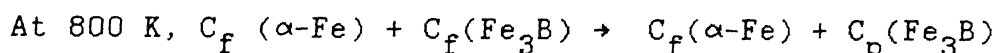
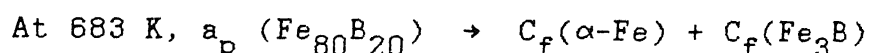


Fig. 3.14 Low-field magnetization M at $H \approx 30$ Oe as a function of temperature for amorphous $\text{Fe}_{80}\text{B}_{20-x}\text{Si}_x$ ($x = 2$ and 6) alloys.

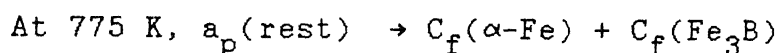
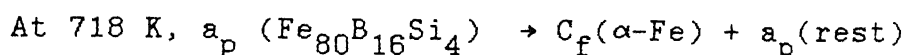
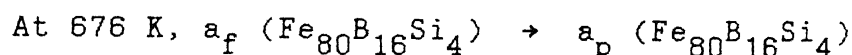


Thus we find that the crystallization of $\text{Fe}_{80}\text{B}_{20}$ is taking place in a single step.

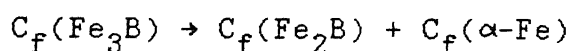
The continuous curves of Fig. 3.13 and 3.14 show the same kind of crystallization sequence for $x = 1$ and $x = 2$. Their final crystalline phases are also $\alpha\text{-Fe}$ and Fe_3B . It can be seen quite clearly that even an addition of Si by only two atomic % increases the crystallization temperature from 683 K ($x = 0$) to 715 K ($x = 2$). Apart from this, the Curie temperature T_C also increases by ≈ 6 K. For $\text{Fe}_{80}\text{B}_{20}$, Fe and B are present in the ratio 4 : 1, this ratio is very close to 3 : 1 and hence the crystallization occurs in a single step. The same is true for $\text{Fe}_{80}\text{B}_{19}\text{Si}_1$ and $\text{Fe}_{80}\text{B}_{18}\text{Si}_2$.

The dashed curve of Fig. 3.12 represents the magnetization of $x = 4$. The first fall (680 K) corresponds to the transition from an amorphous ferromagnetic (a_f) to an amorphous paramagnetic (a_p) state. At 718 K, the moment starts rising slowly but at 775 K, there is an unexpected rise in the moment. Such a rise in the moment could not be due to $\alpha\text{-Fe}$ precipitation only. The moment of Fe_3B phase, on the other hand, can not be so large near its Curie temperature of 800 K [26]. However, this is possible if there appears other crystalline phases having high enough T_C , e.g., Fe_3B decomposing into Fe_2B and $\alpha\text{-Fe}$. Thus, most probably, this sharp rise in the moment indicates that at 775 K, Fe_3B has crystallized as well as has decomposed into $\alpha\text{-Fe}$ and Fe_2B in their ferromagnetic states. After 800 K, the moment more or less remains constant. The transition of $\alpha\text{-Fe}$ and Fe_2B

ferromagnetic phases to paramagnetic phases could not be observed as our experiment had to be terminated at 960 K and the T_C of α -Fe is 1043 K and that of Fe_2B is 1015 K [26]. While cooling we do not see any step as the two equilibrium phases, α -Fe and Fe_2B , have their T_C 's above 1000 K. The crystallization sequence of $\text{Fe}_{80}\text{B}_{16}\text{Si}_4$ can be schematically represented as :



and



In this metallic glass ($x = 4$), Fe and B are present in the ratio 5 : 1, hence α -Fe precipitates first until this ratio becomes 3 : 1 and then only the Fe_3B phase starts crystallizing.

Similarly, the dashed curves of Fig. 3.13 and 3.14 show the magnetization for $x = 6$ and $x = 12$. For $x = 12$, the two-step crystallization is more prominent as it can be seen clearly from the magnetization curve. Around 800 K, there is a sudden rise in the value of the magnetic moment. This can be similarly explained in terms of simultaneous crystallization and decomposition of Fe_3B as in the case of $x = 4$ alloy. For $x = 4, 6, 8$, and 12, the crystallization takes place in two steps. The T_C , as well as T_x , are plotted in Fig. 3.15(a) and 3.15(b) as a function of Si concentration. It has been observed that T_C increases with the addition of Si. Mitera et al. [53] have observed the increase of T_C with the addition of Si in the $\text{Fe}_{80}\text{B}_{20-x}\text{Si}_x$ series. The value of T_C reported by them are 675 K and 700 K for $x = 0$ and $x = 12$

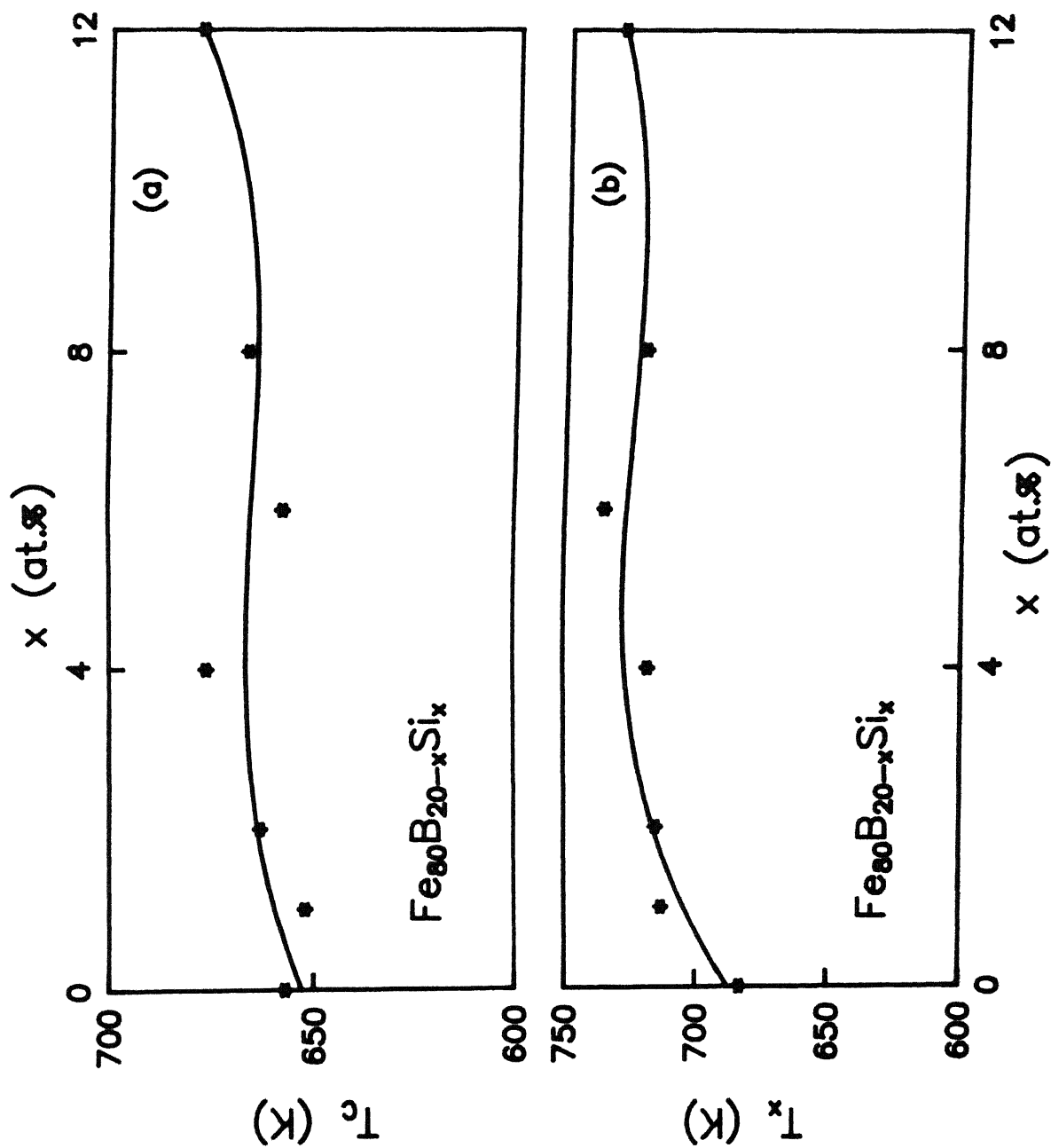


Fig. 3.15 (a) Curie temperature T_C versus x (b) Crystallization temperature T_x versus x for amorphous $\text{Fe}_{80}\text{B}_{20-x}\text{Si}_x$ ($x = 0, 1, 2, 4, 6, 8, \text{ and } 12$) alloys.

respectively. These values are different from those of ours by 15-20 K. This difference could be due to two reasons. One is from the different heating rates used in the two measurements. The second is that the different methods for determining T_C may give slightly different results. It has also been observed from the above figure that the addition of Si increases the crystallization temperature T_x from 683 K ($x = 0$) to 730 K ($x = 12$). It implies that the thermal stability of the system has increased. Luborsky et al. [61] had also observed an increase of the thermal stability on replacement of B by Si in Fe-B-Si system while for $\text{Fe}_{84}\text{B}_{16-x}\text{C}_x$ ($x = 0$ to 10) alloys, Araj's [62] found that the thermal stability decreases with increasing C. Luborsky et al. [63] also reported that for Fe content above 84%, T_x increases as B is replaced by C but for low Fe content, T_x first increases and then it decreases as B is replaced by C while in Fe-B-Si system T_x increases as B is replaced by Si.

Finally it is concluded that the addition of Si ($x \geq 4$) to $\text{Fe}_{80}\text{B}_{20}$ makes the crystallization to occur in two steps and even helps the metastable Fe_3B phase to decompose into the stable $\alpha\text{-Fe}$ and Fe_2B phases.

X-ray Diffraction Studies

The X-ray analysis of $\text{Fe}_{80}\text{B}_{20-x}\text{Si}_x$ ($0 \leq x \leq 12$) samples [Fig. 3.16], after thermomagnetic studies, shows a number of lines whose d-spacings are given in Table 3.4 as d_{obs} . Also, the characteristic lines of $\alpha\text{-Fe}$, tetragonal(t)- Fe_2B , and t- Fe_3B are given as d_{std} [64]. In Table 3.4, I_{obs} is the relative intensity of the peak observed with respect to the maximum intensity peak.

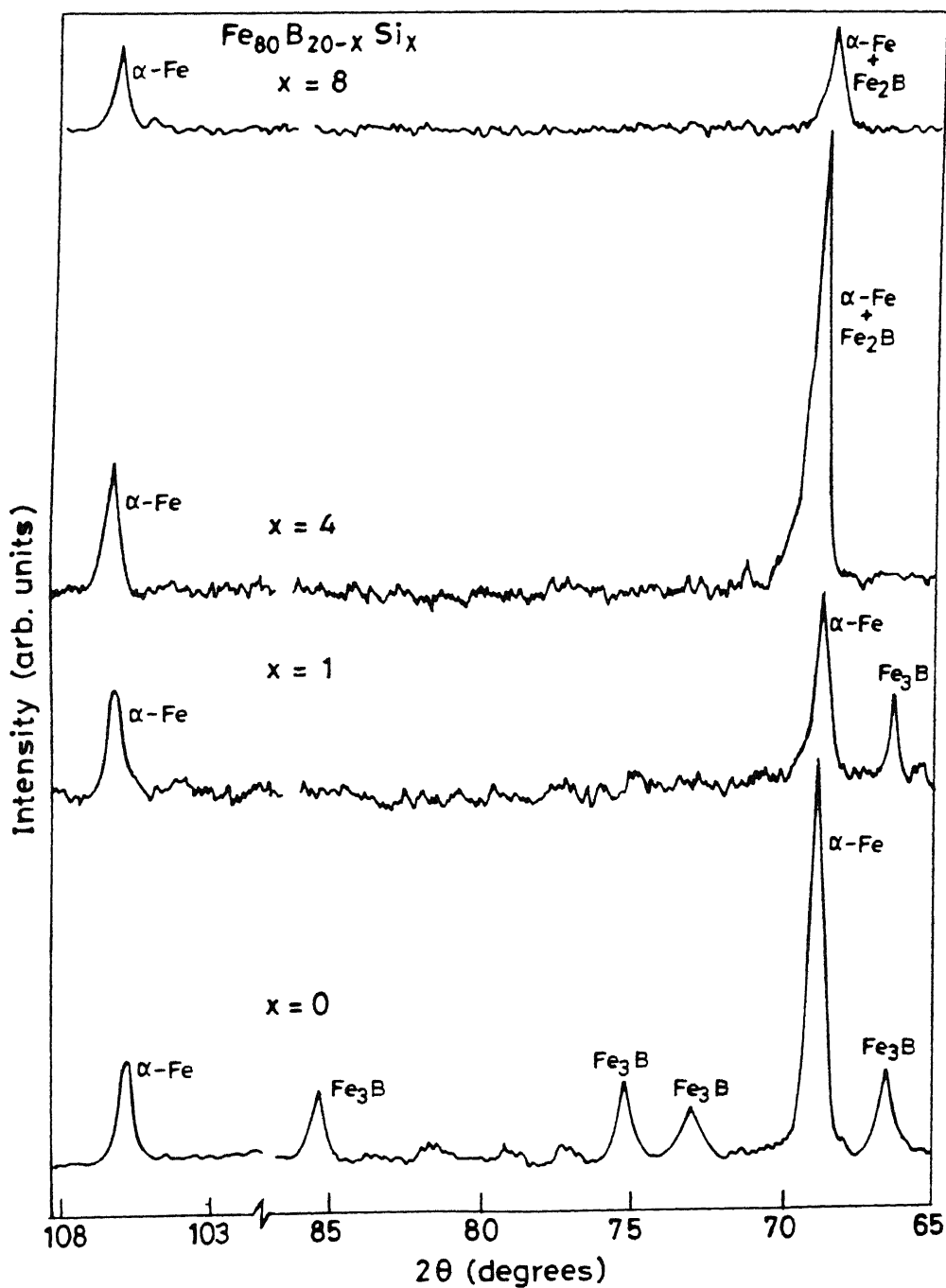


Fig. 3.16 X-ray diffraction pattern after low-field, high-temperature magnetization studies for $\text{Fe}_{80}\text{B}_{20-x}\text{Si}_x$ ($x = 0, 1, 4, \text{ and } 8$) alloys.

Table 3.4

X-ray analysis of $\text{Fe}_{80}\text{B}_{20-x}\text{Si}_x$ ($x = 0, 1, 2, 4, 6, \text{ and } 8$) after high-temperature magnetization studies.

$x(\text{at.}\%)$	Phase	d_{obs}	d_{std}^a	I_{obs}	I_{std}
0	$\alpha\text{-Fe}$	2.027	2.027	100	100
		1.432	1.433	13	20
	Fe_2B	N.P.	2.01	-	100
		N.P.	2.12	-	25
		N.P.	1.63	-	18
		N.P.	1.20	-	20
	Fe_3B	2.087	2.088	17	100
		N.P.	2.028	-	100
		1.93	1.93	9	80
		1.88	1.88	12	100
		1.69	1.69	10	60
1	$\alpha\text{-Fe}$	2.027	2.027	100	100
		1.433	1.433	16	20
	Fe_3B	2.088	2.088	20	100
2	$\alpha\text{-Fe}$	2.027	2.027	100	100
		1.433	1.433	15	20
4	$\alpha\text{-Fe}$	2.027	2.027	100	100
		1.432	1.433	19	20
	Fe_2B	2.01	2.01	34	100
6	$\alpha\text{-Fe}$	2.020	2.027	100	100
		1.430	1.433	17	20
	Fe_2B	2.01	2.01	69	100
8	$\alpha\text{-Fe}$	2.027	2.027	100	100
		1.431	1.433	18	20
	Fe_2B	2.01	2.01	70	100

N.P = Not Present, ^aReference 64.

It is found from a comparison between d_{obs} and d_{std} that for $x = 0 - 1$, the final crystalline phases are $\alpha\text{-Fe}$ as well as $t\text{-Fe}_3\text{B}$. But, for $x = 2$, no $t\text{-Fe}_3\text{B}$ lines have been observed while the thermomagnetic study for this sample has shown the presence of the $t\text{-Fe}_3\text{B}$ phase. This difference could be due to the fact that the Fe_3B phase has been formed in small amounts and hence, was not detectable by X-ray diffraction studies. For $x = 4, 6$, and 8 , lines of $\alpha\text{-Fe}$ as well as Fe_2B are observed. Thus the crystallization scheme, which was proposed for the whole series on the basis of high temperature magnetization studies, is confirmed by the X-ray results of the crystallized samples.

3.5 Mössbauer Spectroscopy

In the following we present the results of Mössbauer spectra for $\text{Fe}_{80}\text{B}_{20-x}\text{Si}_x$ ($x = 0, 2$, and 8) recorded at room temperature using a constant acceleration Mössbauer spectrometer described in Sec. 2.3. These Mössbauer spectra were analyzed with the help of a computer program using Lorentzian shapes for the peaks. The Mössbauer spectra, observed by us for the as-prepared (i.e., as-received) samples, exhibit well-defined but broadened six-line patterns as shown in Fig. 3.17. Such broadened spectral lines are characteristic of amorphous magnetic solids. The broad nature of these lines is due to the large number of structurally inequivalent Fe-sites in the disordered atomic arrangements of these solids [65-67]. It is now well-known that unique hyperfine interaction is observed in crystalline solids while a distribution of hyperfine interactions are observed in amorphous alloys.

Mössbauer parameters, obtained by computer analysis, for

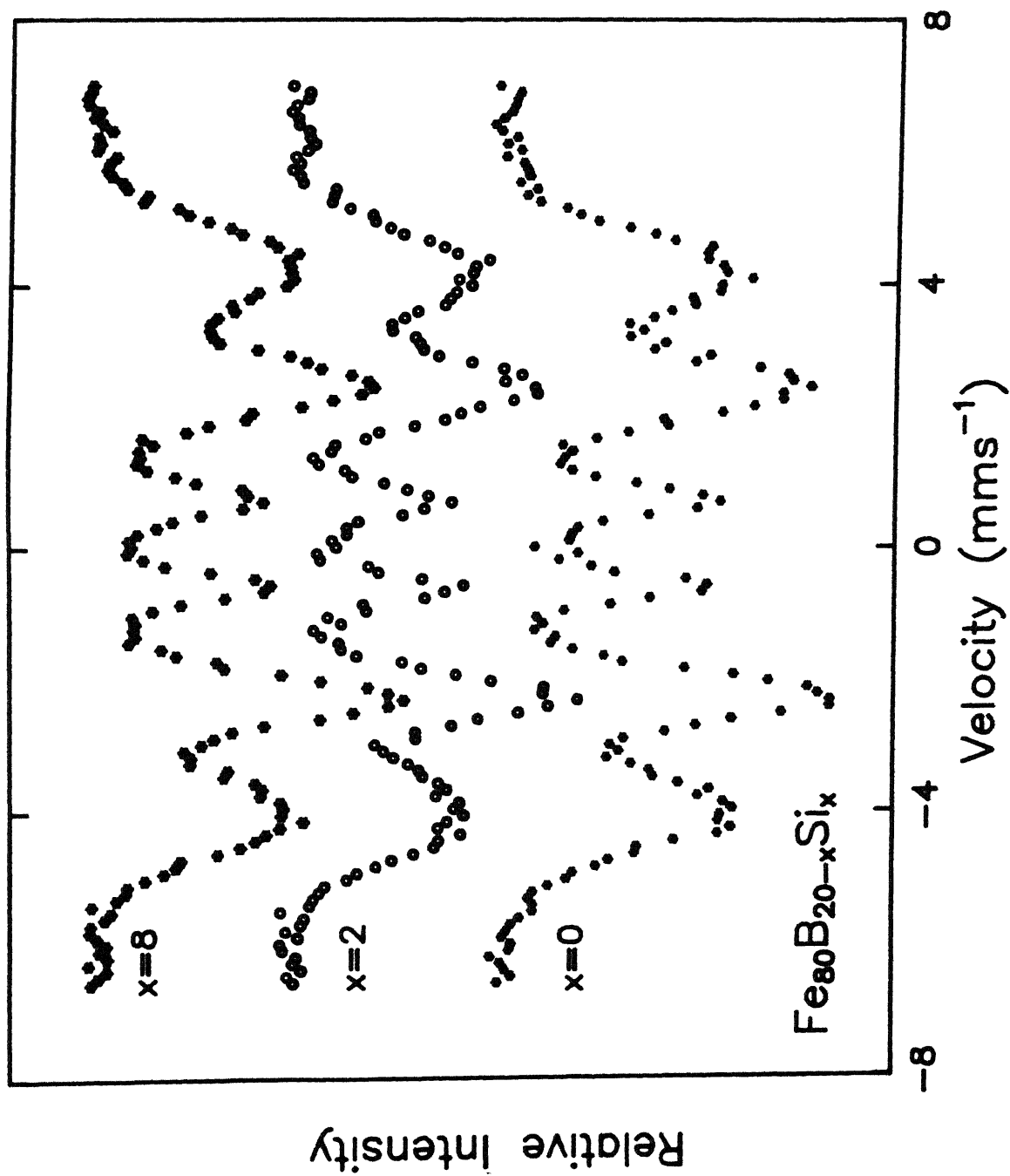


Fig. 3.17 Mössbauer spectra recorded at room temperature of as-received $\text{Fe}_{80}\text{B}_{20-x}\text{Si}_x$ ($x = 0, 2$, and 8) alloys.

the as-received $\text{Fe}_{80}\text{B}_{20-x}\text{Si}_x$ samples ($x = 0, 2$, and 8) are listed in Table 3.5.

Table 3.5

Mössbauer parameters, obtained from computer analysis, for the as-received $\text{Fe}_{80}\text{B}_{20-x}\text{Si}_x$ ($x = 0, 2$, and 8) amorphous ferromagnets.

x (at.%)	H (kOe) (a)	IS(mms^{-1}) (b)	$\Gamma(\text{FWHM})(\text{mms}^{-1})$ (c)
0	253	0.07	0.92
2	255	0.09	0.94
8	258	0.16	0.86

(a) H : Internal magnetic field at ^{57}Fe nucleus, typical error is ± 3 kOe.

(b) IS : Isomer shift w.r.t. $\alpha\text{-Fe}$, typical error is $\pm 0.01 \text{ mms}^{-1}$.

(c) $\Gamma(\text{FWHM})$: Width of the spectral line, typical error is $\pm 0.01 \text{ mms}^{-1}$.

The dependence of the isomer shift on silicon concentration (x) is shown in Fig. 3.18(a). The present results indicate that the isomer shift (IS) increases linearly with increasing silicon concentration (x). According to Walker [68], the IS increases with increasing 3d and decreasing 4s-electron numbers for the ^{57}Fe atoms (in the absorber) in Mössbauer spectroscopy. In the present case the replacement of B by Si, i.e., the addition of Si to $\text{Fe}_{80}\text{B}_{20}$ for $x = 2$ and $x = 8$ samples, causes more electrons to fill the 3d-holes of Fe through the hybridization of the 3d-orbitals of

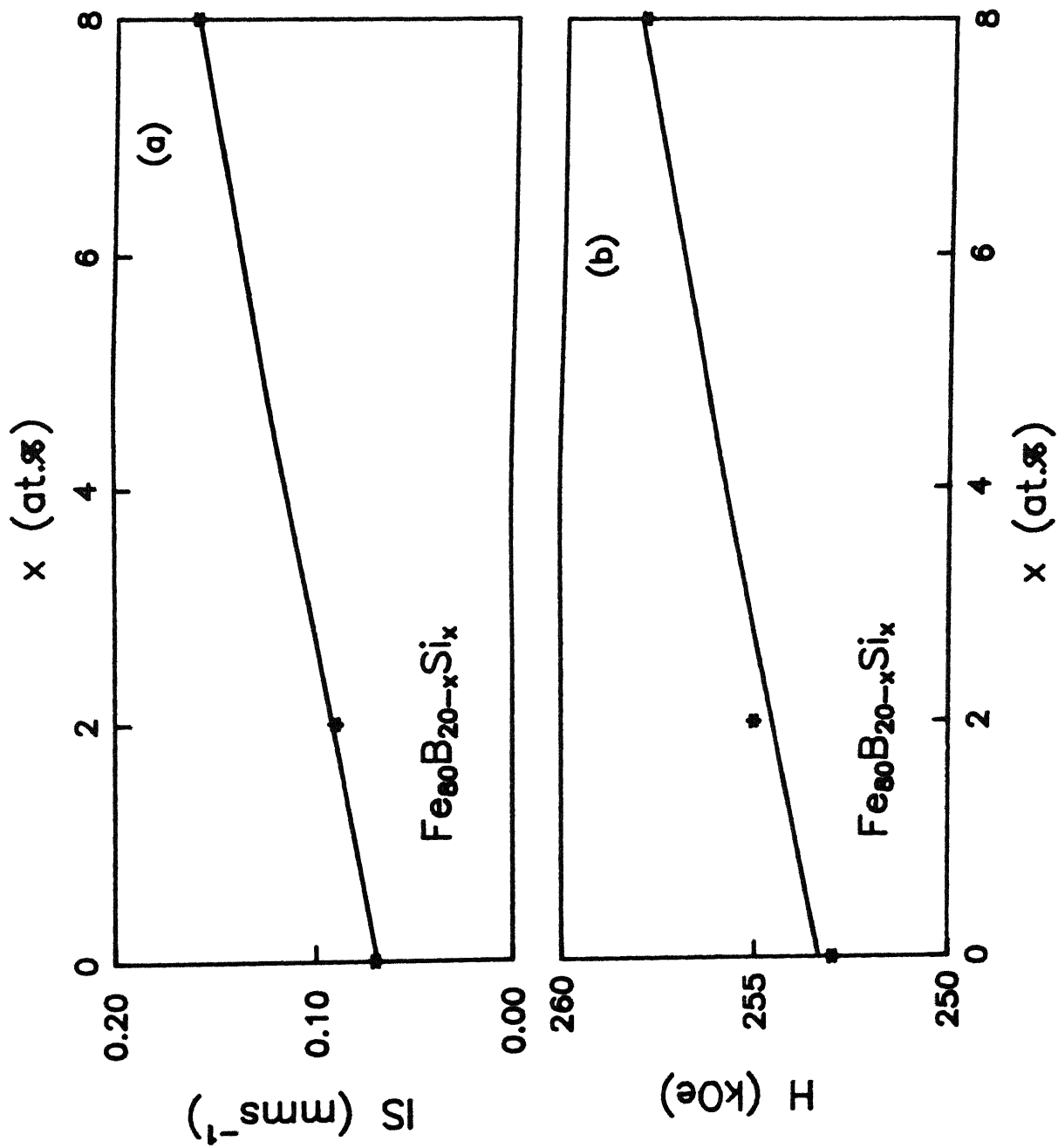


Fig. 3.18 (a) Plot of isomer shift (IS) [measured with respect to $\alpha\text{-Fe}$] versus x (b) Internal magnetic field H versus x for amorphous $\text{Fe}_{80}\text{B}_{20-x}\text{Si}_x$ ($x = 0, 2$, and 8) alloys.

Fe with s- and p-orbitals of the metalloid Si and these surplus 3d-electrons, in turn, shield more 4s-electrons thereby reducing the electron density at the nucleus. The linear dependence of IS on Si concentration is in agreement with the results of Taniwaki and Maeda [69] on Fe-B-Si alloys.

The dependence of the internal magnetic field H on x (silicon concentration) is plotted in Fig. 3.18 (b). It is seen that the observed value is $H = 253 \pm 3$ kOe for $x = 0$ and with the addition of Si, it increases slightly to $H = 258 \pm 3$ kOe for $x = 8$. Such a slight increase of H with x agrees with the observations reported by Gonser et al. [70]. These authors proposed that the slight increase in H with increasing silicon is caused by the strain caused during the replacement of a small metalloid atom by a large metalloid atom in an interstitial site. Similar behaviour of H was observed by Taniwaki and Maeda [69] for $\text{Fe}_{80}\text{B}_{20-x}\text{Si}_x$.

$x = 0$

In order to study the kinetics of crystallization in the $\text{Fe}_{80}\text{B}_{20-x}\text{Si}_x$ system, the as-received samples for $x = 0$ were heated at various temperatures for different time periods as shown below where the time period of heating is shown in parenthesis : 300°C (1 hr), 300°C (2 hr), 350°C (1 hr), 350°C (2 hr), 400°C (1 hr), and 400°C (4 hr). Mössbauer spectra of such heat-treated samples were recorded at room temperature. These spectra have been analyzed and their Mössbauer parameters are listed in Table 3.6. The spectra for the sample heated below 400°C are shown in Fig 3.19 and they typically consist of six broad lines (typical

Table 3.6

Mössbauer parameters, obtained from computer analysis, for $x = 0$ sample after various heat treatments.

Annealing Temp ($^{\circ}\text{C}$)	Annealing duration(hr)	IS (mms^{-1}) (a)	H (kOe) (b)	Γ (mms^{-1}) (c)	Remark
300	1	0.08	256	0.92	amorphous
300	2	0.07	258	0.92	amorphous
350	1	0.08	259	0.94	amorphous
350	2	0.08	260	1.0	amorphous
400	1	i) 0.00	333	0.28	$\alpha\text{-Fe}$ $\left. \begin{array}{l} \text{ii) 0.07} \\ \text{iii) 0.11} \\ \text{iv) 0.07} \end{array} \right\} \text{t-Fe}_3\text{B}$
		ii) 0.07	290	0.38	
		iii) 0.11	268	0.46	
		iv) 0.07	224	0.50	
400	4	i) 0.00	333	0.28	$\alpha\text{-Fe}$ $\left. \begin{array}{l} \text{ii) 0.10} \\ \text{iii) 0.12} \\ \text{iv) 0.07} \end{array} \right\} \text{t-Fe}_3\text{B}$
		ii) 0.10	287	0.42	
		iii) 0.12	266	0.44	
		iv) 0.07	224	0.50	

(a), (b), and (c) \rightarrow as in Table 3.5

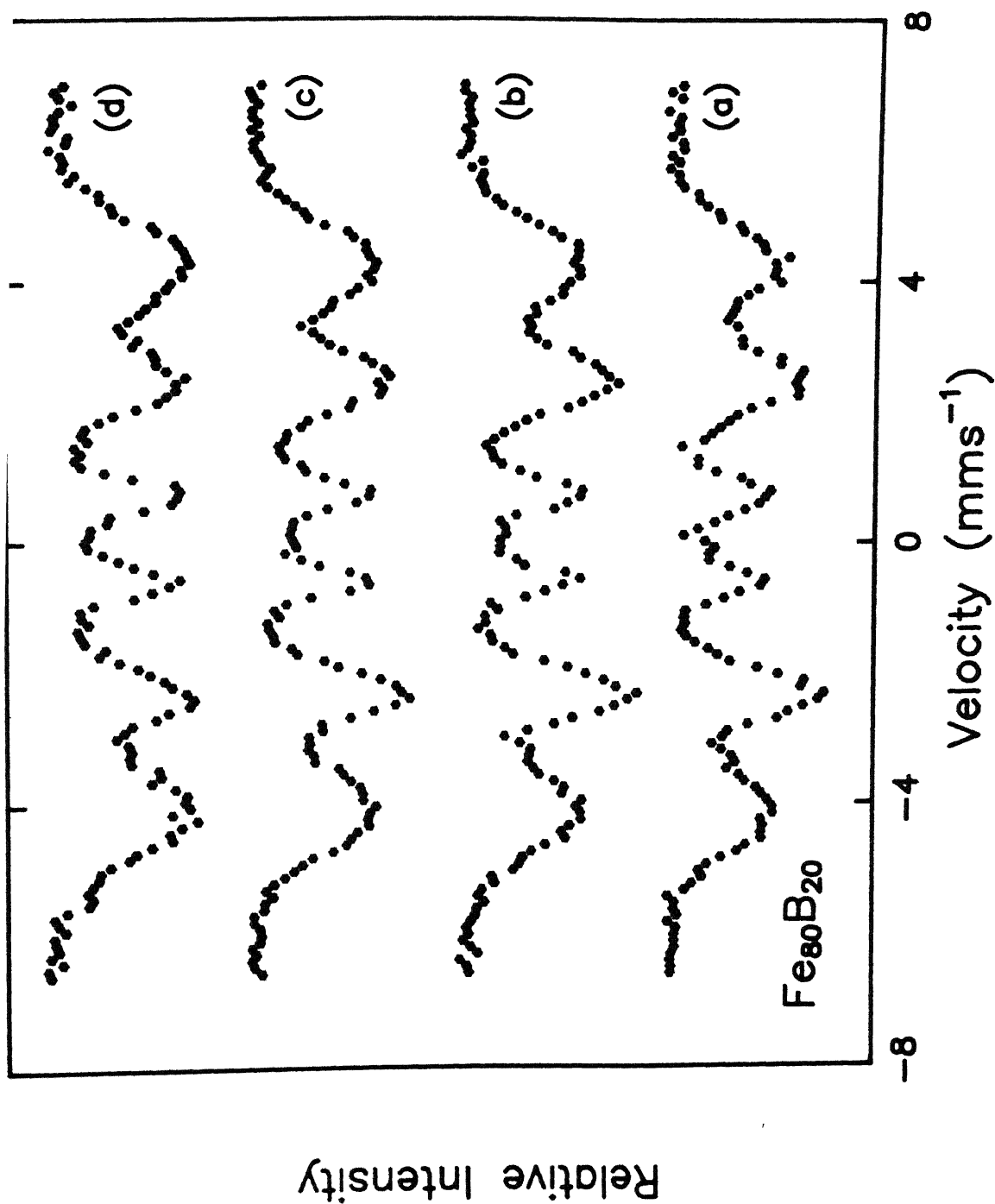


Fig. 3.19 Mössbauer spectra recorded at room temperature of $\text{Fe}_{80}\text{B}_{20}$, heat-treated at : (a) 300°C (1 hr) (b) 300°C (2 hr) (c) 350°C (1 hr) (d) 350°C (2 hr).

linewidths being $0.9 - 1.0 \text{ mms}^{-1}$). The $x = 0$, sample heat-treated at 400°C , shows a dramatic change in the nature of the Mössbauer spectrum indicating the familiar transformation from the amorphous phase to the crystalline phase. These two spectra, [400°C (1 hr) and 400°C (4 hr)] for the $x = 0$ sample, were fitted into four subspectra [Fig. 3.20] and the resulting parameters are shown in Table 3.6. These results indicate that for the $x = 0$ sample, heat-treated at 400°C (for 1 hr and 4 hr), the Mössbauer spectra are characterized by hyperfine fields in four different ranges : 333 kOe (first range), 287-290 kOe (second range) , 266-268 kOe (third range) and 224 kOe (fourth range). The first range is associated with the ^{57}Fe probes in a bcc $\alpha\text{-Fe}$ -like environment. We propose that the last three ranges are associated with the $t\text{-Fe}_3\text{B}$ phase in agreement with the observations of Caer and Dubois [71]. It may be pointed out that, in their Mössbauer study of the crystallization of $\text{Fe}_{80}\text{B}_{20}$ amorphous alloys, Sánchez et al. [72] found evidence for a mixture of tetragonal and orthorhombic Fe_3B ($t\text{-Fe}_3\text{B}$ and $o\text{-Fe}_3\text{B}$) for samples annealed at 800°C . However, in our case the X-ray diffraction studies of the samples revealed [see Table 3.7, Fig. 3.21] the presence of only $\alpha\text{-Fe}$ and $t\text{-Fe}_3\text{B}$, and there was no indication of $o\text{-Fe}_3\text{B}$. Our Mössbauer analysis shows three distinct hyperfine fields attributable to the Fe_3B phase, thus indicating at least three magnetically inequivalent sites in the crystalline Fe_3B . It is known that in the magnetically ordered state, the number of magnetically inequivalent sites could potentially be greater than (although often equal to) the number of crystallographically inequivalent sites [26]. It is further known that in the

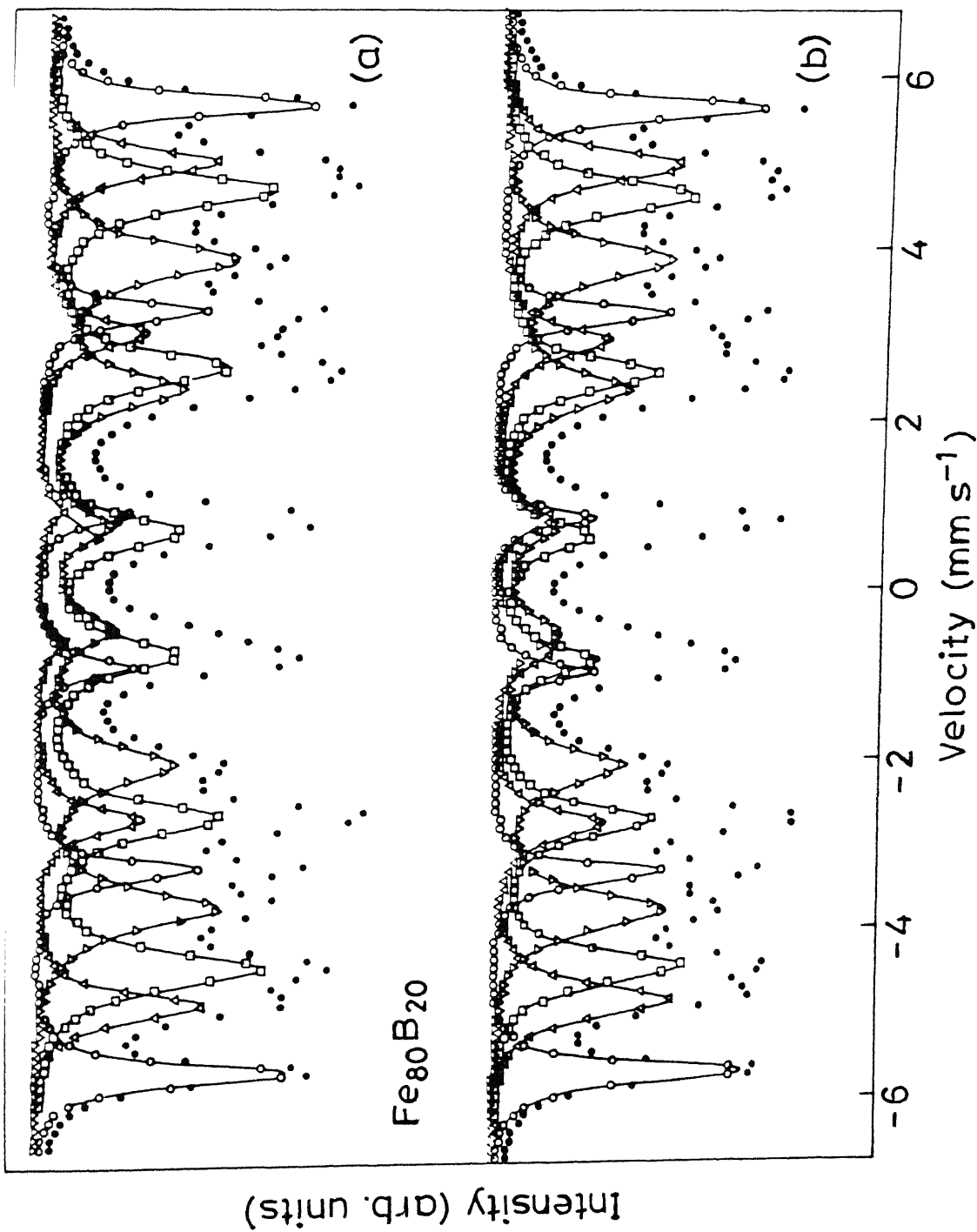


Fig. 3.20 Mössbauer spectra recorded at room temperature of $\text{Fe}_{80}\text{B}_{20}$ heat-treated at : (a) 400°C (1 hr) (b) 400°C (4 hr), fitted into four sub spectra. The symbols \bullet , \circ , Δ , \square , and ∇ refer to raw spectra, I, II, III, and IV sextet, respectively of Table 3.6.

Table 3.7

X-ray analysis of crystallized $\text{Fe}_{80}\text{B}_{20-x}\text{Si}_x$ ($x = 0, 2, \text{ and } 8$) alloys after Mössbauer measurements.

x (at.%)	Phase	d_{obs}	d_{std}^a	I_{obs}	I_{std}
0	$\alpha\text{-Fe}$	2.027	2.027	100	100
		1.43	1.433	12	20
	Fe_3B	2.088	2.088	70	100
		1.93	1.93	30	80
		1.88	1.88	40	100
		1.69	1.69	20	60
	$\alpha\text{-Fe}$	2.027	2.027	100	100
		1.431	1.433	19	20
2	Fe_3B	2.15	2.15	7	20
		2.089	2.088	70	100
		1.93	1.93	30	80
		1.88	1.88	50	100
		1.69	1.69	24	60
	$\alpha\text{-Fe}$	2.027	2.027	100	100
		1.431	1.433	19	20
8	Fe_3B	N.P.	-	-	-
	Fe_2B	2.01	2.01	30	100
		1.63	1.63	15	18

N.P : Not Present, ^aReference 64.

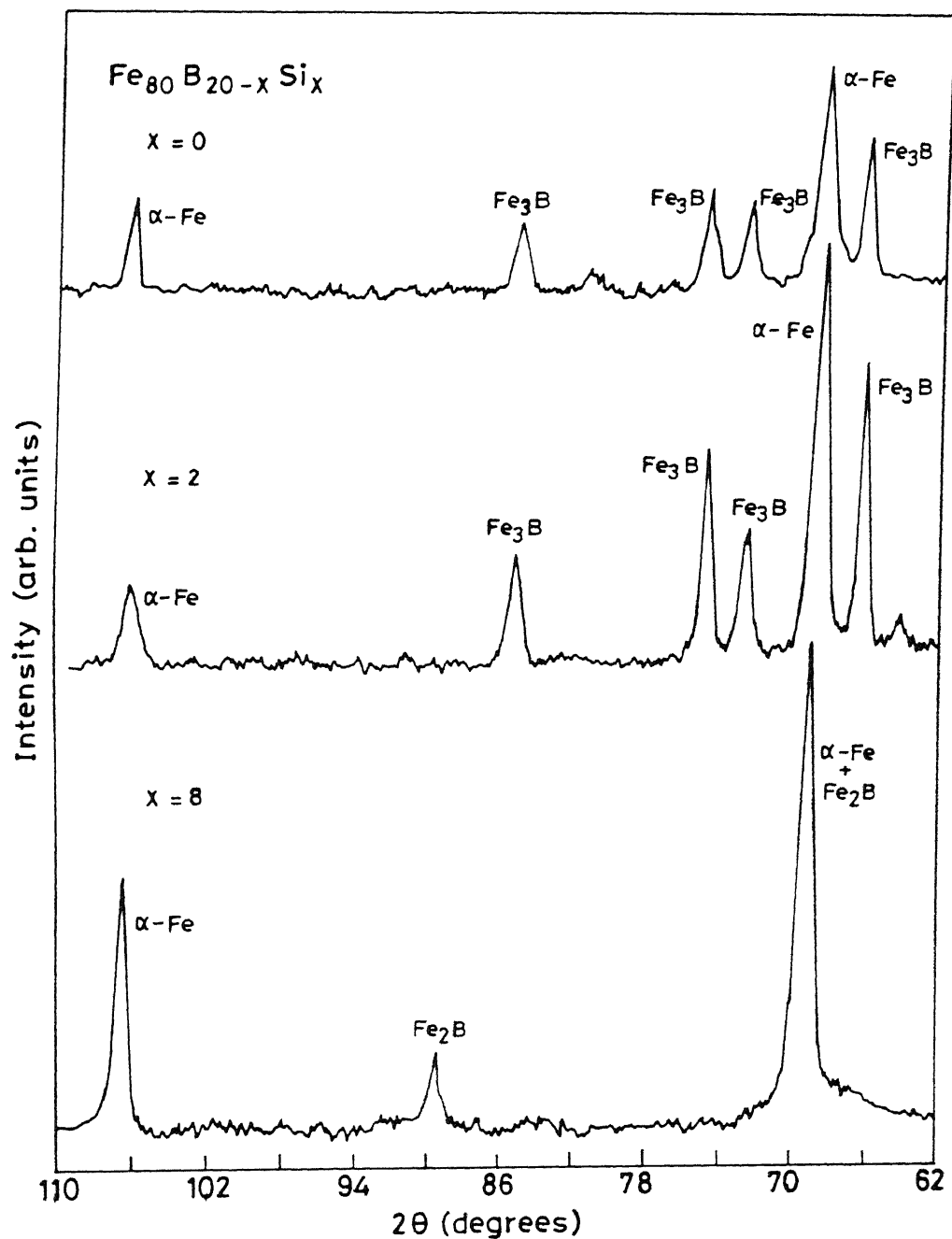


Fig. 3.21 X-ray diffraction pattern at room temperature, of $\text{Fe}_{80}\text{B}_{20-x}\text{Si}_x$, with $x = 0$ annealed at 400°C (4 hr), $x = 2$ at 475°C (4 hr), and $x = 8$ at 525°C (4 hr) after Mössbauer measurements.

orthorhombic structure, there are two crystallographically inequivalent Fe sites with an Fe ratio 2:1 while in the tetragonal structure there are three crystallographically inequivalent sites with a site ratio of 1:1 [26].

As pointed out by Chien et al. [26], from their studies of the magnetic properties of amorphous $\text{Fe}_x\text{B}_{100-x}$ ($72 \leq x \leq 86$) and crystalline Fe_3B , the possible magnetic phases that can precipitate from the system $\text{Fe}_{80}\text{B}_{20}$ after crystallization are FeB , Fe_2B , Fe_3B and $\alpha\text{-Fe}$. Out of these, the crystalline phase of FeB never occurs after crystallization of amorphous $\text{Fe}_{80}\text{B}_{20}$ [25]. In our case, the $x = 0$ sample, heat-treated at 400°C indicates the presence of $\alpha\text{-Fe}$ and $t\text{-Fe}_3\text{B}$ while the presence of Fe_2B or $o\text{-Fe}_3\text{B}$ are not supported by the analysis of our X-ray diffraction, thermomagnetic study, and Mössbauer spectra. The precipitated Fe_3B is not a stable phase but it is a metastable one [22,28] which can decompose at higher temperatures. The possible decomposition of Fe_3B into Fe_2B and $\alpha\text{-Fe}$ can occur only at temperatures much above 400°C and hence it was not observed by us. In the high-temperature magnetization study, the sample with $x = 0$ was heated up to 700°C but we did not observe the decomposition of Fe_3B into $\alpha\text{-Fe}$ and Fe_2B . In this respect our results are in agreement with those observed by Chien et al. [26], Sánchez et al [72] and Schaafsma [24]. It may further be added that our results indicate that the intensities of $\alpha\text{-Fe}$ and Fe_3B to be 24% and 76% in the spectrum of 400°C (4 hr) sample.

$x = 2$

The sample of $\text{Fe}_{80}\text{B}_{20-x}\text{Si}_x$ ($x = 2$) was studied by

Mössbauer spectroscopy and X-ray diffraction techniques. This $x = 2$ sample was heat-treated at 300°C (1 hr), 300°C (2 hr), 350°C (1 hr), 350°C (2 hr), 400°C (1 hr), 400°C (2 hr), 475°C (1 hr), and 475°C (4 hr). The Mössbauer spectra of these, recorded at room temperature, are shown in Fig. 3.22 while the computer-fitted spectra are shown in Fig. 3.23 for the 475°C (1 hr) and 475°C (4hr) sample. The Mössbauer parameters, obtained from computer analysis, are given in Table 3.8. An immediate observation, made from Table 3.6, is that compared to the $x = 0$ sample, the crystallization starts at a higher (475°C) temperature. This result suggests that the thermal stability of $\text{Fe}_{80}\text{B}_{18}\text{Si}_2$ increases with the addition of Si. An analysis of the Mössbauer spectra shows that $\alpha\text{-Fe}$ and Fe_3B phases crystallize in the sample heat-treated at 475°C (1 hr) and 475°C (4 hr) with three distinct hyperfine fields for the Fe_3B phases. The values of the internal magnetic field, obtained for the Fe_3B phase for the $x = 2$ sample, support the assignment of the tetragonal ($t\text{-Fe}_3\text{B}$) phase (Table 3.8). This conclusion is confirmed by the X-ray diffraction studies (Table 3.7 and Fig. 3.21). The relative intensities of the $\alpha\text{-Fe}$ and $t\text{-Fe}_3\text{B}$ phases, observed by us for the $x = 2$ sample, are 20% and 80% respectively and thus these intensities do not show much change from the values observed for the $x = 0$ sample.

$x = 8$

The sample of $\text{Fe}_{80}\text{B}_{12}\text{Si}_8$ ($x = 8$) was given heat-treatment at the following temperatures 300°C (1 hr), 300°C (2 hr), 350°C (1 hr), 350°C (2 hr), 400°C (1 hr), 400°C (2 hr), 475°C

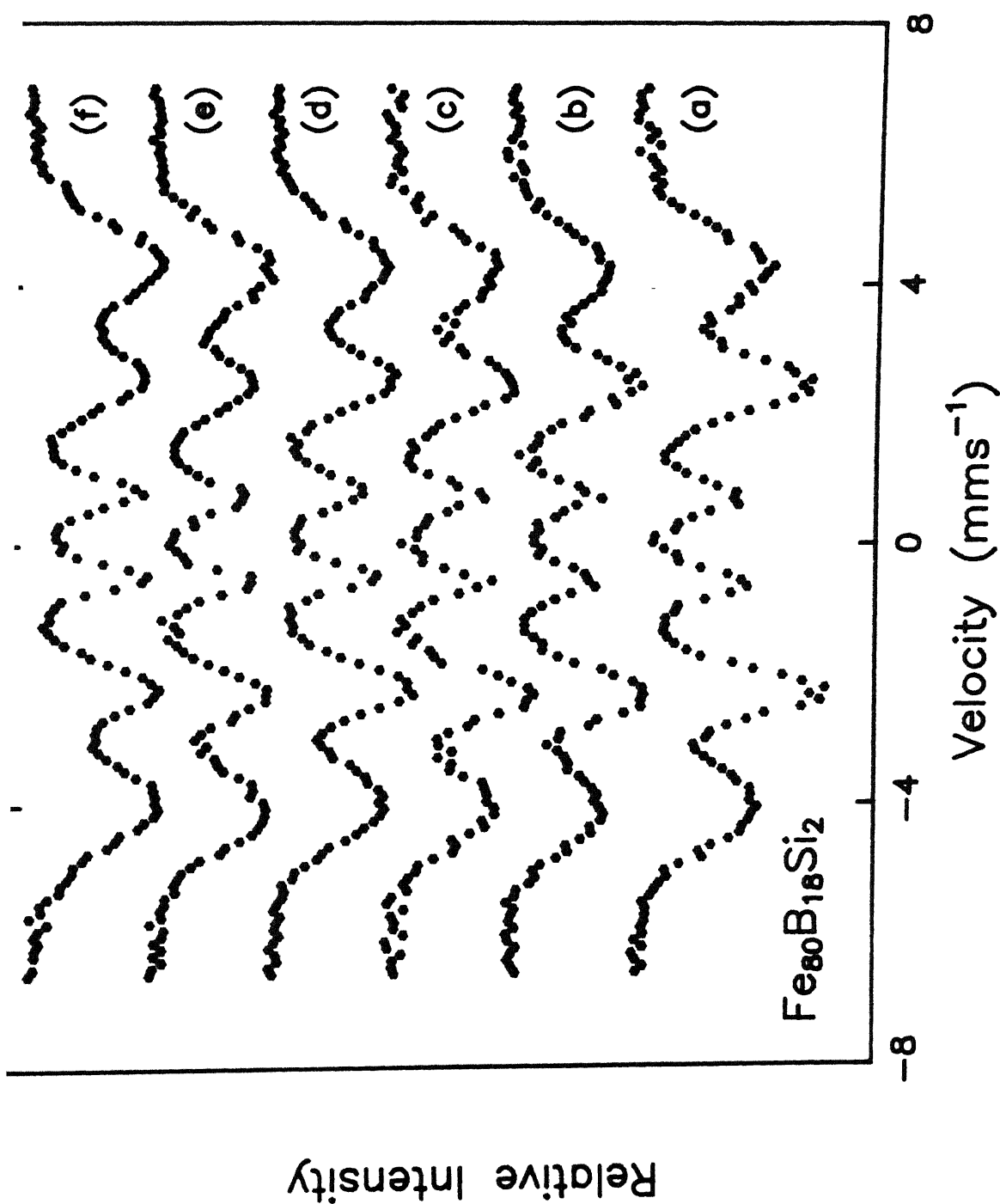


Fig. 3.22 Mössbauer spectra recorded at room temperature of $\text{Fe}_{80}\text{B}_{18}\text{Si}_2$, heat-treated at : (a) 300°C (1 hr) (b) 300°C (2 hr) (c) 350°C (1 hr) (d) 350°C (2 hr) (e) 400°C (1 hr) (f) 400°C (2 hr).

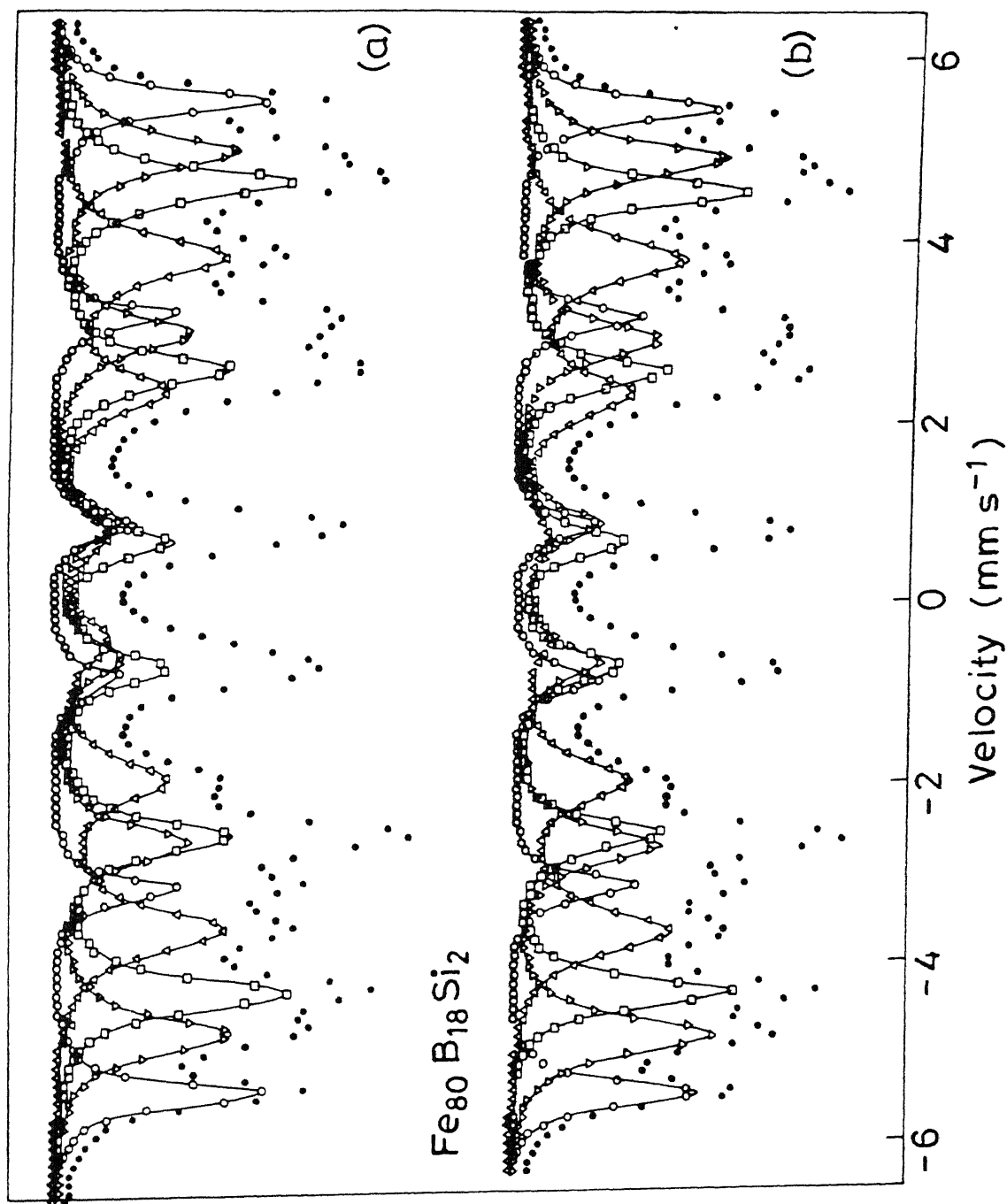


Fig. 3.23 Mössbauer spectra recorded at room temperature of $\text{Fe}_{80}\text{B}_{18}\text{Si}_2$, heat-treated at : (a) 475°C (1 hr) (b) 475°C (4 hr), fitted into four sub spectra. The symbols \bullet , \circ , Δ , \square , and ∇ refer to raw spectra, I, II, III, and IV sextet, respectively of Table 3.8.

Table 3.8

Mössbauer parameters, obtained from computer analysis, for $x = 2$ sample after various heat treatments.

Annealing Temp ($^{\circ}\text{C}$)	Annealing duration(hr)	IS (mms^{-1}) (a)	H (kOe) (b)	Γ (mms^{-1}) (c)	Remark
300	1	0.10	256	0.92	amorphous
300	2	0.07	259	0.92	amorphous
350	1	0.09	259	0.90	amorphous
350	2	0.07	258	0.92	amorphous
400	1	0.06	260	0.96	amorphous
400	2	0.07	260	1.00	amorphous
475	1	i) 0.02	332	0.33	$\alpha\text{-Fe}$ $\left. \begin{array}{l} \text{ii) 0.07} \\ \text{iii) 0.13} \\ \text{iv) 0.08} \end{array} \right\} \text{t-Fe}_3\text{B}$
		ii) 0.07	296	0.52	
		iii) 0.13	271	0.42	
		iv) 0.08	225	0.62	
475	4	i) 0.00	333	0.34	$\alpha\text{-Fe}$ $\left. \begin{array}{l} \text{ii) 0.06} \\ \text{iii) 0.12} \\ \text{iv) 0.08} \end{array} \right\} \text{t-Fe}_3\text{B}$
		ii) 0.06	297	0.46	
		iii) 0.12	271	0.38	
		iv) 0.08	227	0.60	

(a), (b), and (c) \rightarrow as in Table 3.5

(1 hr), 475°C (2 hr), 525°C (1 hr), and 525°C (4 hr). Mössbauer spectra for these, recorded at room temperature, are shown in Fig. 3.24 and 3.25 while their Mössbauer parameters, obtained by computer analysis, are given in Table 3.9. In the case of the $x = 2$ sample, the crystallization of $\text{Fe}_{80}\text{B}_{18}\text{Si}_2$ was complete at 475°C. It is evident also from the high-temperature magnetization study for $x = 2$ that the crystallization starts at about 442°C. However, the Mössbauer spectra for the $x = 8$ sample, heat-treated at 475°C for 1 hr, does not show any clear precipitation (Fig. 3.25). The peaks for the α -Fe phase appear to overlap with those due to the amorphous phase while another new phase appears to precipitate. The computer analysis of the sample ($x = 8$), heat-treated at 475°C for 4 hr, when fitted into two subspectra, yielded two values of the internal magnetic field i) $H \simeq 316$ kOe and ii) $H \simeq 240$ kOe (Table 3.9). This computer analysis was complicated due to the partial crystallization which left some material still in the amorphous phase and made the fit rather difficult. The observed value of $H \simeq 316$ kOe is assigned to α -Fe and it is lower than the standard value of $H \simeq 330$ kOe for α -Fe because of the presence of the amorphous phase in small amount. The other subspectra observed by us yielded $H \simeq 240$ kOe and $IS = 0.15 \text{ mms}^{-1}$ and we ascribe it to Fe_2B , based on the findings of Takács et al. [73] who observed the Mössbauer spectra from crystalline Fe_2B and have obtained an average value of $H = 236.9$ kOe and $IS = 0.12 \text{ mms}^{-1}$. Actually, Takács et al. [73] observed two subspectra corresponding to the two iron sites in Fe_2B whose H -values were very close, i.e., at 242 and 231.7 kOe. In our case we could not resolve these two sites, most probably because of the

Relative Intensity

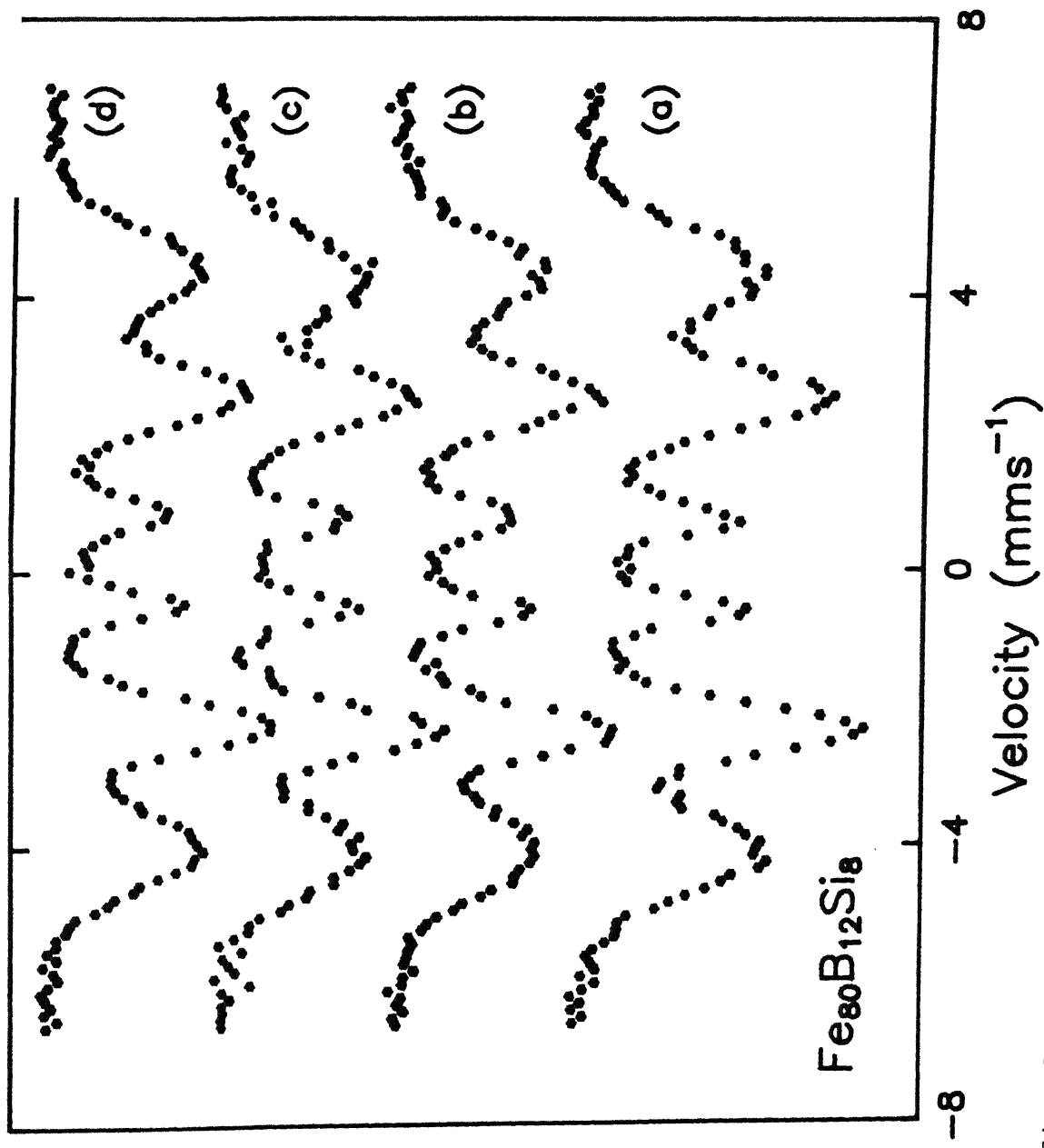


Fig. 3.24 Mössbauer spectra recorded at room temperature of $\text{Fe}_{80}\text{B}_{12}\text{Si}_8$, heat-treated at : (a) 300°C (1 hr) (b) 300°C (2 hr) (c) 350°C (1 hr) (d) 350°C (2 hr).

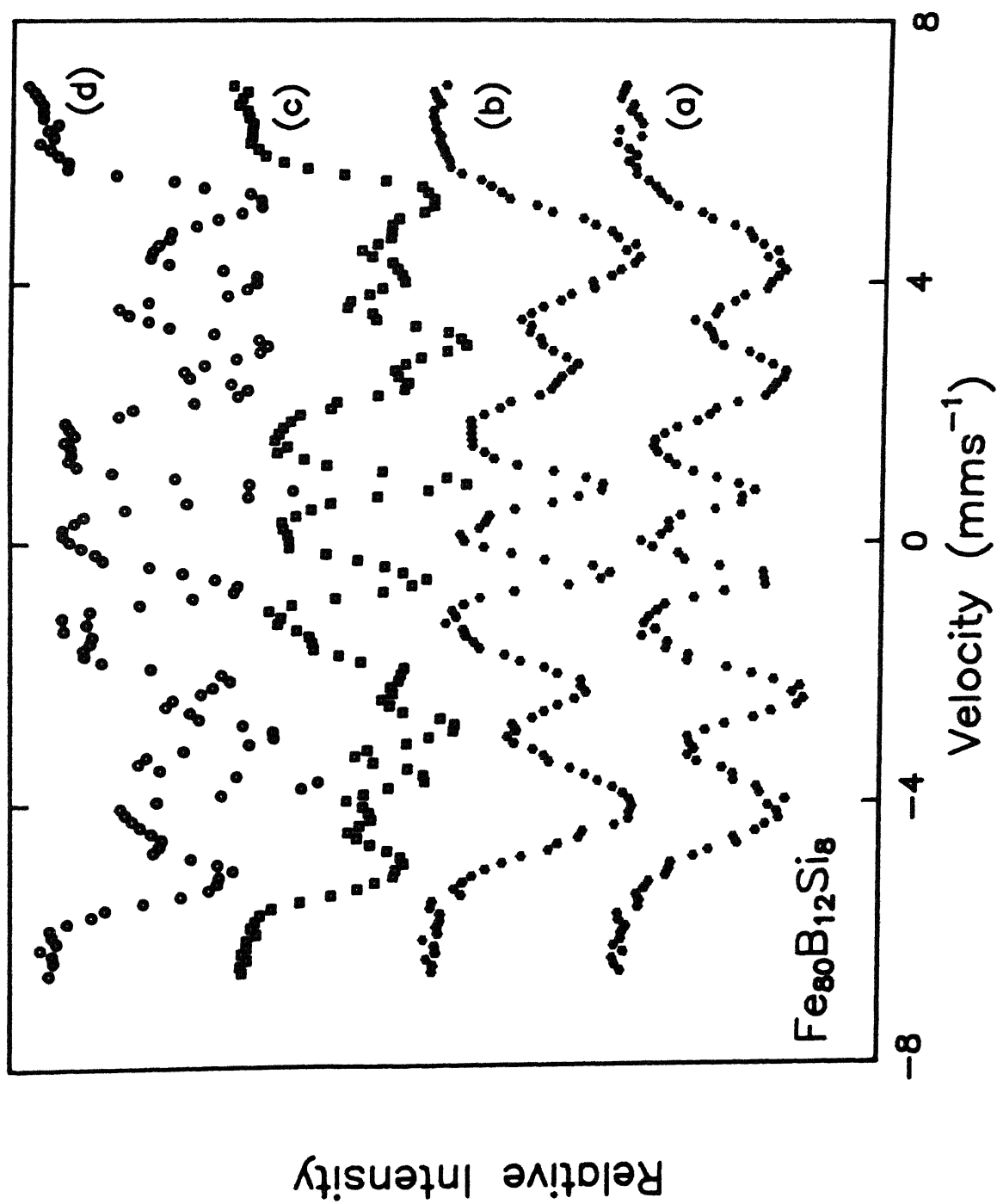


Fig. 3.25 Mössbauer spectra recorded at room temperature of $\text{Fe}_{80}\text{B}_{12}\text{Si}_8$, heat-treated at : (a) 400°C (1 hr) (b) 400°C (2 hr) (c) 475°C (1 hr) (d) 475°C (4 hr).

Table 3.9

Mössbauer parameters, obtained from computer analysis, for x = 8 sample after various heat treatments.

Annealing Temp ($^{\circ}\text{C}$)	Annealing duration(hr)	IS (mms^{-1}) (a)	H (kOe) (b)	Γ (mms^{-1}) (c)	Remark
300	1	0.13	261	0.93	amorphous
300	2	0.11	263	0.90	amorphous
350	1	0.09	262	0.88	amorphous
350	2	0.10	262	0.88	amorphous
400	1	0.07	263	0.94	amorphous
400	2	0.08	264	1.02	amorphous
475	1	i) 0.05	316	0.66	partially crystallised, α -Fe overlapped with amorphous phase
		ii) 0.15	241	0.40	Fe_2B
475	4	i) 0.05	317	0.68	partially crystallised, α -Fe overlapped with amorphous phase
		ii) 0.15	240	0.40	Fe_2B
525	1	Model A			
		i) 0.06	315	0.66	α -Fe
		ii) 0.14	238	0.38	Fe_2B
		Model B			
		i) 0.06	322	0.48	α -Fe
		ii) 0.05	295	0.74	FeSi
		iii) 0.14	237	0.42	Fe_2B
525	4	Model A			
		i) 0.04	314	0.66	α -Fe
		ii) 0.14	239	0.38	Fe_2B
		Model B			
		i) 0.01	327	0.30	α -Fe
		ii) 0.05	309	0.42] FeSi
		iii) 0.10	281	0.40	
		iv) 0.15	238	0.42	

(a), (b), and (c) \rightarrow as in Table 3.5

presence of the amorphous phase. It is also observed from our high-temperature magnetization studies that the crystallized phases are α -Fe and Fe_2B .

In order to study the crystallization of $\text{Fe}_{80}\text{B}_{12}\text{Si}_8$ in more detail we have heat-treated the $x = 8$ sample at 525°C for 1 hr and 4 hr respectively. The Mössbauer spectra of these two were recorded at room temperature and they are shown in Figs. 3.26 and 3.27 in the as-recorded form as well as in the form obtained by computer fitting. In the case of these sample the computer analysis was carried out in the following two ways :

- i) Model A : In this model it was assumed that there are two subspectra arising out of α -Fe and Fe_2B phases.
- ii) Model B : In this model it was assumed that there are more than two subspectra arising out of α -Fe, Fe_2B and Fe-Si alloy system.

The Mössbauer parameters, obtained from such a computer analysis, are shown in Table 3.9. The use of model B was felt necessary because some authors have observed Fe-Si alloy phase during the crystallization of the heat-treated sample of Fe-B-Si system. The crystallization process in the metallic glass $\text{Fe}_{83}\text{B}_{12}\text{Si}_5$ has been studied with Mössbauer spectroscopy by Nowik et al. [74] who found that the final products of crystallization occurring above 500°C were α -Fe, Fe_2B , and Fe-Si. The α -Fe and Fe_2B phases showed well-defined magnetic hyperfine fields at two sites while the Fe-Si showed a pure quadrupole-split subspectrum. The relative abundance of Fe-Si, observed by these authors, was about 6%. This could be barely observed by X-ray diffraction. Ok and Morrish [20] have studied the amorphous-to-crystalline

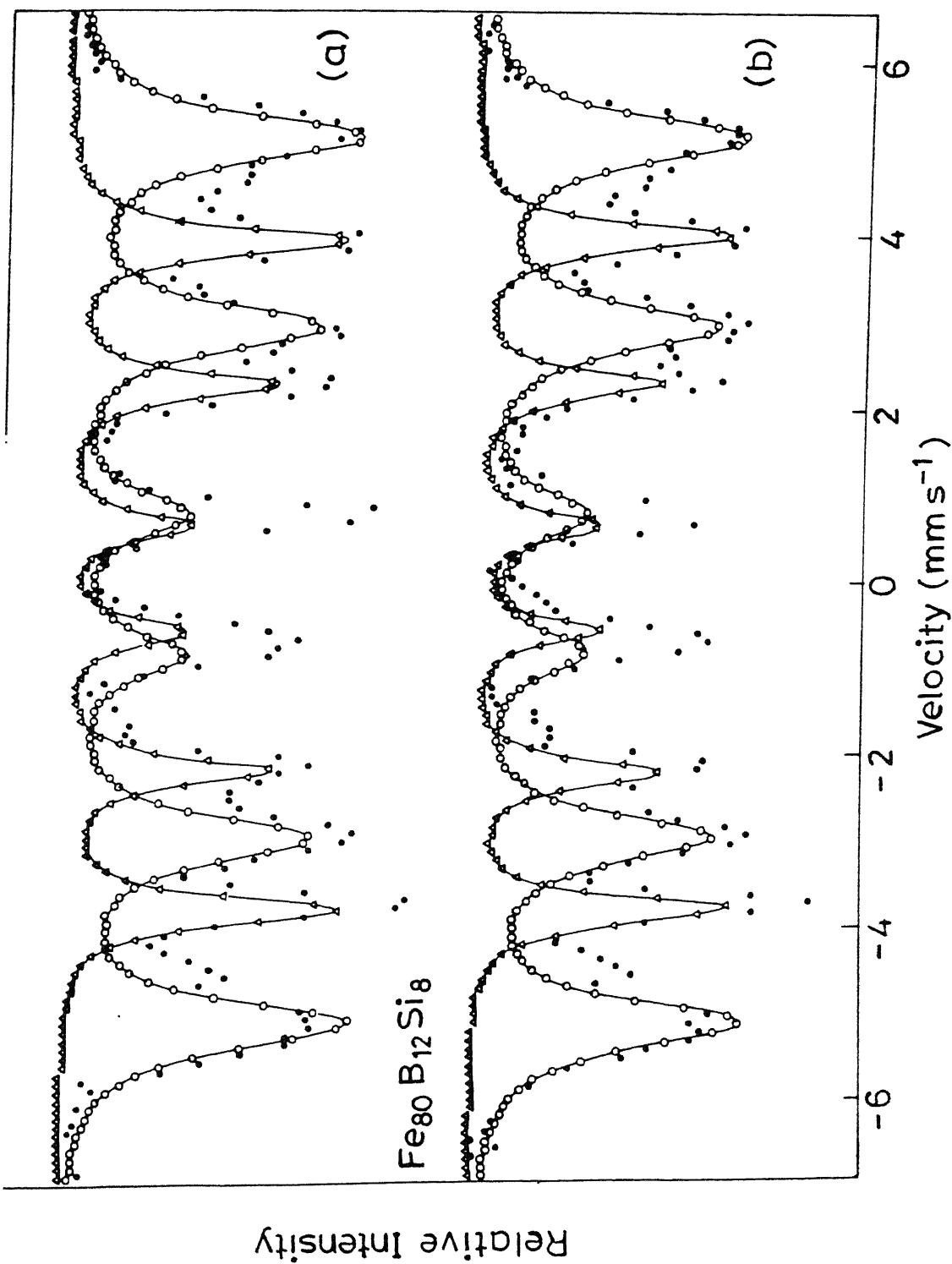


Fig. 3.26 Mössbauer spectra recorded at room temperature of $\text{Fe}_{80}\text{B}_{12}\text{Si}_8$, heat-treated at : (a) 525°C (1 hr) (b) 525°C (4 hr), fitted using model A. The symbols ●, ○, and Δ refer to raw spectra, I, and II sextet, respectively of Table 3.9.

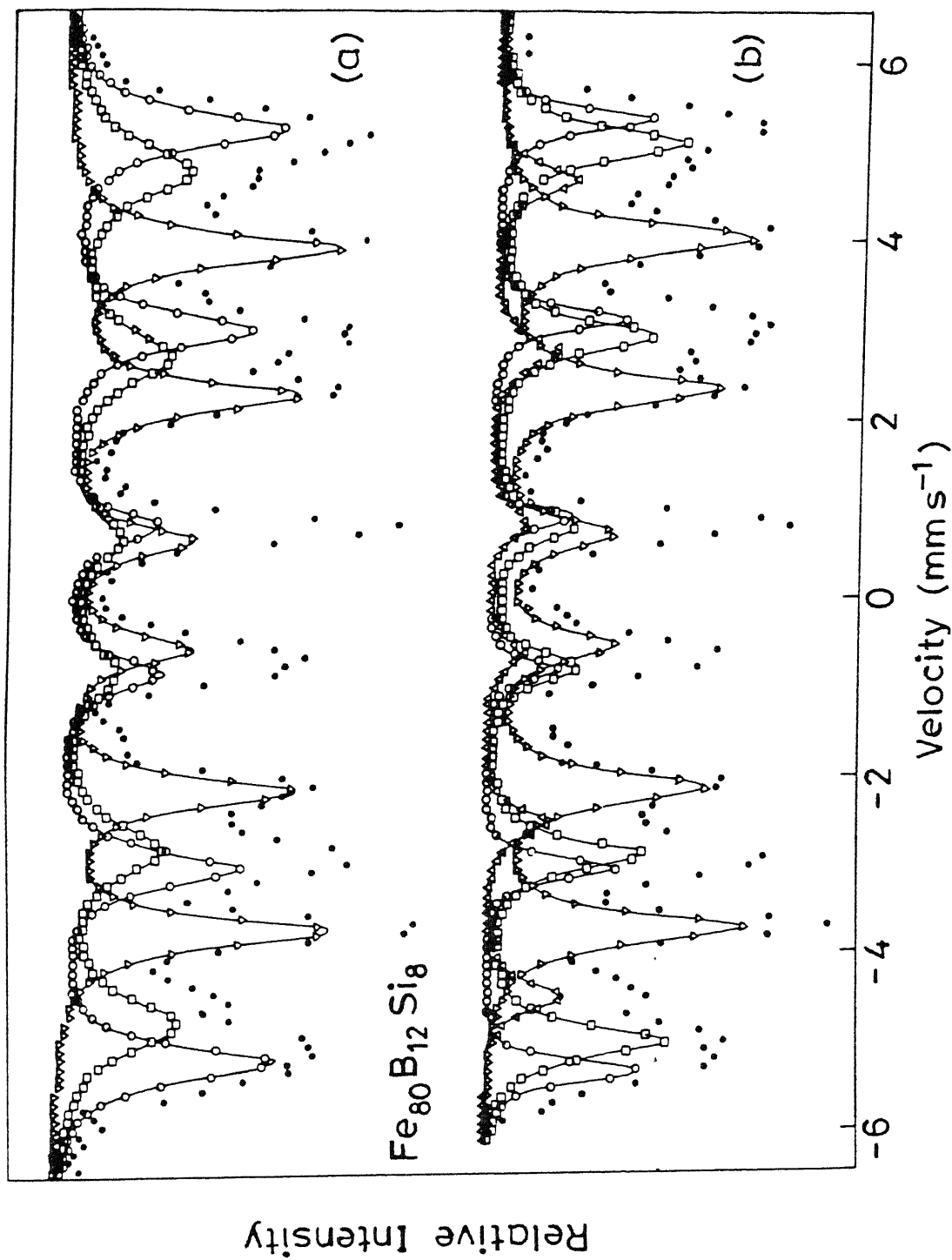


Fig. 3.27 Mössbauer spectra recorded at room temperature of $\text{Fe}_{80}\text{B}_{12}\text{Si}_8$, heat-treated at : (a) 525°C (1 hr) (b) 525°C (4 hr), fitted using model B. The symbols ●, ○, ▲, △, ■, and ▼ refer to raw spectra, I, II, III, and IV sextet, respectively of Table 3.9.

transformation of $\text{Fe}_{82}\text{B}_{12}\text{Si}_6$ by Mössbauer spectroscopy, X-ray diffraction and density measurements. These authors found that the heat treatment of $\text{Fe}_{82}\text{B}_{12}\text{Si}_6$ led to a transformation involving several steps and the final products of the transformation did not consist of $\alpha\text{-Fe}$ but consisted of Fe-9 at.% Si alloy and Fe_2B while we observed from the high-temperature magnetization study that the crystallization is a two-step process. Similarly Ok et al. [30] found that the final products of the crystallization of amorphous $\text{Fe}_{75.4}\text{B}_{14.2}\text{Si}_{10.4}$ were Fe-18.1 at.% Si alloy and Fe_2B . Nagarajan et al. [31] studied the crystallization of $\text{Fe}_{78}\text{B}_{13}\text{Si}_9$ by Mössbauer spectroscopy and X-ray diffraction and concluded that Fe-15.8 at.% Si and Fe_2B were the final crystalline products of this system.

The present results (Table 3.9) for the Mössbauer parameters for the 525°C (1 hr) and 525°C (4 hr), using model A, show the clear presence of $\alpha\text{-Fe}$ and Fe_2B phases with the observed H-value ($H = 238$ and 239 kOe) agreeing with the value $H = 236.9$ kOe reported by Takács et al. [73] for Fe_2B [Fig. 3.26]. The analysis, using model B, suggests the presence of Fe-Si alloy with $H = 295$ kOe occurring at one Fe-Site for the 525°C (1 hr) sample and with $H = 309$ and 281 kOe occurring at two sites for the 525°C (4 hr) sample [Fig. 3.27]. This assignment of Fe-Si alloy phase is based on the results of other authors [20, 30, 31, 75]. It is well-known that the hyperfine fields (values of H) in the Fe-Si solid solution depend on the nearest-neighbour distributions [31, 75]. Thus, for example, the investigation of Fe-6.7 at.% Si by Häggström et al. [75] resulted in $H = 333.1$, 309.2 , and 282.4 kOe for the 8 Fe NN, 7 Fe NN, and 6 Fe NN sites respectively. In

order to resolve the choice between models A and B, we examined the results for the sample heat-treated at 525°C (4 hr), obtained by the X-ray diffraction and high-temperature magnetization studies. The X-ray diffraction studies (Table 3.7, Fig. 3.21) did not bring out the presence of the Fe-Si phase but this result could be due to a rather small amount of precipitation of the Fe-Si phase.

Further, it can be concluded that the addition of Si inhibits the formation of the metastable phase Fe_3B . It is also apparent that the addition of Si increases the crystallization temperature implying an improvement in the thermal stability. It is observed from our Mössbauer studies that $x = 0, 2, \text{ and } 8$ sample, when annealed at various temperatures, show a slight increase in the value of H (internal magnetic field). The atomic arrangements become more ordered with annealing. This increase of atomic ordering can strengthen the long-range exchange interactions responsible for the ferromagnetism of these alloys [20]. This might explain the slight increase in the value of H .

In view of these results it is difficult to make a clear choice between models A and B used by us. More experimental studies of the $\text{Fe}_{80}\text{B}_{12}\text{Si}_8$ system are necessary to determine whether Fe-Si alloy is precipitated at all and, if so, at what Fe NN sites.

CHAPTER IV

CONCLUSIONS

Our quantitative analysis of the electrical resistivity data in $\text{Fe}_{80}\text{B}_{20-x}\text{Si}_x$ ($x = 0-12$) ferromagnets shows conclusively that the inclusion of a magnetic term at all temperatures improves the χ^2 -value by an order of magnitude as compared to that when only structural terms are considered. If the data are interpreted in terms of a magnetic term proportional to T^2 , the coefficients of the various terms agree quantitatively with those of Kaul et al. [8] in a similar system, viz., $\text{Fe}_{80}\text{B}_{20-x}\text{C}_x$ ($x = 0-10$) and yield realistic Debye temperatures of $(330 \pm 40)\text{K}$. However, we find that there is a much better fit, for $T \ll \theta_D$, if the magnetic term is taken to be proportional to $T^{3/2}$, as predicted by Richter et al. [4], except for the disturbing fact that the resulting θ_D has a wide range of values in this series. A possible explanation is offered in term of the applicability of the theory of Richter et al. [4] wherein Eq.(1.6) may not satisfy the condition $T \ll T_C$ for $T \geq \theta_D$. For $T \geq \theta_D$, it is difficult to distinguish between the $T^{3/2}$ and T^2 terms, both giving equally good fit compared to that without any magnetic contribution. It is therefore safe to conclude that the magnetic contribution, at least at low temperatures ($T \ll \theta_D$), is through a $T^{3/2}$ term which is theoretically the leading term [4].

The temperature dependence of electrical resistivity in the presence of a magnetic field is still described by the same set of equations as in the zero-field case. However, the

coefficient of the magnetic term decreases somewhat with increasing field at lower temperatures while remaining constant with increasing field at higher temperatures. The magnetoresistance measurements up to 16.5 kOe, at several constant temperatures (10-300 K), show a positive ferromagnetic anisotropy of resistivity in these amorphous ferromagnets, very similar to the crystalline case. It has been observed that the FAR is not much influenced by the replacement of B by Si. The FAR decreases with increasing temperature as expected in a ferromagnet. The possible explanation for the temperature dependence of FAR is given on the basis of the model proposed by Campbell et al. [19]. These alloys are on the verge of becoming strong ferromagnets. Moreover, it has also been observed that the addition of Si does not change the special orientation of magnetization \vec{M} , i.e., \vec{M} lies in the plane of the ribbon and makes an angle of $\approx 35^\circ$ with the ribbon axis. At higher fields (≥ 2 kOe), the magnetoresistance is very small and negative for both orientations at all temperatures as expected from the localized as well as the band model. The FAR versus temperature plot for $x = 0$ roughly follows the linear magnetostriction coefficient λ_s versus temperature plot as the origin of the two lies in the spin-orbit interaction.

From our low-temperature magnetization studies, it is clear that the replacement of B by Si does not change the magnetic properties (within the experimental error). The values of the spin-wave stiffness constant D do not show any specific trend with the variation of Si while the replacement of B by C increases D ,

as observed by Majumdar et al. [32].

It is evident from our high-temperature magnetization studies that the thermal stability of $\text{Fe}_{80}\text{B}_{20}$ has increased with the addition of Si. The effect of the addition of Si ($x \geq 4$) is to render the crystallization process to occur in two steps instead of one and helps the metastable Fe_3B phase to decompose into the stable $\alpha\text{-Fe}$ as well as the Fe_2B phases. The predictions about the precipitated crystalline phases from these studies are confirmed by X-ray diffraction work.

From our Mössbauer studies of samples (as-received) with $x = 0, 2$, and 8 , it has been observed that the addition of Si increases the internal magnetic field slightly. The increase of the isomer shift on Si addition is explained in terms of the charge-transfer model. From the Mössbauer studies of the heat-treated samples, it is evident that for samples with $x = 0$ and 2 , the final crystallized phases are $\alpha\text{-Fe}$ as well as $t\text{-Fe}_3\text{B}$. These phases are also identified by X-ray diffraction studies. However, for $x = 8$, the final crystallized phases are $\alpha\text{-Fe}$, Fe_2B instead of Fe_3B , and Fe-Si (probably). It is also evident from these studies that the addition of Si increases the crystallization temperature. Thus we find that the high-temperature magnetization and Mössbauer studies give very similar conclusions about the process of crystallization and the final crystallized phases.

The origin of resistivity minima in metallic glasses is still an open question. The $\rho(T)$ data in the zero-field case as well as in the presence of external magnetic fields should be

extended down to 1 K for this investigation. With the help of more sensitive and sophisticated instruments like SQUID magnetometer or Faraday Balance, the higher order terms, viz., $T^{5/2}$, $T^{7/2}$, T^4 , etc., could be detected in the low-temperature magnetization studies.

REFERENCES

1. A.I. Gubanov, Fiz. Tver, Tel., 2, 502 (1960).
2. N. Banerjee, R. Roy, A.K. Majumdar, and R. Hasegawa, Phys. Rev. B 24, 6801 (1981); R. Roy and A.K. Majumdar, *ibid.* 31, 2033 (1985).
3. S.R. Nagel and J. Tauc, Phys. Rev. Lett. 35, 380 (1975).
4. R. Richter, M. Wolf, and F. Goedsche, Phys. Status Solidi B95, 473 (1979).
5. Béla Vasvári, Physica B159, 79 (1989).
6. G. Bergmann and P. Marquardt, Phys. Rev. B 17, 1355 (1978).
7. G. Thummes, J. Kötzler, R. Ranganathan, and R. Krishnan, Z. Phys. B 69, 489 (1988).
8. S.N. Kaul, W.H. Kettler, and M. Rosenberg, Phys. Rev. B 33, 4987 (1986).
9. E. Babic, Z. Marohnic, M. Ocko, A Hamzic, K. Saub, and B. Pivac, J. Magn. Magn. Mater. 15, 934 (1980).
10. W.H. Kettler and M. Rosenberg, Phys. Rev. B 39, 12142 (1989).
11. J. Smit, Physica 16, 612 (1951).
12. A.K. Nigam and A.K. Majumdar, Physica B95, 385 (1978).
13. J. Yamasaki, H. Fukunaga, and K Narita, J. Appl. Phys. 52, 2202 (1981).
14. M. Naka, R. Kern, and U. Gonser, J. Appl. Phys. 52, 1448 (1981).
15. K. Fukamichi, R.J. Gambino, and T. R. McGuire, J. Appl. Phys. 53, 8254 (1982).
16. Y.D. Yao, Sigurds Araj, and S.T. Lin, J. Appl. Phys. 53, 2258 (1982).

17. G. Böhnke, N. Croitoriu, M. Rosenberg, and M. Sostarich, IEEE Trans. Magn., MAG-14, 955 (1978).
18. S.N. Kaul and M. Rosenberg, Phys. Rev. B 27, 5698 (1983).
19. I.A. Campbell, A. Fert, and O. Jaoul, J. Phys. C 3, S 95 (1970).
20. Hang Nam Ok and A.H. Morrish, Phys. Rev. B 22, 3471 (1980).
21. K. Fukamichi, M. Kikuchi, S. Arakawa, and T. Masumoto, Solid State Commun. 23, 955 (1977).
22. T. Kemény, I. Vincze, and B. Fogarassy, Phys. Rev. B 20, 476 1979.
23. T. Tarnoczi, I. Nagy, C. Hargitai and M. Hosso, IEEE Trans. Magn., MAG-14 , 1025 (1978).
24. A.S. Schaafsma, H. Snijders, and F. van der Woude, Phys. Rev. B 20, 4423 (1979).
25. C.L. Chien, Phys. Rev. B 18, 1003 (1978).
26. C.L. Chien, D. Musser, E.M. Gyorgy, R.C. Sherwood, H.S. Chen, F.E. Luborsky, and J.L. Walter, Phys. Rev. B 20, 283 (1979).
27. H. Franke and M. Rosenberg, J. Magn. Magn. Mater. 7, 168 (1978).
28. J.A. Cusidó, A. Isalgué, and J. Tejada, Phys. Status Solidi A87, 169 (1985).
29. T. Masumoto, H. Kimura, A. Inoue, and Y. Waseda, Mat. Sci. Eng. 23, 141 (1976).
30. Hang Nam Ok, Kyung Seon Baek, and Chul Sung Kim, Phys. Rev. B 24, 6600 (1981).
31. T. Nagarajan, U. Chidambaram Asari, S. Srinivasan, V.

- Sridharan, and A. Narayanswamy, *Mat. Sci. Eng.* 97, 355 (1988).
32. A.K. Majumdar, V. Oestreich and D. Weschenfelder, *Phys. Rev. B* 27, 5618 (1983).
 33. J.-P. Jan, in *Solid State Physics* edited by F. Seitz and Turnbull (Academic, New York, 1957), Vol. 5, p. 1.
 34. F. Keffer, in *Handbuch der Physik*, edited by S. Flügge and H.P.J. Wijn (Springer-Verlag, 1966) Vol. 18, p. 1.
 35. T. Kaneyoshi, *J. Phys. C* 5, 5304 (1972).
 36. U. Krey, *Z. Phys. B* 31, 247 (1978).
 37. B.E. Argyle, S.H. Charap, and E.W. Pugh, *Phys. Rev.* 132, 2051 (1963).
 38. F.J. Dyson, *Phys. Rev.* 102, 1217 (1956); 102, 1230 (1956).
 39. J.A. Copeland and H.A. Gersch, *Phys. Rev.* 143, 236 (1966).
 40. T. Izuyama and R. Kubo, *J. Appl. Phys.* 35, 1074 (1964).
 41. J. Mathon and E.P. Wohlfarth, *Proc. R. Soc. London, Ser. A* 302, 409 (1968).
 42. R.L. Mössbauer, *Z. Physik* 151, 124 (1958) ; *Z. Naturforsch* 14a, 211 (1959).
 43. G.M. Bancroft, *Mössbauer Spectroscopy* (McGraw Hill Book Co., England, 1973).
 44. G.K. Shenoy and F.E. Wagner, in *Mössbauer Isomer Shift* (North Holland Publishing Company, Amsterdam, 1978).
 45. *Mössbauer Spectroscopy and its applications*, Proceedings of a Pannel, Vienna, 24-28 May 1971 (International Atomic Energy Agency, Vienna, 1972).
 46. P.W. Nicholson, *Nuclear Electronics* (John Wiley and Sons, New

York, 1979).

47. G.F. Knoll, *Radiation Detection and Measurement* (John Wiley and Sons, New York 1979).
48. V.J. Law and R.V. Baiele, *Chem. Eng. Sci.* 18, 189 (1963).
49. P.J. Cote and L.V. Meisel, in *Glassy Metals I*, edited by H.-J. Güntherodt and H. Beck (Springer-Verlag, New York, 1981), vol. 46, p. 141.
50. A.K. Majumdar and G. Uffinger, *Solid State Commun.* 51, 967 (1984).
51. L. Berger, in *Magnetism and Magnetic Materials 1976* (Joint MMM-Intermag Conference, Pittsburgh), Partial Proceedings of the First Joint MMM-Intermag Conference, edited by J.J. Becker and G.H. Lander (AIP, New York, 1977), p. 355.
52. R.L. Jacobs, *Phys. Status Solidi* B107, K13 (1981).
53. M. Mitera, M. Naka, T. Masumoto, N. Kazama, and K. Watanabe, *Phys. Status Solidi* A49, K163 (1978).
54. R.C. O' Handley, M.C. Narashiman, and M.O. Sullivan, *J. Appl. Phys.* 50, 1633 (1979).
55. R. Hasegawa, R. C. O' Handley, and L. I. Mendelsohn, in *Magnetism and Magnetic Materials 1976* (Joint MMM- Intermag Conference, Pittsburgh), Partial Proceedings of the First Joint MMM-Intermag Conference, edited by J.J. Becker and G.H. Lander (AIP, New York, 1976), p. 298.
56. J.J. Becker, F.E. Luborsky, and J.L. Walter, *IEEE Trans. Magn.*, MAG-13, 988 (1977).
57. R. Hasegawa and Ranjan Ray, *Phys. Rev. B* 20, 211 (1979).
58. M. Grimsditch, A Malozemoff, and A. Brunsch, *Phys. Rev. Lett.*

- 43, 711 (1979).
59. Y. Ishikawa, K. Yamada, K. Tajima, and K. Fukamichi, J. Phys. Soc. Japan 50, 1958 (1981).
 60. K. Moorjani and J.M.D. Coey, *Magnetic Glasses* (Elsevier Science Publisher, B.V., 1984).
 61. F.E. Luborsky, J.J. Becker, J.L. Walter, and H.H. Lieberman, IEEE Trans. Magn. MAG-15, 1146 (1979).
 62. Sigurds Aarj, R. Canton, M.Z. El-Gamal, L. Gránásy, J. Balogh, A. Gziraki, and I. Vincze, Phys. Rev. B 25, 127 (1982).
 63. F.E. Luborsky, J.J. Becker, J.L. Walter, and D.L. Martin, IEEE Trans. Magn. MAG-16, 521 (1980).
 64. Powder diffraction file, Inorganic, vol. 6 and 34.
 65. T.E. Sharon and C.C. Tsuei, Phys. Rev. B 5, 1047 (1972).
 66. C.C. Tsuei and H. Lilienthal, Phys. Rev. B 13, 4899 (1976).
 67. C.L. Chien and R. Hasegawa, AIP Conf. Proc. 29, 214 (1976).
 68. L.R. Walker, G.K. Wertheim, and V. Jaccarino, Phys. Rev. Lett. 6, 98 (1961).
 69. M. Taniwaki and M. Maeda, Mat. Sci. Eng. 99, 47 (1988).
 70. U. Gonser, M. Ghafari, M. Ackermann, H.P. Klein, J. Bauer, and H.-G. Wagner, in *Proceedings of the 4th International Conference on Rapidly Quenched Metals*, edited by T. Masumoto and K. Suzuki, The Japan Institute of Metals, Sendai, 639 (1982).
 71. G.Le. Caer and J.M. Dubois, Phys. Status Solidi A64, 275 (1981).
 72. F.H. Sánchez, Y.D. Zhang, J.I. Budnick, and R. Hasegawa, J.

Appl. Phys. 66, 1671 (1989).

73. L. Takács, M.C. Cadeville, and I. Vincze, J. Phys. F 5, 800 (1975).
74. I. Nowik, I. Felner, Y. Wolfus, and Y. Yeshurun, J. Phys. F: Met. Phys. 18, 481 (1988).
75. L. Häggström, L. Grånäs, R. Wäppling, and S. Devanarayanan, Phys. Scr. 7, 125 (1973).

PHY-1991-D-SIN-MAG